



Tomas Bata University in Zlín
Faculty of Technology

Analýza makrostruktury polymerních materiálů

Analysis of macrostructure of polymeric materials

Doctoral Thesis

Author:

Ing. Tomáš Matoušek

Doctoral study programme:

P 2808 Chemistry and Materials Technology

Study course:

2808V009 Chemistry and Materials Technology

Tutor:

doc. RNDr. Petr Ponížil, Ph.D.

Zlín, 2015

CONTENT

CONTENT.....	2
ABSTRACT	5
KEYWORDS	5
ABSTRAKT	6
KLÍČOVÁ SLOVA.....	6
ACKNOWLEDGMENT	7
AIMS OF THE DOCTORAL STUDIES.....	8
INTRODUCTION.....	9
THEORETICAL BACKGROUND	10
1 Stereometry vs. stereology	10
1.1 First order stereology.....	11
1.2 Second order stereology	12
1.3 Stochastic geometry.....	12
1.4 Stereological probes.....	13
1.5 Proportional quantities in stereology.....	14
1.6 Basic stereological measurements	15
1.7 ASTM E112 standard	20
1.7.1 Comparison procedure	20
1.7.2 Planimetric procedure	21
1.7.3 Intercept procedure.....	21
1.8 Edge phenomenon in stereology.....	22
1.8.1 Gundersen's selection rule	22
1.8.2 Vertices rule	22
2 Tessellations	23
2.1 Point process.....	24
2.2 Types of tessellations.....	24
2.2.1 Voronoi tessellations	25
2.2.2 Poisson tessellation.....	25
2.2.3 Delaunay tessellation.....	26
2.2.4 Johnson-Mehl tessellation	26
2.2.5 Induced tessellation	26
3 Planar sections of porous media.....	27
3.1 Dispersity.....	27

3.2	Wicksell's corpuscle problem.....	28
3.3	Distribution functions.....	31
3.3.1	Normal and log-normal distribution	31
3.3.2	Bimodal distribution	33
4	Acquiring the digital image of internal structure.....	35
4.1	Digital cameras and scanners	36
4.2	Microscopic techniques.....	37
4.3	X-ray computed tomography	39
4.4	Other techniques.....	40
5	Image analysis.....	42
5.1	Digital image properties	43
5.2	Colour gamut, perception and interpretation of colours	44
5.3	Thresholding.....	47
5.4	Contrast modifications	47
5.5	Edge detection	48
5.6	Binary mathematical morphology	49
5.6.1	Erosion	49
5.6.2	Dilation	50
5.6.3	Opening and closing	51
5.6.4	Euclidean distance map	51
5.6.5	Skeletonization.....	53
5.7	Greyscale mathematical morphology.....	53
5.7.1	Watershed segmentation	54
EXPERIMENTAL		54
6	Materials.....	54
7	Methods.....	55
7.1	Computed X-ray microtomography	55
7.1.1	Instrumentation	55
7.1.2	Sample preparation	56
7.1.3	Scan parameters	57
7.1.4	Slices reconstruction	58
7.1.5	Optional reconstruction parameters	59
7.2	Structural analysis – CTAn software	60
7.2.1	Region and volume of interest.....	60
7.2.2	Thresholding	61

7.2.3	Structural analysis	62
7.3	Structural analysis – tessellation approach.....	63
7.3.1	Raw image pre-processing	63
7.3.2	Tessellation computation.....	65
7.4	Model of 3D structure.....	67
8	Results and discussion.....	69
8.1	CT vs. Voronoi tessellation	69
8.1.1	Sample HR4250	70
8.1.2	Sample CMHR6052	71
8.1.3	Sample PANTERA100	73
8.1.4	Sample 4070.....	74
8.1.5	Sample HR5050	76
8.1.6	Sample 3050.....	77
8.1.7	Sample 2545.....	79
8.1.8	Sample 2340.....	80
8.1.9	Sample 2015.....	82
8.1.10	Sample 3545.....	83
8.1.11	Acoustic properties of the foams.....	86
8.2	Other possibilities of Voronoi tessellation approach	88
8.2.1	Pore size estimation in pastry.....	89
8.2.2	Pore size estimation in resin/metal sintered composites.....	90
8.2.3	Grain size estimation in metal scratch patterns.....	92
	CONTRIBUTION TO SCIENCE.....	94
	USED SYMBOLS AND ACRONYMS	95
	LIST OF FIGURES.....	99
	LIST OF TABLES	103
	REFERENCES.....	104
	LIST OF PUBLICATIONS.....	114
	CURRICULUM VITAE	116
	APENDICES	117
	ORIGINAL PUBLICATIONS.....	122

ABSTRACT

This dissertation thesis “Analysis of macrostructure of polymeric materials” is divided into two main parts. The first of them gives a theoretical background, necessary for understanding the topic and content of the following chapters. The fundamental terms and definitions used in the experimental part are described from the point of acquisition the experimental data as well as their further processing and results interpretation.

The focus of the work in the experimental part is concentrated on studying the structure of soft polyurethane foams, namely quantification of their structural (three-dimensional) characteristics – pore size distribution and estimation of mean pore volume from the knowledge of sets of images representing planar cross sections (two-dimensional areas) through such a structure. Experimental data were captured employing the method of X-ray computed micro tomography and evaluated by means of two techniques. The former one was the image analysis method directly implemented in slice-reconstructing software, the latter one was based on Voronoi Tessellations.

KEYWORDS

Computed Tomography, Stereology, Voronoi Tessellation, Porous Structure, Polymeric Foams, Image Analysis, Pore Size Estimation.

ABSTRAKT

Tato disertační práce s názvem „Analýza makrostruktury polymerních materiálů“ je rozčleněna do dvou hlavních částí. V první z nich je podán teoretický základ důležitý pro pochopení tématu a obsahu dalších kapitol. Jsou vysvětleny zásadní pojmy a definice použité ve vlastní experimentální části, a to jak z pohledu pořízení experimentálních dat, jejich zpracování, tak výsledné interpretace.

V experimentální části se práce věnuje studiu struktury měkkých polyuretanových pěn, konkrétně kvantifikaci jejich strukturních (trojrozměrných) charakteristik – distribuci velikosti pórů a odhadu střední velikosti pórů ze znalosti pouze série obrazů řezů (dvourozměrných ploch) takovouto strukturou. Experimentální data byla pořízena metodou rentgenové výpočetní tomografie a vyhodnocena dvěma metodami. První z nich je obrazová analýza implementovaná v softwaru pro rekonstrukci řezů získaných tomografií, druhá metoda je založena na využití Voronoiových teselací.

KLÍČOVÁ SLOVA

Výpočetní tomografie, Stereologie, Voronoiovy Teselace, Porézní struktura, Polymerní pěny, Obrazová analýza, Odhad velikosti pórů.

ACKNOWLEDGMENT

At this place I would like to express my great thanks to my supervisor Doc. RNDr. Petr Ponížil, Ph.D., who made his best to tutor and advise me always when I was in need and therefore helped me a lot to solve all kinds of particular tasks related to my dissertation throughout the whole doctoral studies. I really appreciate his professionalism and kindness.

I would also like to mention and acknowledge to all people, which I met during the time of my doctoral studies, who pushed me forward even with a small idea or advice and to those, who encouraged me to not give it up when I switched to the part-time study mode in 2013. Every one of them has contributed to the origin of this thesis.

AIMS OF THE DOCTORAL STUDIES

The subject of this dissertation is the investigation and analysis of various soft polyurethane foams with open pores from the stereological point of view. The studied materials are chosen intentionally to cover a range of different densities and thus expected various pore sizes.

The experimental part deals with pore size estimation in the studied foams from planar sections through the samples and expressing the results in the form of estimated pore size distributions for each of them. The experimental data represented by images of reconstructed slices from X-ray computed tomography are processed employing two methods: The direct quantification of pore volumes by software supplied with the tomography and the novel way of estimation based on using Voronoi tessellations and image analysis techniques.

The main goal of this work lies in comparison of these two methods and critical evaluation of the applicability of the suggested novel method.

INTRODUCTION

All objects of macroscopic (naked-eye visible) dimensions, that surround us elsewhere, are from the more detailed view constituted from much smaller entities, e.g. cells in the case of living tissues or crystals, grains, pores or other particles, if we talk about inorganic materials. Their number, shape, size, orientation and mutual organization within the macroscopic object contribute to resulting properties of the material. This statement is confirmed by various studies in many disciplines ranging from biology, medicine, food technology as well as materials science [1]-[6]. Among the subjects of materials research we can find studying these small objects itself – the fillers dispersions and clustering in composite materials [7], [8], grainy structures; e.g. metals and alloys [9], [10], organizations of crystals in polymers [11] or pores in foam-structured materials in general [12] or specifically in polymers, metals or ceramics [13]-[15].

From the perspective of establishing the structure-properties relationship it is important to correctly classify the structure of the various species of the same material and measure relevant macroscopic properties (typically mechanical, physical or chemical) at comparable conditions to find the connection between these two subjects [5], [6]. Acquisition of data describing both the structure itself and related properties is not challenging, but the required extent of instrumentation and methodology might be a problem. Therefore, the main subject of theoretical part is concentrated mainly on estimation of structural characteristics of the observed material – soft polyurethane foams.

THEORETICAL BACKGROUND

1 Stereometry vs. stereology

Following the introductory part, it is necessary to classify the objects around us from more detailed view. While the *man-made objects* are predominantly formed in features considered as “regular shapes”, strictly based on planes, spheres, angles etc., the *naturally occurring objects* are commonly “irregular”. The former group of objects is in general called Euclidean shapes, after Greek mathematician Euclid (Εὐκλείδης, ca. 325-260 BC) who has described them in his work Elements and postulated the fundamentals of geometry [16]. The latter set of nature-based irregular shapes is simply called non-Euclidean shapes. As a consequence of this division, the methodology for studying these particular groups of shapes is also divided, as it is shown in Fig. 1:

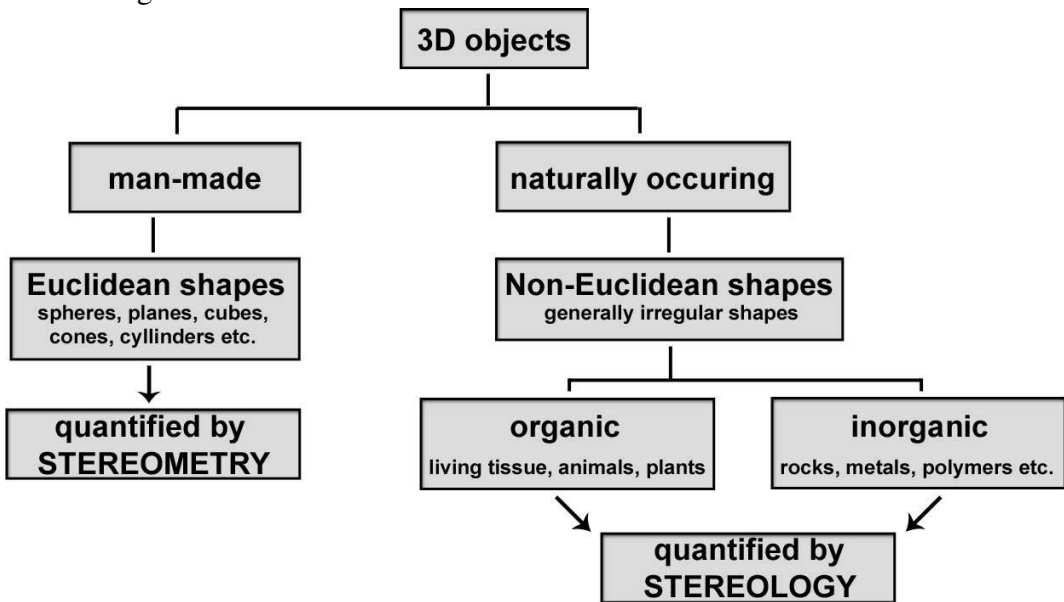


Fig. 1: Scope of stereometry and stereology. Scheme redrawn from [17].

The methods for quantification of classically shaped objects are included in the term *stereometry*¹ (formerly solid geometry) whereas *stereology*² has been derived from geometry and stereometry, and their principles apply on analysis of samples with various sizes and shapes [17], [18].

Several exact definitions of stereology, similar to each other, can be found in the literature; however, Underwood’s definition seems to be one of the most suitable:

^{1,2} Both words stereometry and stereology have their roots in Greek, where στερεός [stereos] means “solid”.

“Stereology deals with a body of methods for the exploration of three-dimensional space, when only two-dimensional sections through solid bodies or their projections on a surface are available” [19].

Simply said: stereology provides ways for determination of the quantities describing an internal structure of a material, such as mean size of the objects (particles, grains, pores) hidden inside the structure or even their orientation or size distribution. Basically, these procedures are based on transferring 2D projections appearing in the cuts through the solid material into the desired 3D values, mostly volumes, of the observed objects via applying stereological rules [20]. It can be also concluded from the Underwood’s definition of stereology, that in contrast with the direct and exact methods of stereometry, the result of properly carried stereological analysis is always only an estimated value of the given quantity. The explanation is simple – any stereological analysis is based on processing a *representative, randomly chosen sample* or set of samples and consequent statistical evaluation of the results [18], [21]-[24]. In other words employing the stereology enables us only *to estimate* the structural characteristics of the observed material. Sampling a material for stereological analysis must be done carefully and with special attention paid to the internal structure itself. Correctly taken sample includes both the observed structure of interest and also the remaining parts of the structure, all with the same probability as the observed structure. In the case of oriented structures one has to take into account also the orientation of studied objects [3], [25]-[27].

The history of stereology began in the second half of 18th century, when the French mathematician and naturalist Georges Louis Leclerc de Buffon (1707-1788) started to investigate the relations between geometry and probability. The “Buffon’s needle problem” [28], [29], is undoubtedly one of his most popular works. Buffon’s extensive work has contributed to formulation of the fundamentals of stereology. Although the basic stereological theory has been known since the 18th century, the stereology, as an independent scientific discipline, was established much later, in 1961 at the founding meeting of the International Society for Stereology organized by German professor of biology Hans Elias (1907-1985), who is considered to be the founder of modern stereology [20]. Nowadays, after more than two centuries from its origin, stereology is the integral part of many scientific fields, namely mineralogy, metallography, biology, food industry or general materials research.

1.1 First order stereology

There are four basic structural entities (also known as first order parameters) recognized in stereology. These virtual shapes, shown in the Fig. 2 are Volume – V , Surface – A , Length – L and Number – N . The appropriate quantification of these formations is essential for further structure evaluation. Their direct measurement is, however, mostly impossible due to opacity of the studied materials. In such cases it is only possible to see the internal structure of interest on either planar cut(s) through the object(s) or on the planar surface, if available. That unfortunately means a partial loss of the information about the internal structure itself. In practice only 2-dimensional (2D) profiles are observable instead of the original 3-dimensional (3D) objects; volumes appear as areas, surfaces seem to be curves, linear features

become points, and finally objects, when intersected by a plane become an unequal number of sectional profiles [24]. This is schematically shown in Fig. 2:

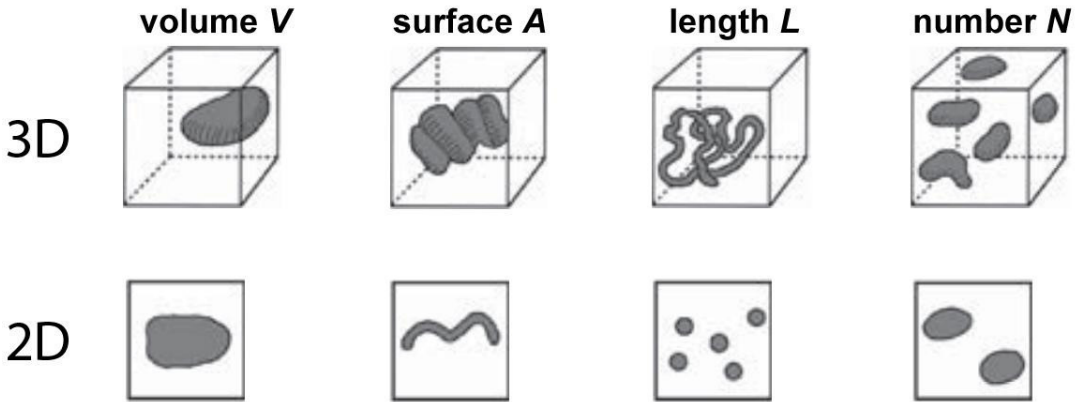


Fig. 2: Relations between basic stereological 3D entities and corresponding 2D projections. Redrawn from [23].

1.2 Second order stereology

Second order stereology is based upon first order stereology and serves as a tool for estimating the spatial organisation of objects. Foundation of these methods was initiated mainly by biologists which were searching for more complex quantification methods of biological objects with more complicated shapes than in the case of inorganic materials [17], [24]. The methods of second order stereology often include estimation of connectivity used e.g. for connectivity analysis of trabecular structure of bones [30], organisation of tissue cells [31], or have been suggested for tasks like estimation of average number of particles within a given distance to a typical particle [32], or, last but not least for the nearest neighbour analysis to estimate the distances between particles [23], [33].

1.3 Stochastic geometry

Stochastic geometry denotes a certain approach to examination of random spatial objects. Basically, stochastic (meaning “random” or “probabilistic”) geometry is a mathematical concept combining the probability theory with integral geometry. Thus, it is frequently utilized i.a. for the stereological analysis. The techniques employing the principles of stochastic geometry allow *unbiased sampling* and therefore lead to finding the results undistorted by presumptions on the studied materials. *Stereological bias* connotes a distortion of results from the reality caused by influence of a systematic error arisen in the course of sampling. In other words, the term unbiased sampling ensures uniform and random sampling. The typical feature of the methods based on unbiased sampling is decreasing scattering of results with increasing number of measurements [34], [36].

1.4 Stereological probes

Stereological probe is a type of geometric construction used for sampling the structural objects. The interactions between the probes and the objects of interest are called events. The number of events is linked with the estimated quantity [24]. Depending on the nature of the studied material (see Fig. 2), as well as the goal of the stereological analysis, one can choose from four basic probes, as illustrated in Fig. 3:

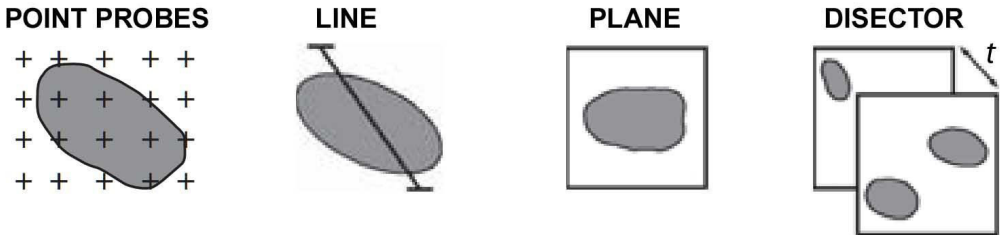


Fig. 3: Basic types of stereological probes. Redrawn from [23].

The relations between probes and 3D objects are schematically shown in Fig. 4:



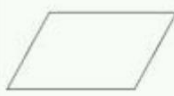






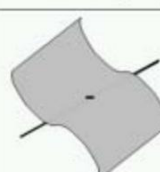
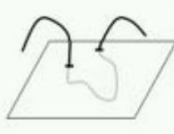

Probe	 Point (0D)	 Line (1D)	 Plane (2D)	 Volume (3D)
\cap Feature	 Volume (3D)	 Surface (2D)	 Length (1D)	 Number (0D)
= Countable events	 Countable events	 Countable events	 Countable events	 Countable events

Fig. 4: Events caused by interactions of probes with objects. Redrawn from [24].

Characteristics of stereological probes:

- **Point** – dimensionless probe (0D). Point is indicated solely by its position in the space; it has neither direction nor orientation.

- **Line** – one-dimensional probe (1D). Line has both certain position and orientation in space.
- **Plane** – two-dimensional probe (2D). Similarly to line, plane is described by its position and orientation in space.
- **Disector** – three-dimensional probe (3D). Disector is a virtual construction of two parallel, not identical, planes in space. The gap t between these planes determines the volume of the probe. In contrast with the previous probes, this type can be employed also for second order stereological analysis [3], [24].

Note the loss of the structural information about the original 3D structure after using a probe in Fig. 4; the dimensionality of the structural information is always lower than the dimensionality of the original object [24]. Thus, if ignored, this phenomenon may lead to undesirable affection or inaccuracy of the results. As an example, let’s have a planar cut through a real spherical object in Fig. 5. A transverse cut of the apple shows the apple body as an area, the surface seems to be a linear contour and the worms’ paths (in the image represented by three black speckles) are transferred to a dimensionless count of events.

feature	original dimension	probe	seen as
apple body	volume (3D)	plane (2D)	area (2D)
apple surface	area (2D)		contour/line (1D)
worm tunnels	Length (1D)		count (0D)

Fig. 5: A transverse cut through the apple showing the loss of the original structure information, when cut by plane. Picture of apple from source [35], modified.

1.5 Proportional quantities in stereology

Expressing the results of stereological analysis is possible in absolute values of first order parameters; however, it is more convenient and therefore preferred to use established proportional units. Among the most important and most frequently used quantities belong:

- Volume fraction V_V [mm^3/mm^3] – is one of the most principal units in stereology quantifying the volume of studied phase inside a reference volume.
- Surface area density S_V [mm^2/mm^3] – describes the surface-to-volume ratio. As a surface in a volume can be considered any 2D feature – typically boundary between the cells entirely fulfilling the volume except the outer surface of such object (e.g. fracture-resulting surface).
- Length density L_V [mm/mm^3] expressing the length of a linear object within a reference volume.

- Numerical density P_V [mm^{-3}] counts the number of intercepts relatively to reference volume.

Similarly, in lower dimensions there are analogical measures:

- Area fraction or equally intercept area-to-reference area A_A [mm^2/mm^2] in 2D
- Length fraction L_L [mm/mm] denoting intercept length-to-reference length in 1D
- Point fraction P_P [-] is given by the number of events when points (the intersections of lines in the grid) coincide with the phase divided by the total number of points [36].

If used (and measured) appropriately, last three quantities can serve as the direct estimators for V_V , as shown by the Eq. (1):

$$V_V = A_A = L_L = P_P \quad (1)$$

The formula (Eq. (1)) as well as the further Eqs. (2) - (10) assumes a homogeneous nature of the observed structure and representatively chosen sample. Unless these conditions are not fulfilled, random sampling approach has to be followed [18], [22], [36].

1.6 Basic stereological measurements

Counting point fraction (P_P) method is based on superimposing the studied image by a set of point probes, typically organized into various grids and summing up the events when the grid intersects the object. The grid is repeatedly randomly placed over the image and the ratio events vs. total number of points – P_P is calculated. Consequently, the point fraction P_P can be easily transformed into V_V according Eq. (1). The method itself is illustrated in Fig. 6. A planar section through the studied two-phased object is covered with periodic array of points. The places, where the events appear, that means where the points hit the particles are highlighted. P_P value in this particular case equals to 9 : 25 (events : total number of points), that corresponds to 0.36 or 36 %, when expressed in percents [19].

Counting points at a line probe is analogical to P_P determination. This type of probe can basically serve for two types of measurement. Firstly, it enables measuring the number of points intersecting the particles boundaries, known as the number of points per unit length P_L [mm^{-1}]; secondly one can measure a simple count of intersections with the objects, denoted as number per unit length N_L [mm^{-1}] by means of line probes. To give an example, let's have a planar cut through a two-phased (α - β) heterogeneous material, where the first phase (α) is created by general solid particles surrounded by second phase (β) – a general homogeneous matrix, as it is shown in Fig. 7. When overlaid by line probe(s), two basic cases may happen in such a system:

In the simpler case (Fig. 7a) the particles of α phase are perfectly separated in β phase, and therefore only one phase interface ($\alpha\beta$) can be distinguished.

In the second case illustrated in Fig. 7b, some of the α phase particles touch their neighbours and, beside the $(\alpha\beta)$ interface, form an additional phase interface ($\alpha\alpha$) in between them. Thus, there can be counted from Fig. 7a:

- Number of intersections of the line probe with the $\alpha\alpha$ interface $(P_L)_{\alpha\alpha} = 0$.
- Number of intersections of the line probe with the $\alpha\beta$ interface $(P_L)_{\alpha\beta} = 10$.
- Number of intersections of the line probe with the α phase $(N_L)_{\alpha} = 5$.

Similarly, the same values can be defined for Fig. 7b: line-interfaces intersections $(P_L)_{\alpha\alpha} = 2$, $(P_L)_{\alpha\beta} = 10$ and line-particle intersections $(N_L)_{\alpha} = 6$.

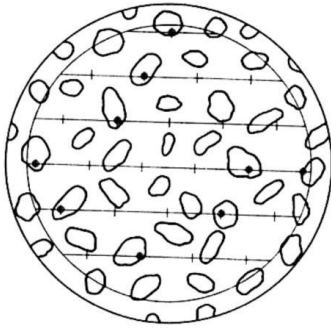


Fig. 6: Counting point fraction with point probes, redrawn from [19].

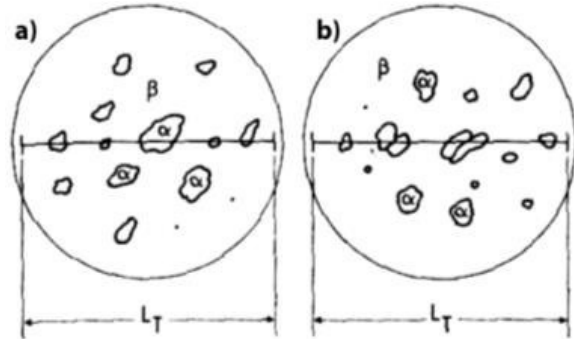


Fig. 7: Counting number of particle intersections by line probe L_T – a) two phases with the particles separated from each other, b) two phases with particles joined together, redrawn from [19].

For the case of separated particles, there is a logical equality between P_L and N_L , given by Eq. (2):

$$P_L = 2N_L \quad (2)$$

That means that number of line-boundary (of particles) intersections P_L is double compared to number of simple line-particles intersections N_L for the given probe. For mutually touching particles applies the following Eq. (3):

$$(N_L)_{\alpha\alpha} = \frac{2(P_L)_{\alpha\alpha} + (P_L)_{\alpha\beta}}{2} \quad (3)$$

Analysis of the number of points per unit length P_L is frequently employed for quantifying the surface area of objects within the observed volume, which is in fact the surface area density S_V . The relation between these quantities is given as Eq. (4):

$$S_V = 2P_L \quad (4)$$

It is also possible to determine the value of the length of a linear object or its perimeter per unit area L_A [mm/mm^2] instead of P_L , which is more convenient way in

case of digital images. Practically, S_V is assessed by means of conversion of the total length of boundaries in the studied region according Eq. (5) [3], [36]:

$$S_V = \frac{4}{\pi} L_A \quad (5)$$

However, always when the digital images are analysed, it must be paid a special attention to one substantial feature of them. As it is shown in Fig. 8, the objects in digital images consist of pixels (px) – squares of finite dimension. Thus, the resulting value of L_A is strongly dependent on the manner of interpreting the boundaries by the used SW.

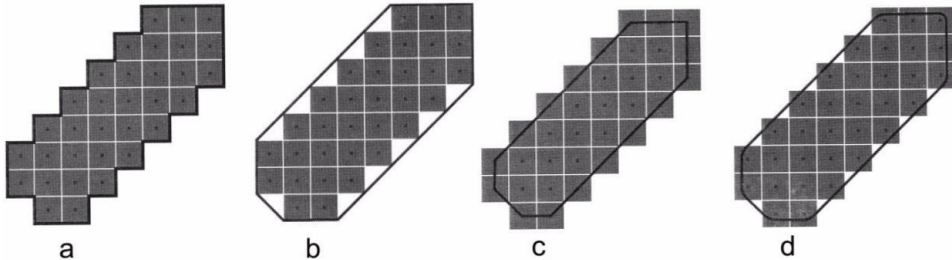


Fig. 8: a) the object boundary stretched around the pixels' boundaries, b) "smoothing" the perimeter of the object, c) the connector of the centres of the outer pixels, d) "smoothing" the perimeter with preserved real area of the object, redrawn from [3].

As it is evident, it is very important to choose a probe appropriately to the measured stereological characteristics. The above mentioned examples do not cover the structure orientation, which also play a significant role in selecting the most suitable probe. A number of various grids considering different types of structure orientation have been suggested. Some of them are shown in Fig. 9, Fig. 11 and Fig. 12:

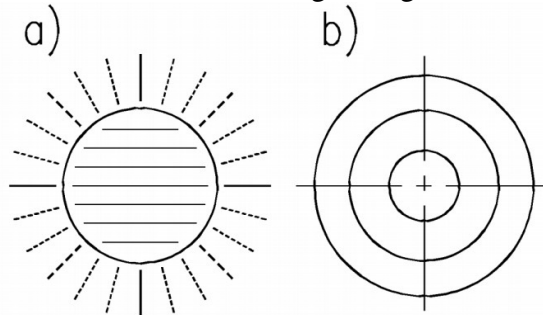


Fig. 9: Linear testing grids for P_L measurements on oriented structures, redrawn from [19].

Fig. 9a shows both parallel line grid for analysis of random non-oriented structure and propose radial line grid which can be used for measurements of directionality of the examined structure. Another type of grid is circular grid illustrated in Fig. 9b. This grid enables measuring either oriented or non-oriented structures. Among others,

a circular grid is applied in Heyn’s intercept grain size procedure for metallic grains standardized in ASTM E 112 [19], [37].

For measuring the structures, which are supposed not to be isotropic in 3D, it is necessary to use a probe which ensures isotropic, uniform and random sampling. Such a probe can be cycloid³, shown in Fig. 10. The parameters of this curve can be expressed in dimensions of circumscribed rectangle of height h ; then width equals to $(\pi/2)h$ and length of cycloid is $2h$. Thank to the construction of cycloid, when the fraction of its length pointing in a given direction decreases as the tangent rotates from the vertical direction in a manner that is proportional to the sinus of the angle from the vertical [36]. Such a curve can be used for construction of grids for unbiased P_L estimation in anisotropic 3D structure and further determination of value for S_V .

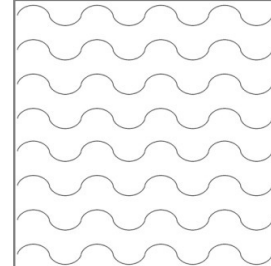
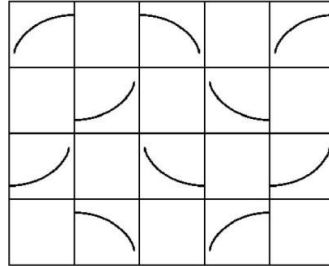
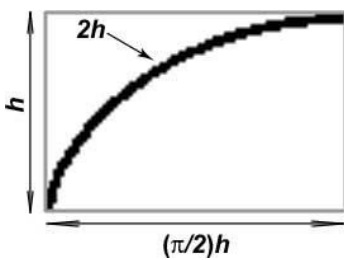


Fig. 10: Cycloid curve inscribed in the rectangle of height h , redrawn from [36]. Fig. 11: Cycloid-based grid, for vertical sections, redrawn from [39]. Fig. 12: Cycloid grid, redrawn from [38].

Fig. 11 and Fig. 12 show the ways of usage of cycloids as a probe. Fig. 11 illustrates a cycloid-based grid suggested by Cruz-Orive et al. for sampling on vertical sections [40], [41], whereas Fig. 12 shows cycloids rotated ninety degrees joined into “waves”. These, when applied to projected images, give isotropic sampling of the population of orientations of planes in 3D [36].

Next type of stereological measurement is counting points in an area of section. This measurement provides the quantity P_A [mm^{-2}] – area point count, which is the quantification of the count of points per unit area. This type of measurement is substantial mainly for measuring the length of linear objects (1D) in volumes (3D) i.e. linear density (so called line fraction), outlined in Fig. 13, or determining the count of vertices (points) of neighbouring objects in the plane of a section, as shown in Fig. 14, and consequently calculate feature count within the given N_A [mm^{-2}] area.

³ The cycloid is a curve generated by a point on the rim of a virtual wheel as rolling along a horizontal trajectory.

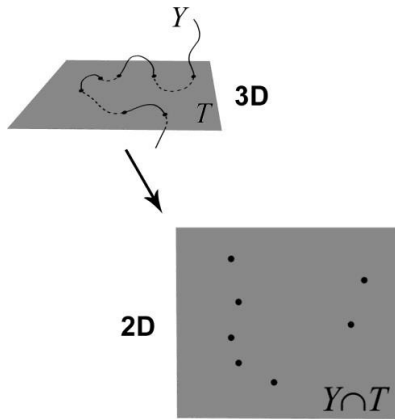


Fig. 13: Spatial linear object Y intersecting plane T is in 2D seen as a set of points, redrawn from [22].

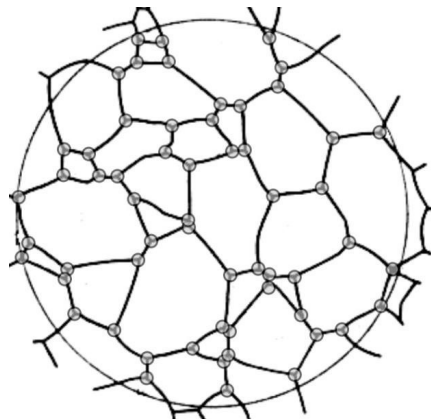


Fig. 14: Counting the number of vertices belonging to three neighbouring objects. The points are highlighted by grey circles, redrawn from [19].

For the case illustrated in Fig. 13, there has been suggested Eq. (6) putting into context the above mentioned area point count P_A with length density L_V . For the second instance, when the number of points in area unit is counted, Eq. (7) must be employed. This method is based on “triple points count” method following the principle that only points that belong to the common vertex of three objects are counted. The value of points intersecting the boundary of the area of interest are assessed to $\frac{1}{2}$ [21], [22], [36].

$$N_A = 2P_A \quad N_A = \frac{P_A}{2} + 1 \quad (6), (7)$$

In the structure shown in Fig. 14 is possible to determine the number of object intersections with the testing area even directly and this value can be transferred into the value of mean profile area \mathbf{EA} [mm^2]. The measurements as well as the following calculations vary with the nature of the studied structure, as two basic situations may happen:

The cells are touching each other and fill the space (area) entirely. That means that there is only one phase in the structure. In such a case \mathbf{EA} is counted as follows Eq. (8):

$$\mathbf{EA} = \frac{1}{N_A} \quad (8)$$

If the cells do not fill the area completely (there are 2 distinguishable material phases) the \mathbf{EA} is counted from the relation Eq. (9):

$$\mathbf{EA} = \frac{A_A}{N_A} \quad (9)$$

Where A_A is area fraction.

Besides that, direct counting the profiles is also possible to perform via the method of Jeffries [37], [42]. This method is based on summing up the objects N_w located fully inside a defined area and adding half of objects N_i intersecting the boundary. Thus, the total point of profiles N_r is given as Eq. (10):

$$N_r = N_w + \frac{1}{2}N_i \quad (10)$$

1.7 ASTM E112 standard

American Society for Testing and Materials (ASTM), is an international standards organization engaged in developing and publishing voluntary consensus technical standards for a wide range of materials, products, systems, and services.

The standard ASTM E112 – Standard test methods for determining average grain size [37] defines the methods for the estimation of average grain, crystal, or cell size in both metallic and non-metallic materials. These test methods cover procedures for estimating and rules for expressing the average grain size of all metals consisting entirely, or principally, of a single phase, however the described methods can be easily employed for any other material with the internal structure which is similar to metallic structure. The text of the standard highlights the fact that the test methods can serve only to the estimation of average grain and not as a precise method for measurements.

Basically, the standard defines three procedures for grain size estimation. For expressing the result of all methods the standard defines ASTM grain size number – G , defined as Eq. (11):

$$N_A = 2^{G-1} \quad (11)$$

Where N_A can be easily converted to mean feature cross sectional area \mathbf{EA} , following Eq. (8). Then, for transforming \mathbf{EA} to mean volume \mathbf{EV} applies the correlation according Eq. (12):

$$\mathbf{EV} = \sqrt{\frac{6}{\pi}} \cdot (\mathbf{EA})^{3/2} \quad (12)$$

1.7.1 Comparison procedure

The comparison procedure does not require counting the features, as it is based on comparison of the structure to a series of graded images, (illustrated in Fig. 15), either in the form of a wall chart, clear plastic overlays, or an eyepiece reticle. There appears to be a general bias in that comparison grain size ratings claim that the grain size is somewhat coarser (1/2 to 1 G number lower) than it actually is. Repeatability and reproducibility of comparison chart ratings are generally $\pm 1 G$ number. This method is recommended to use for determining the grain size of materials consisting of equiaxed grains. On the other hand, this technique is not applicable to measurement of individual grains [37].

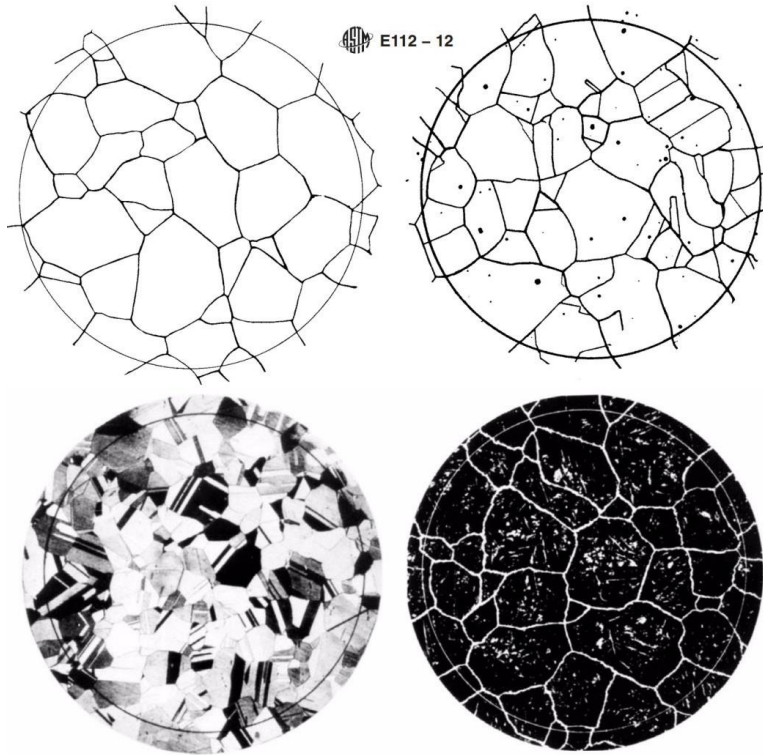


Fig. 15: Patterns of ASTM E112 for comparison procedure, redrawn from [37].

1.7.2 Planimetric procedure

This method involves an actual count of the number of grains within a known area (N_A). This value is consequently used to determine the ASTM grain size number, G . The standard declares the precision of $\pm 0.25 G$ (precision is a function of the number of grains counted). Results obtained by this method are free of bias and repeatability and reproducibility are less than ± 0.5 grain size [37].

1.7.3 Intercept procedure

Similarly to the planimetric procedure, this method involves an actual count of the number of grains intercepted by a test line or the number of grain boundary intersections with a test line, per unit length of test line, that are used for calculating the mean lineal intercept length L_L , which is transferrable to G . The precision of the method is a function of the number of intercepts or intersections counted. A precision of better than ± 0.25 grain size units can be attained with a reasonable amount of effort. The fact that an accurate count can be made without need of marking off the intercepts or intersections, the intercept method is faster than the planimetric method for the same level of precision [37].

1.8 Edge phenomenon in stereology

A set of dimensionless points is supposed to lie inside an observing area in such a way that none of them intersects the boundary of the area. However, having a set of objects (particles, pores, grains, etc.) with finite size inside the same observing area may cause some intersections of the objects with the boundary. These intersections are called edge phenomena [42]. Stereology introduces certain corrections and rules in order to govern the manners of handling with these situations. Basically, the corrections assess, whether the related objects are considered to lie inside the given area or not, and if counted, assign the weight of such object in the count. For the sake of brevity, only two most frequently used corrections are mentioned.

1.8.1 Gundersen's selection rule

The technique of Gundersen [43] introduces the observing rectangle-shaped frame, as shown in Fig. 16. This frame superimposed over the image of the observed structure suggests the limits for counting/rejecting the edge phenomena. The rule is quite simple: All objects which are located fully inside the rectangle as well as those protruding to light grey area are counted, while the remaining objects are ignored. The principle of the method is illustrated in Fig. 16. and Fig. 17:

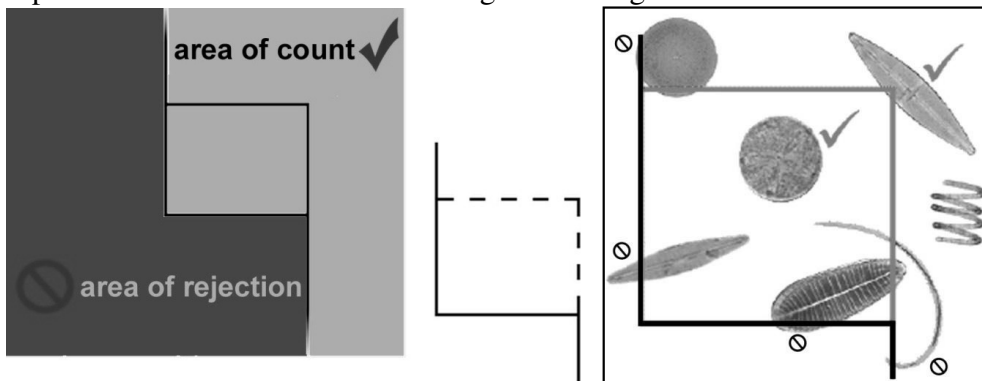


Fig. 16: Gundersen's rule of particle selection, redrawn from [44].

Fig. 17: Example of Gundersen's selection rule [44].

1.8.2 Vertices rule

It is also possible to determine the number of objects via vertices rule. The method is based on assessment of the coordinates values to the reference points of all objects, usually to the northernmost – $\max(y)$, easternmost – $\max(x)$, southernmost – $\min(y)$ and westernmost – $\min(x)$ points. The summation of these reference points divided by four relates to the estimation of the average count of objects within the observed area [45].

2 Tessellations

The word “tessellation“ is the name of a mathematical method for both partial and complete division of space into a finite number of cells, growing from the same number of points called tessellation nuclei or generators. The neighbouring cells have only one common boundary. The simplest algorithm for constructing the cells of tessellations is comparing the point-to-nuclei distances for each point within the area or space of interest. All points located closer to one nucleus than to other nuclei belong to the cell created from the former nucleus. The boundaries between cells are constructed by points having the same distance to more than one nucleus [46], [47].

Certainly, there are more types of different tessellations varying in ways of construction and cell shapes. The most common tessellations will be mentioned below. Also the distances used for cell construction may not be Euclidean in all cases; however, this happens only occasionally, for example to calculate traffic accessibility of streets in cities with perpendicular street network etc. [48].

Tessellations surround us and various examples of tessellations can be easily found elsewhere around us, some examples are shown in Fig. 18-Fig. 21 – typically at plates of bee honeycombs or at pavements constructed from tiles. Therefore, it is not surprising that stereology plays important role in certain scientific areas, mainly in astronomy, logistics, as it was already mentioned above, biology for studying the alimentation of living tissues, ecology for observing the animals’ settlements etc. In materials science tessellations serve as a model for polymer crystallization [46], or can be used for pore size estimation in polymeric foams [13], [49] and [50].

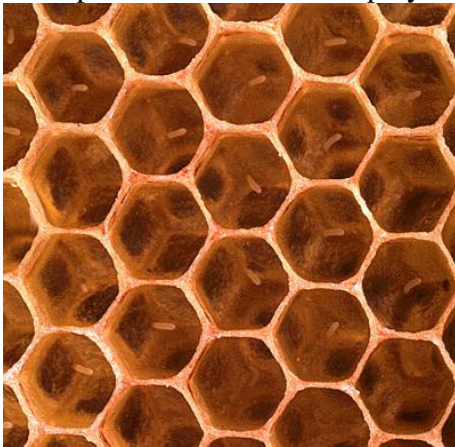


Fig. 18: Naturally-occurring tessellation – example I: a honeycomb [51].

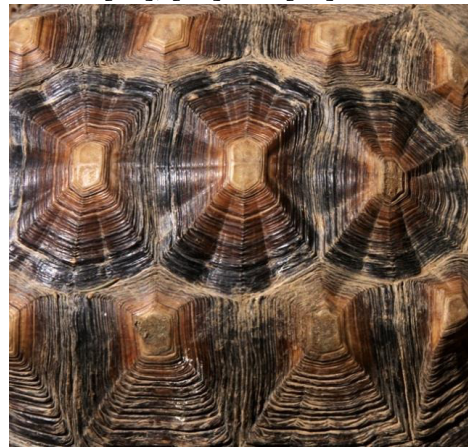


Fig. 19: Naturally-occurring tessellation – example II: a tortoiseshell [52].

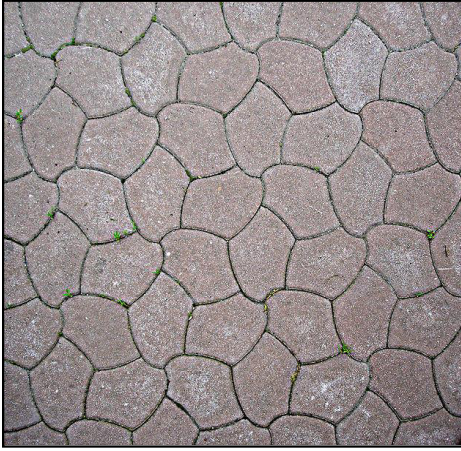


Fig. 20: Man-made tessellation – example I: pavement tiles [53].

Fig. 21: Man-made tessellation – example II: Gaudi's mosaic in Barcelona [54].

2.1 Point process

Point process is a term denoting the dislocation of tessellation nuclei in space. It is finite set of points Q ; $Q = \{x_1, \dots, x_n\}$ which is dislocated inside restricted region \mathbf{R} . Thus, such set creates a subset B in d -dimensional space \mathbf{R} , therefore: $B \subset \mathbf{R}^d$. The entire system Q may be considered as an intersection with another restricted set of points Φ within \mathbf{R}^d , then: $\Phi(B) = \Phi \cap B$.

If Φ is restricted in an arbitrary area and no two different points are coincident, then Φ is called point process in \mathbf{R}^d [47].

Various point processes can be identified; as each of them is characterized by its original way of points dislocation:

- Poisson point process (PPP) is distinguishable by uniformly distributed centres in the space, which are mutually independent. That means that each position of the considered space has the exactly same probability of an action occurrence in it.
- Non-homogenous point process is a result of non-uniformly distributed points. The non-uniformity is caused by attractive and/or repulsive interactions between the points. The former interactions lead to creation of cluster fields, the latter result in so called hard-core models [55].
- Periodically dislocated points create point grids [47].

2.2 Types of tessellations

The simplest classification of tessellations is assessing their regularity or irregularity. The main intention of regular tessellations is achievement of optimal fulfilment of space; therefore the main use is in some artificially created structures like mosaics or tiles [56], [57]. It is not so surprising that for the same reason bees make the honeycombs out of wax hexagonal-shaped cells. This construction provides them the biggest storage space with the smallest consumption of the material [58].

Cells of random tessellations are generated from tessellation nuclei and those are much more suitable for description of general structures. Random tessellations enable modelling pore structures in foams, crystal growth or grainy structure, e.g. in metals [46], [50], [59]-[63]; however, by means of employing different approaches, even very specific structural problems can be simulated. The most frequently used tessellations are listed below:

2.2.1 Voronoi tessellations

Group of tessellations named after Ukrainian mathematician Georgi Voronoi (Георгій Вороний, 1868-1908), who had been studying them intensively. The cells of Voronoi tessellation are generated from arbitrary set of points and for the majority of these points it is possible to find finite solution. Each cell includes only such points, closer to the respective nucleus than to other nuclei. The cell boundaries are formed from points with the closest distance to more than one tessellation nucleus. These tessellations is also possible to generate by the growth model – when all cells start growing concurrently from their nuclei with isotropic, constant velocity and the growth terminates when the neighbouring cells touch each other [59]. Very important feature of the cells is their convexity [47].

Voronoi tessellations can be generated by several different point processes:

- Poisson-Voronoi tessellation generated by PPP,
- Voronoi tessellation generated by Bookstein model (also known as Bookstein tessellation),
- Voronoi Tessellation generated by cluster field.
-

Comparison of these three types is shown in Fig. 22:

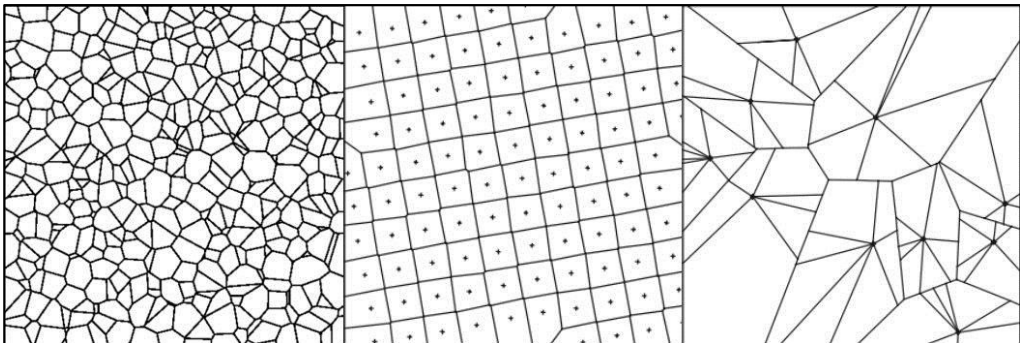


Fig. 22: Types of Voronoi tessellations: From left to right: Poisson-Voronoi tessellation, Bookstein tessellation, tessellation generated by cluster field, redrawn from [47].

2.2.2 Poisson tessellation

The main and essential difference from Voronoi tessellation is the way of cell generating. Cells of Poisson tessellations (Fig. 23) are built by direct construction of cell boundaries in two-dimensional plane or walls in 3D space. Boundaries of cells are determined by a system of random lines, whereas spatial cell walls are

defined by random planes. Such cells typically show high cell-size variability [47]. Owing to the way of cells creation, Poisson tessellation is also sometimes mentioned as Poisson-line tessellation [64].

2.2.3 Delaunay tessellation

Planar Delaunay tessellation (or triangulation) has its cells built from the optimal system of triangles. The vertices of these triangles are placed into the tessellation generators (Fig. 24). In 3D space Delaunay tessellation create tetrahedral cells [47], therefore this type of tessellation helps to resolve i.a. problems in solid mechanics. Recently, it has been suggested as a tool for polygonal finite element method [65].

2.2.4 Johnson-Mehl tessellation

This type of tessellation generates non-convex cells with curved boundaries. Similarly to Voronoi tessellation, also this tessellation can be constructed with the use of the growth model with one modification: The cells do not start to grow in the same moment. This tessellation typically serves as a model for austenitic steels with wide grain size distribution and presence of clusters or for certain cases of polymer crystallization, where the crystals grow in anisotropic manner [47], [60]-[62].

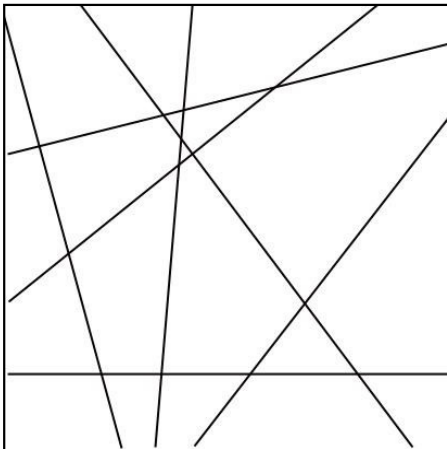


Fig. 23: Poisson tessellation, redrawn from [47].

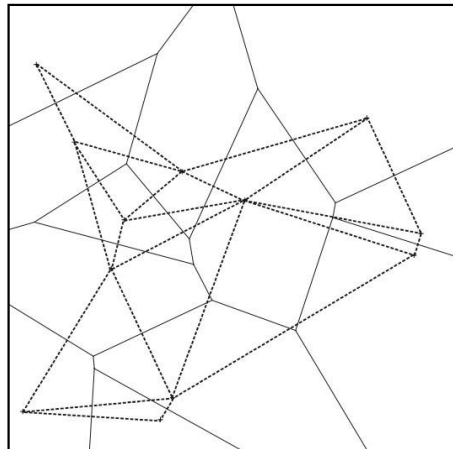


Fig. 24: Delaunay tessellation (dashed), induced by generators of Voronoi tessellation cells (solid lines), redrawn from [47].

2.2.5 Induced tessellation

This general group closes the short overview of tessellations. It contains planar tessellation induced by spatial tessellation as well as linear tessellation induced by spatial tessellation. It is obvious from their names that these tessellations are based on previously created spatial tessellation and both are created by intersecting the former tessellation by plane and line respectively. An illustration of linear tessellation induced by Poisson-Voronoi tessellation is shown below (Fig. 25):

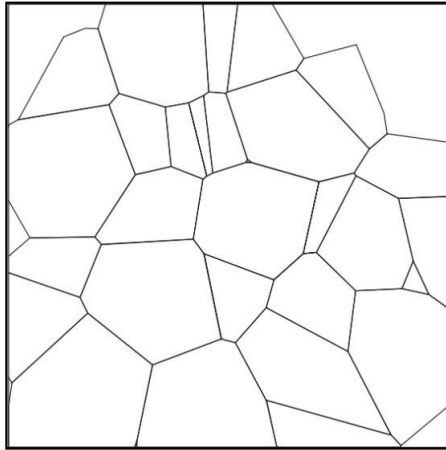


Fig. 25: Induced tessellation (planar cut through spatial Voronoi tessellation), redrawn from [47].

3 Planar sections of porous media

As it has been mentioned above (in paragraphs 1.1 and 1.4), an arbitrary planar cut through a solid material causes a partial loss of structural information about the original object(s) of interest. When the section plane intersects the body of (usually opaque) studied material, it reveals the boundaries of the internal structural entities which are situated above and below such plane. Porous materials, typically represented by polymeric, metal or ceramic foam-like structure, when cut, show pores' cross sections bounded by contours of pores' walls, frequently described as struts [66]. At this place it is important to note, that special attention must be always paid to several basic circumstances accompanying all planar sections prior performing the spatial structural characterization. It is also important to mention that these factors, which are described below, presume isotropic structures, without any directionality in all examples in order to keep simplicity.

3.1 Dispersity

In broader context, the term dispersity may refer to various features; however, in scope of materials, dispersity means one important characteristic of any particulate material ranging from pigments and dyes to polymeric fillers and molecular sizes in case of polymer chemistry [67], [68]. Last but not least dispersity can be defined also for grainy and porous structures [13], [69]. For the latest group of materials it can be defined as the rate of the heterogeneity of sizes of the individual pores [59], [66]. Dispersity of materials attracts the interest of scientist, since it relates to certain macroscopic properties such as specific surface, density or mechanical and acoustic characteristics [70]-[72].

In general, various degrees of dispersity can be seen in the materials. In the extreme situation, the system consists only out of elements of the same size as shown in Fig. 26, illustrating a set of spheres with constant diameter. Such system is monodisperse

and demonstrates the simplest type of dispersion. This type of dispersion is rare, though some polymer latex or nano- fillers for polymers prepared under strict conditions tend to monodispersity [73].

Principally, replacing part of the spheres in Fig. 26, by another monodisperse set of spheres, but with larger diameter results in bidisperse system (Fig. 27). Putting together spheres of arbitrary diameters (Fig. 28) can serve as an example of general polydisperse system and as an approximator of real porous structures (Fig. 29) [63].

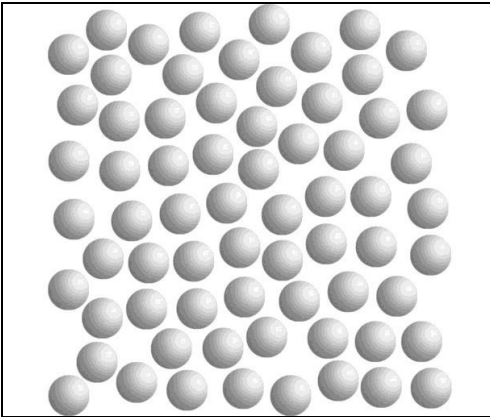


Fig. 26: A set of spheres with the constant diameter serving as a model of monodisperse particular system.

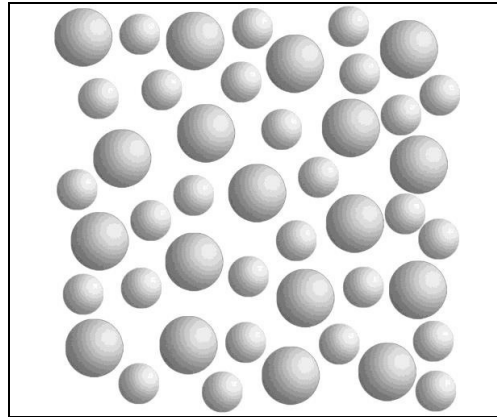


Fig. 27: Model of bidisperse system containing big and small spheres with the radii ratio between them 2:3.

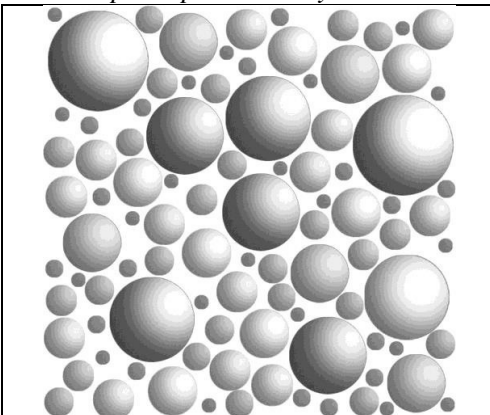


Fig. 28: Model of generally polydisperse system containing range of spheres with various sizes.

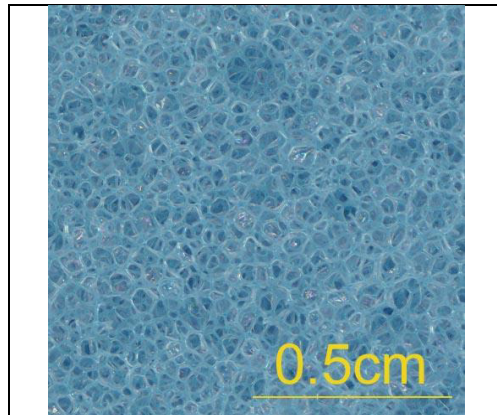


Fig. 29: Planar section through soft polyurethane foam as the example of real polydisperse structure.

3.2 Wicksell’s corpuscle problem

A classical stereological task dealing with planar sections through an opaque material which contains spherically-shaped particles was originally discovered by Swedish statistician Sven Dag Wicksell (1890-1939) in 1925 [74], [75]. As he described in his work, sectioning methods for measuring particle sizes making up the microstructure of materials do not provide accurate results, mainly because of two principal reasons.

Firstly, randomly dispersed set of non-overlapping spherical features (3D) whose radii can be described by continuous random function, when arbitrary embedded in a solid non-transparent material can be observed only on planar (2D) sections through the structure. Resulting circular cross sections do not correspond to the mean (equatorial) areas, because the random cutting plane rarely strikes the equator and therefore the viewed circular sections are mostly smaller than the equatorial cross section [76]-[78]. This problem is outlined in simplified way in Fig. 30, where the dashed line represents an arbitrary cutting plane and dark-grey area the corresponding circular cross sections. Moreover, it holds that a cross section size is inversely related to the distance of the cutting plane from a particle centre [74].

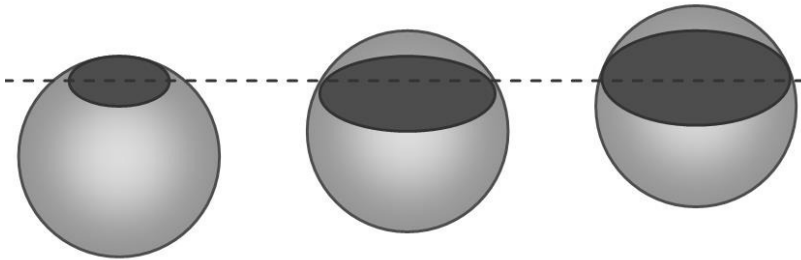


Fig. 30: Generalized sketch of Wicksell's corpuscle problem, redrawn from [50].

The second problem is that a planar section through the studied material with a polydisperse microstructure produces much greater number of bigger circular cross sections, than the smaller ones. The reason of it is simple: A random cutting plane hits a bigger sphere more likely than a small sphere. Thus, the size distribution of the intersected spheres is always size-weighted, preferring the larger spheres [78].

Additionally, the extreme model case is illustrated in Fig. 31. Random cutting planes c_1 , c_2 and c_3 intersect a polydisperse structure which includes also spheres A and B with the ratio between their radii $R_A : R_B = 2:1$. The cutting planes hit the structure and create planar sections through the material, when viewed in 2D. Each section generated by the respective plane provides a number of circular cross sections equalling to the number of sphere-plane hits. Note that only one plane (c_1) hits the sphere B, whereas the sphere A is intersected three times. Another fact, which is necessary to be emphasized, regarding to the plane c_1 , is the relative position of it to the spheres A and B. As it can be seen in Fig. 31, none of the chosen planes hits the sphere A at the equatorial line, highlighted by a thick black line. Therefore all of the cross sections S_1 , S_2 and S_3 through the sphere A (Fig. 32) are smaller than it would be the section at the equatorial line, though the cross section S_2 is near to it. That is in contrast with the sphere B, which is truncated exactly at the equator, thus providing circular cross section S_4 of mean sphere section area, when viewed in 2D.

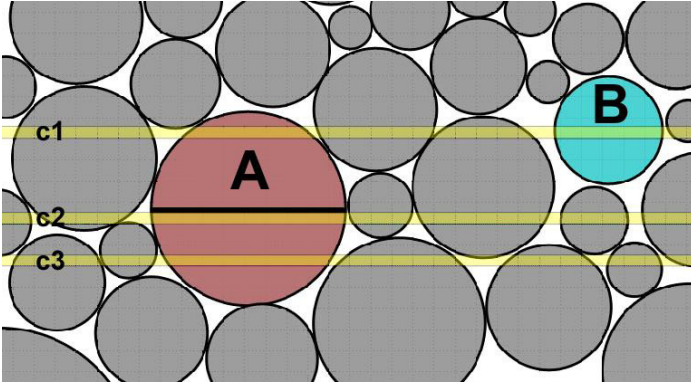


Fig. 31: Random cutting planes intersecting a general polydisperse structure.

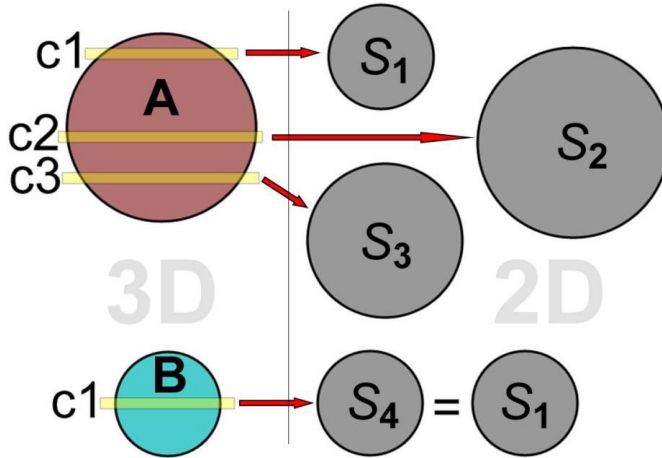


Fig. 32: Comparison of planar sections through the spheres A and B. Situation corresponds to Fig. 31.

Taking a closer look to the cutting planes and to the spheres A and B (Fig. 32) – shows, that the mean cross section through the sphere B – S_4 has the same area as S_1 – the northernmost cross section through the sphere A. However, the area of cross section S_1 is significantly smaller than a hypothetic equatorial cross section. Moreover, at a real planar cross section it is impossible distinguish whether this cross section is the equatorial or near-equatorial cross section of a small sphere or belongs to a near-polar cross section of a big sphere. The same applies for comparing two cross sections of the same area, as it has just been proved above.

Bearing in mind that the ratio between radii of spheres is $R_A : R_B = 2:1$ implies that the relation between the areas of mean cross sections of the spheres EA_A and EA_B can be derived by Eq. (13)-(15):

$$R_A = 2R_B, \quad V = \frac{4}{3}\pi R^3, \quad \Rightarrow \quad \mathbf{EV}_A = 8\mathbf{EV}_B \quad (13), (14), (15)$$

That means that if one considers a random planar cross section through a spherically shaped feature as its mean cross section, the following transformation to

its volume is always completely incorrect. To resolve this, on the basis of his observations, Wicksell proposed the following Eq. (16):

$$f_r(x) = \frac{x}{\mathbf{E}R} \int_x^\infty \frac{1}{\sqrt{y^2 - x^2}} dF_R(y) \quad (16)$$

Where f_r is the density of the cross section radii r and F_R is the cumulative distribution function of the sphere radii R in 3D Euclidean space. Further, $\mathbf{E}R$ is the mean of values R , and finally x, y are coordinates.

3.3 Distribution functions

Distribution is a term explaining scattering of the observed value around the mean value of a quantity x (μ), with standard deviation σ , defining the width of the distribution curve. The width of the distribution is also frequently called dispersity or the degree of dispersity. In other words, it means that distribution or distribution function assists as the graphical interpretation of dispersity [76].

Considering the relation to the material structure description, distribution has special significance, since the monodisperse systems appear very uniquely in practice. This applies both for man-made and natural structures. As an example we can point out to two simple instances: Comparisons between the sizes of apples that grew on the same tree reveal that some apples grew bigger than the others, or vice versa. Likewise, a handful of sand sieved through the system of superposed sieves with decreasing mesh always separate the larger grains from milder fractions. This regularity applies also to crystals in polymer materials and sizes for all types of cavities in porous systems as well [50], [77]. The most important distributions are discussed below.

3.3.1 Normal and log-normal distribution

The fundamental example of a distribution is normal (Gaussian) distribution. Probability density function (PDF) for the normal distribution is given by Eq. (17):

$$f(x) = \frac{1}{\sigma\sqrt{2\pi}} e^{-\frac{(x-\mu)^2}{2\sigma^2}} \quad (17)$$

Where μ is the mean value, and σ denotes the standard deviation.

The PDF of the normal distribution (Fig. 33) has typical bell-like shape with the extreme in the point corresponding to μ and it is symmetric around this value. The vast majority of the values of the quantity x (99, 6 %) is concentrated in the interval $\langle \mu \pm 3\sigma \rangle$ [79].

However, the occurrence of normal distribution in real structures can be hardly expected, but only tends to be normal [73]. Many of the real systems exhibit distribution resembling rather log-normal distribution, which is “skewed” towards to the left (Fig. 34). That relates to the situation when a material includes relatively small amount of big particles, (or pores, grains etc.) and considerably more of smaller particles. Similarly to the normal distribution, also log-normal distribution

is characterized by means o parameters μ and σ [21]. Analogically, the PDF is defined by Eq. (18) as follows:

$$f(x) = \frac{1}{x\sigma\sqrt{2\pi}} e^{-\frac{(\ln x - \mu)^2}{2\sigma^2}} \quad (18)$$

For better understanding, based on the above mentioned, it is possible to model a size distribution of spheres with a random distribution of radii R , using Gaussian distribution. With a certain non-zero probability this virtual distribution may correspond to the size distribution of spherical particles in a general simple structure as it is shown in Fig. 35. Assuming that such system is composed from sufficiently enough particles to make it sensible counting individual size fractions, it is possible to express the distribution by continuous function [21].

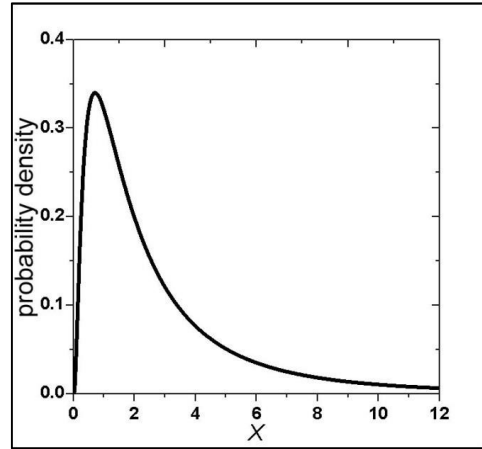
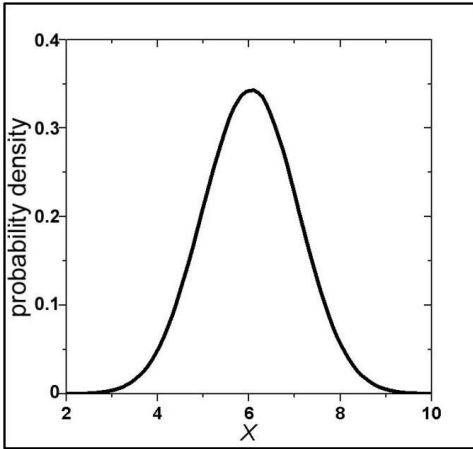


Fig. 33: Normal (Gaussian) distribution. Fig. 34: Log-normal distribution.

However, structure analysis of materials brings several difficulties. The principal problem is that the size distribution is tricky-discoverable directly. Mostly only planar (2D) sections through the studied structure are available and thus it is possible to determine directly only sizes of objects' cross sections and the respective distribution. That is, unfortunately, insufficient for the complete structural characterization, hence this “planar” distribution must be transferred into the “spatial” one. Besides that, it is important to remember that for the achievement of the correct results a representative random sample, where all parts of the structure are present with the same probability, must be taken [36].

In order to find out how will the size distributions of random cross sections with radii r through a set of spheres with Gaussian size distribution of radii R , look like, it is possible to model this situation.

The model case assumes a set of spheres with normally-distributed radii. All the spheres have their centres located at a straight line (in zero position). Providing that, a random cutting plane, which is parallel with that central line can occur at an arbitrary point within the interval $\langle 0, R_{\max} \rangle$, where R_{\max} is the radius of the biggest sphere with the same probability, the corresponding size distribution of cross sections is obtained. This model construction guarantees that

the “trimming probability” of a sphere is proportional to its size. In other words, the small spheres are intersected by the cutting plane with a small probability, while the larger spheres are intersected more likely. Comparison of these distributions offers Fig. 35:

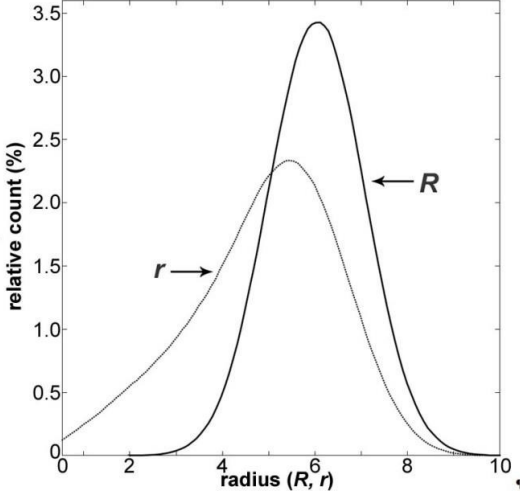


Fig. 35: Comparison of cross section radii (r) distribution with the corresponding sphere radii (R) normal distribution.

3.3.2 Bimodal distribution

The second example is a bimodal distribution. This type of distribution can be mostly understood as a summation of two mutually independent distributions [21].

Adding another normal distribution of sphere sizes with its own σ and μ to the initial model of spheres radii with Gaussian distribution (Fig. 35) creates a model of bimodal distribution, as shown in Fig. 36:

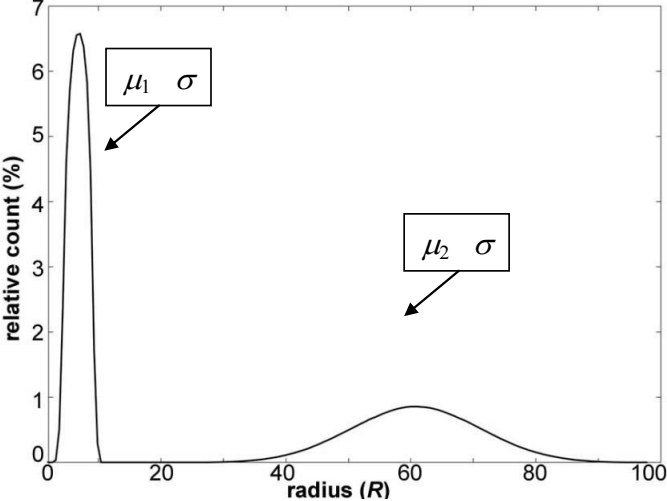


Fig. 36: Model of bimodal distribution.

In this particular model, the mean value of the second normal distribution μ is ten times greater than the mean value of the former distribution and as a consequence also the σ values vary tenfold, then:

$$\mu_2 = 10\mu_1 \quad , \quad \sigma_2 = 10\sigma_1 \quad (19), (20)$$

Regarding to the present bimodal model, it is necessary to mention that the ratio between the “smaller” and the “greater” spheres is 3:2 in favour of the smaller spheres. That results in the same ratio between the respective areas under curves.

Performing the cutting-by-random-plane approach, similarly as in the previous case leads to the following distribution (Fig. 37):

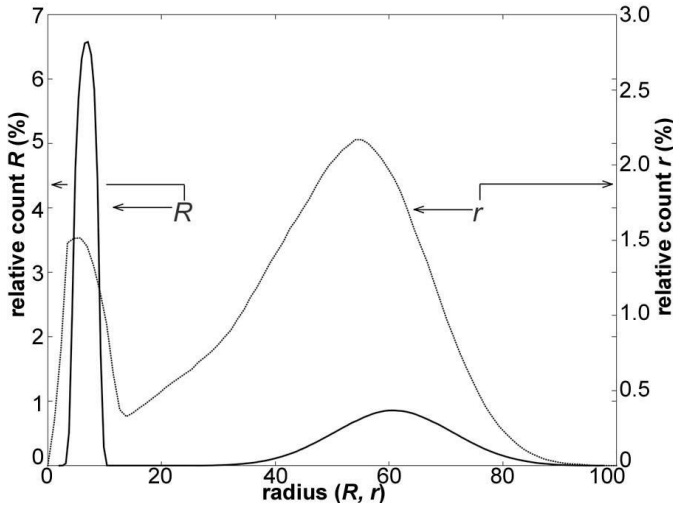


Fig. 37: Comparison of cross section radii (r) distribution with the corresponding sphere radii (R) bimodal distribution.

Finally, comparing the distributions of area of cross sections shown in Fig. 38 and Fig. 39 reveals non-symmetric curves, skewed to the left in both cases. Moreover, Fig. 39 exhibits two maxima. The left peak is significantly higher, but narrow. That means that the area under this peak relating to the number of cross sections is small. Conversely, the right peak, which is much broader and smaller, corresponds to the proportionally smaller amount of bigger cross sections, as compared with the smaller ones.

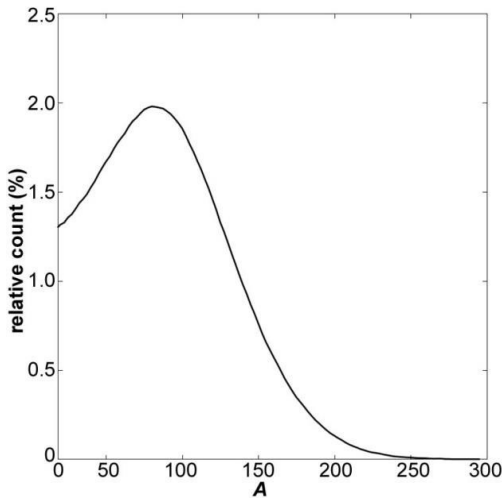


Fig. 38: Area of cross sections – distribution corresponding to the size distribution in Fig. 35.

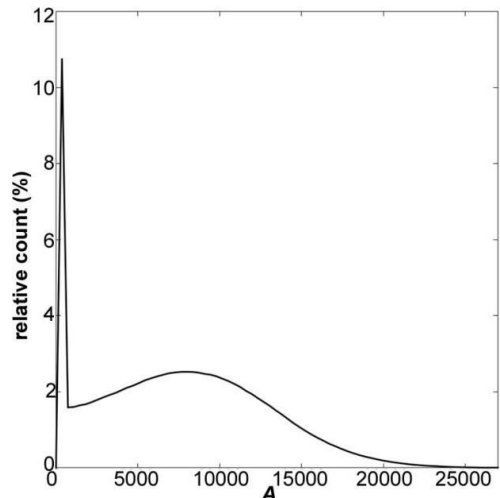


Fig. 39: Area of cross sections – distribution corresponding to the size distribution in Fig. 36.

4 Acquiring the digital image of internal structure

The original sample for the stereological analysis is an image or a set of images capturing the part of the structure which is being investigated. That can be a general cut through a material (Fig. 5), planar cross section through a porous medium (Fig. 29) shown above or a grainy structure, e.g. Fig. 40:

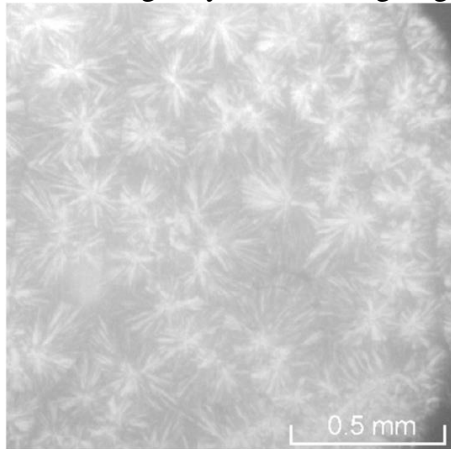


Fig. 40: A micrograph of the spherulitic structure of polypropylene, [46].

These three examples were chosen intentionally, in order to point out to the fact, that the way of image acquisition is dependent on the nature of the studied samples. The parameters determining the selection of the appropriate method are required magnification, and the fact whether it is a planar cut through the material or its surface.

4.1 Digital cameras and scanners

Digital cameras are the successors of classic cine-film cameras. The main principles of the device functionality remained unchanged; however, the most substantial difference is in the manner of image capturing. The originally used cine-film has been substituted by an image sensor (chip) which provides transformation of photons into electrons and thus creates electric charge. In other words, the chip ensures the transformation of the captured scene into its digital form, which is further saved and stored in the form of bytes in a memory card [80]. This principle facilitates the further handling with the image data, mainly the possibility of direct transfer into PC. At present, two types of chips are commercially available. The preferable CCD (charge coupled device) sensor is a part of vast majority of cameras and also is being used for the scientific and other hi-tech applications, where hi-definition images are strongly required. The second type – CMOS (complementary metal oxide on silicon) chip is cheaper, but due to incomparable higher noise generation is not sufficient for capturing the data for image analysis. However, it is still frequently used for certain applications, typically for cameras in mobile phones [3], [80].

Scanner is a device for direct image digitalization. The principle of scanner is based on direct imaging the pattern (original) and following digitalization of the captured image. The original is illuminated from below by a built-in lamp and by means of an optical system including several mirrors the reflected light signal is transported towards to a CCD chip. A simple scheme of a scanner is shown in Fig. 41:

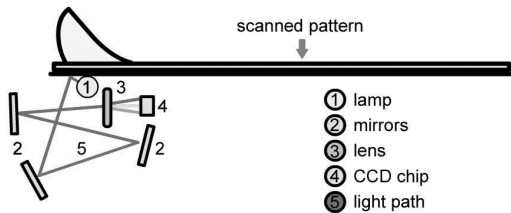


Fig. 41: The principle of scanning, redrawn from [80].

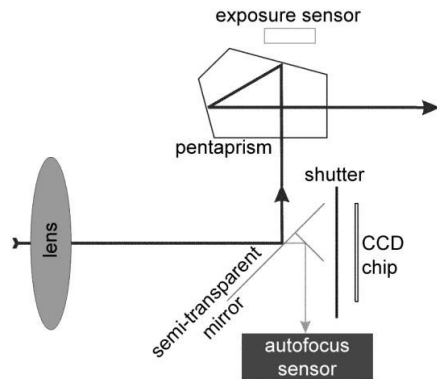


Fig. 42: Scheme of DSLR digital camera, redrawn from [81].

Fig. 42 is illustrating the optical path in DSLR (Digital Single Lens Reflect) camera. After passing the objective lens, the light hits foldable semi-transparent mirror at an angle of 45°. The biggest amount of light passes the viewfinder, while the rest continues towards to the sharpening sensor. During exposure, the mirror folds down and shutter opens which results in exposure of the chip. The shutter is opened as long as the exposure time is preset, enabling the incident light to illuminate the chip, which is located in front of the sensor.

Scanners and digital cameras do not have in common only the similar technology. Another common feature is a relatively low price compared to more sophisticated

devices discussed below. On the other hand, the disadvantage of scanners and cameras is in their relatively low magnification and resolution (up to ca. 1200 dpi – 1200 pixels per inch), which slightly surpasses the resolution of the human eye⁴ [82], [83].

4.2 Microscopic techniques

Microscopy is a technique of observing small objects or tiny details at magnifications that often greatly exceed the resolution abilities of human eye. The principle of the vast majority of microscopies is a specific interaction of radiation emitted by a radiation source with the studied sample [84].

The oldest and for stereological purposes most widely used microscope is an optical microscope (OM). This method, also frequently called light microscopy or optical light microscopy, employs as a radiation visible light emitted by means of a light source, typically by a tungsten wire in a bulb. The basic arrangement of OM can be modified in several ways, so that a range of materials can be studied. Basically, the samples can be observed either in reflected, or in transmitted light, when beam of light passes through the sample. The former case is being used for solid, non-transparent samples, e.g. [85], whereas the latter method has been a principal method of biological discovery for almost three centuries, serving as a tool for studying transparent samples [86]. If the optical path of OM includes a light polarizer, the microscope is able to display e.g. spherulitic structure of semicrystalline polymers, as already shown in Fig. 40. Using various filters and adjustments extends the usability of this method for a wide spectrum of samples and materials [87]-[89].

The limitation of OM is the wavelength of visible light ($\lambda \approx 400\text{-}750\text{ nm}$). By using the optical microscope it is possible to achieve the maximum magnification $z_{o_max} = 1500x$ and display tiny dots with size about $0.2\ \mu\text{m}$ [90], [91]. Transfer of images into the computer is ensured by a direct interconnection between the microscope and the PC. A simplified scheme of the optical microscope is shown in Fig. 43:

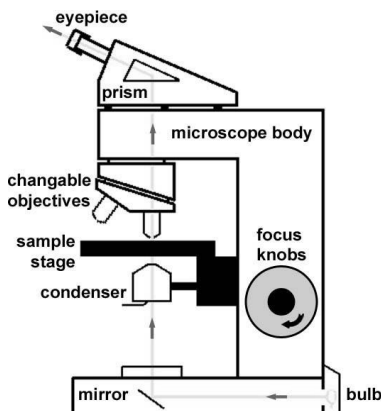


Fig. 43: Scheme of an optical microscope, redrawn from [92].

⁴ The resolution of human eye is about 700 dpi (in ideal light conditions) [82].

Going beyond the resolution of classical OM is enabled by usage of electron microscopies – scanning electron microscopy (SEM) outlined in Fig. 44 and transmission electron microscopy (TEM) illustrated in Fig. 45.

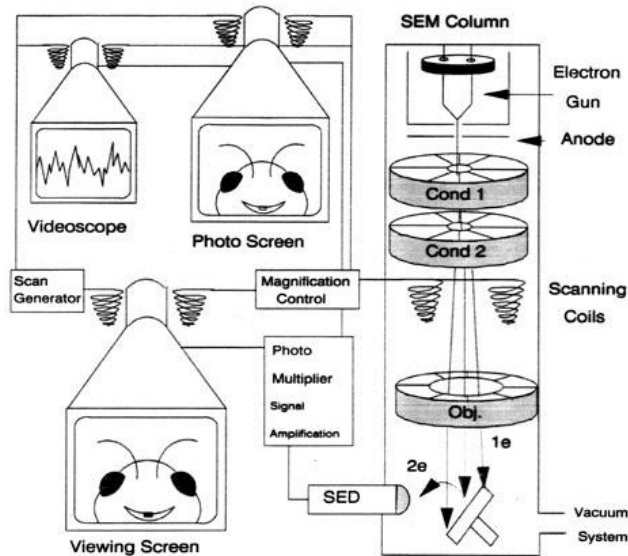


Fig. 44: Schematic illustration of scanning electron microscope [93].

The most substantial difference against OM is different type of used radiation. These techniques exploit an accelerated beam of electrons, emitted by an incandescent tungsten wire. The optical elements are substituted by the electromagnetic parts; radiation is focused towards to the sample using the condenser lens, which are in fact electromagnetic coils. Both methods differ from each other by the detection method of electrons. SEM detects either the electrons reflected from the sample (backscattered electrons) or the electrons ejected from the sample’s surface (secondary electrons), moreover the detection of transmitted electrons signal is also possible. TEM according to its name detects the electrons passed through the sample, primarily. Additionally, the difference is also in the manner how the electron beam incident to the sample. While in the case of SEM the electron beam is movable and successively scan the surface of the sample line by line, TEM employs the stationary electron beam. Finally, while SEM is able to display 3D images of the samples, TEM produces 2D images of thin samples [84], [91], [92].

The accelerated electron beam radiation has much smaller wavelength than the visible light and thus provides much higher resolution. According to the nature of both SEM and TEM it is stated in the literature that the maximum magnification for SEM is $z_{SEM} = 300,000x$ and maximum magnification of TEM – $z_{TEM} = 1,000,000x$ [91].

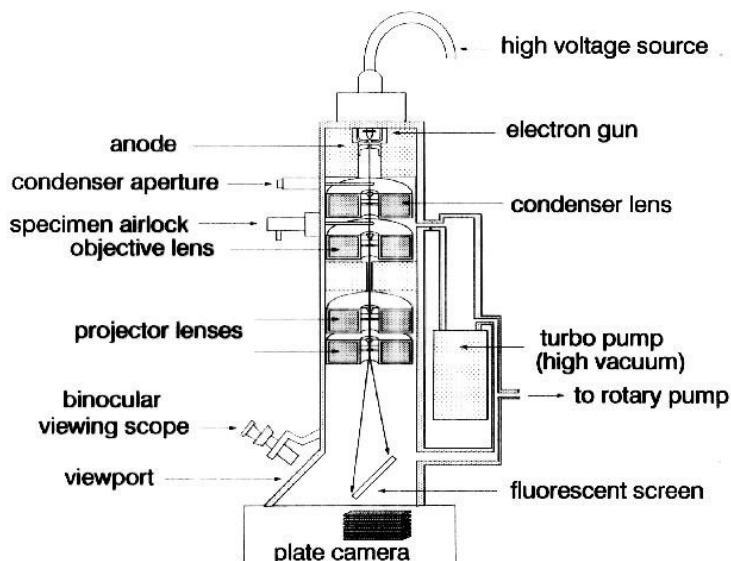


Fig. 45: A cut through transmission electron microscope [94].

As already pointed out, microscopes overcome scanners and digital cameras thanks to their magnifying power; however, the disadvantage of these techniques is the complexity of such devices, requiring the expertise of staff, especially for electron microscopes. Another complication is the need for preparing the samples to acceptable dimensions, while preserving representativeness of the structures plus additional sample modifications necessary to be done prior the microscopic observation. Utilization of electron beam also requires high vacuum inside the samples chamber. Last but not least, the problem may be the price of the device, which is many times higher than in the case of OM.

4.3 X-ray computed tomography

X-ray computed microtomography (CT) is a modern nondestructive digital imaging method. The word „tomography“ is derived from greek words τομος [tomos] – a cut and γραφο [grafo] – to write. Originally, CT was employed almost exclusively in medical diagnostics; however currently plays an important role also in materials research [66], [95]-[99].

The principle of the method can be described as recording the attenuation of X-rays which have passed through a sample. The studied sample is mounted to a rotatable sample stage, located in between an X-ray source and a CCD chip (Fig. 46) which enables scanning it from various angles. As the sample rotates around its vertical axis with a preset constant step between each two positions, the X-rays pass through the sample. The portion of the radiation which is neither absorbed, nor scattered by the sample expose the CCD chip at each position. As a result, a set of scanned grey projections is created and saved into the hard drive of the PC and further processed after the measurement [95]. In the following step a slice-reconstructing SW computes the images of transversal slices through the region of interest which may also contain the whole volume of the sample. The individual slices are in fact

equivalents of planar cross sections through the structure, thus they can be understood and processed as samples for stereological analysis. Thanks to it, it is possible to estimate the studied material characteristics [100].

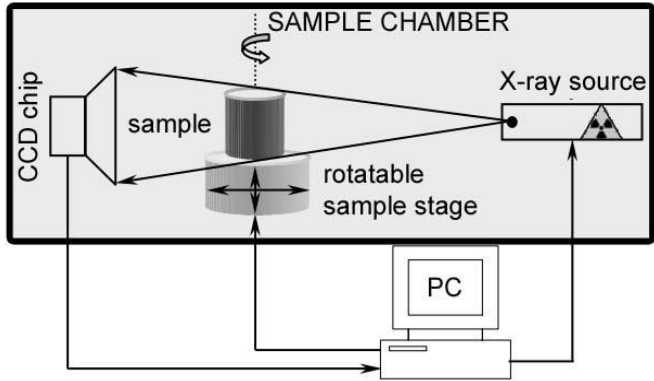


Fig. 46: Scheme of an X-ray mirco-CT, redrawn from [95].

The alternative to the stereological approach is employing a specialized SW, either provided by the supplier [100] or an external one [101], in order to quantify the structure computationally. This way of image post-processing is based on different X-ray attenuation coefficients of the particular features forming the micro-structural architecture of the studied material. That leads into corresponding contrast values in the image – as a good example may serve a foam-like structure, where the hollow parts (air) almost not absorb the radiation in comparison with the struts (solid). These variations in contrast within the sample image are evaluated by the SW and phase type is assessed [102].

The main and the most important advantage of this technique against the previously described methods is allowing the observer to insight into the internal structure of the material without the need of a special pre-treatment of the sample or damaging it. A special shaping is neither required, since the method is not limited by the sample’s shape⁵. The only limitations lie in the sample chamber (a few ccm) and in the scattering angle of the radiation itself. A spatial resolution of CT, which is one of the key parameters of the device, is determined by the resolution of the detection system. It is defined as a minimal spot size, which can be focused and thus depends on the X-ray-to-sample and sample-to-detector distances. The commonly used devices work with spatial resolution ranging from the order of a few tenth to micrometer units [95]. Similarly to the electron microscopes, a substantial disadvantage of this methodology is the financial demand on instrumentation.

4.4 Other techniques

In order to keep the completeness of the overview it is also necessary to mention the techniques, which are also capable to capture the desired structure beside the foregoing image acquisition methods. Some of these methods can be advantageously used in combination with e.g. scanning or microscopy.

⁵ though the cylindrical geometry is recommended

A stamping method [13] can be employed for studying the structure of porous materials with a flat surface, preferably at a planar cut. With the intention of highlighting the boundaries of the structural features the planar cut is covered with a contrasting colour in fine layer. Consequently, two operations are possible: if the sample's surface is not wettable, the highlighted parts can be stamped into a sheet of paper and the contours are scanned. Another possibility, leading to the same result is a direct scanning the highlighted sample and further suitable image processing of the scan, as outlined in Fig. 47. The method is very simple; however, it is not adequate for pores smaller than 0.5-1.0 mm (in diameter of the cross section).

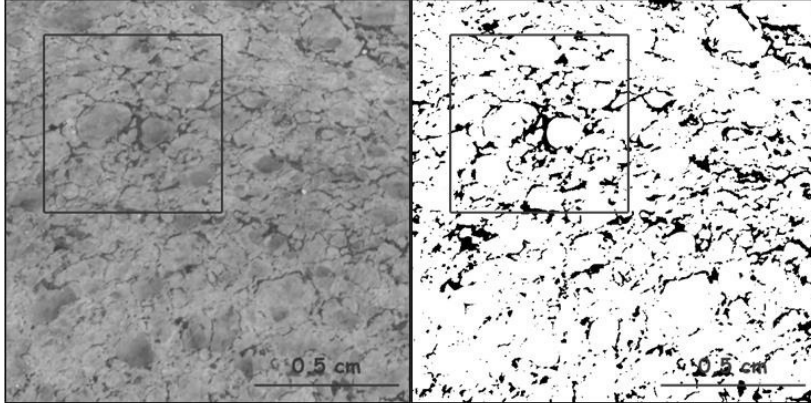


Fig. 47: Stamping method. Left: Scanned image of foam structure covered with contrasting ink for enhancing the pore cross sections boundaries. Right: Binarized scan [63].

Similarly, a disector measurement can be used for estimation of number of convex, arbitrarily shaped objects, provided that each of these objects has exactly one minimum or maximum of [3]. In essence, it is a measurement of thin sections, where both the top and the bottom of the cut are observed and checked whether the objects (particles, grains, pores) which appear on the upper side of the cut, pass through the disector, as shown in Fig. 48.

The number of convex objects per unit volume N_V [mm^{-3}] can be determined as the ratio between the number of maxima and minima (E) in the disector and double sample volume, which is given classically by the product of slice thickness times area of the sample, as shown in Eq. (21):

$$N_V = \frac{E}{2V} \quad (21)$$

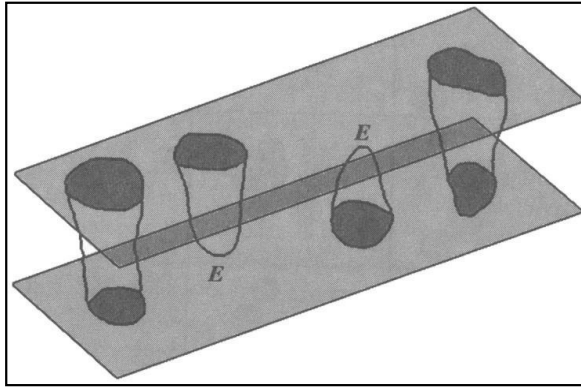


Fig. 48: N_V estimation by means of disector measurement [3].

Less used, but not less important method, which can be assessed to the group microscopic techniques is 3D (confocal) microscopy (CLSM - confocal laser scanning microscopy). It is built on similar principles as optical microscopy with the differences that the used light source is laser and the optical path of the microscope includes also a confocal aperture and a slit. The aperture is positioned precisely in the point that is optically associated with the plane of focus. Its function is preventing the return of light reflecting from the space outside the plane of focus. The result is displaying of one point within the given plane of focus. By scanning points from more levels above each other (i.e. in the optical axis of the system) it is possible to gain so called optical sections through the sample. These are consequently processed by SW into a coherent 3D image. To view the whole plane of the sample, it is necessary to scan it point by point at each point of the plane by moving the aperture over the plane at the defined raster. The output from CLSM is a reconstructed 3D model of the sample. Owing to its excellent resolution and image contrast, obtained without any special pre-treatment CLSM makes a bridge between OM and SEM [103], [104]. This method can serve as a suitable complementary technique to the stereology of 2D sections through structures containing geometrically complex objects, or as an alternative to a CT [99], [105], [106].

5 Image analysis

Image analysis is the key and integral part of stereology. By means of image analysis it is possible to obtain the data necessary for the mathematical (stereological) description of the structure. Simply said, the intention of image analysis is the correct interpretation of the image, both quantitatively and qualitatively plus obtaining the information about the shape, size and number of studied objects, or the design or arrangement and micro-structural architecture of these objects [107].

However, acquiring an image that captures a 2D projection of the studied structures is not sufficient very often. In many cases it is necessary to modify the input image prior to image analysis itself, in such a way to allow “extraction” of the required information from the image. In other words, there is a need for separation of the foreground, carrying information about the structure, and background

which is usually completely out of sense for image analysis. This separation process is called segmentation of the digital image. It is usually carried out as the very first step of the image analysis. The significance of segmentation within the image analysis is great – the accuracy of segmentation predetermines the precision of further steps of image processing. Moreover, it is important to choose a suitable segmentation technique with consideration to the particular image or the set of images [108], [109].

5.1 Digital image properties

At this place it is necessary to stress the fact, that a digital image is a record of a real object or scene stored in computer in the form of certain numerical values. Firstly, it is possible to assign the coordinates x and y to each pixel, secondly, the numerical value itself of this pixel expresses a certain image parameter [110]. Amongst the most important parameters of digital image describing their basic characteristics belong spatial resolution, dynamic range, image contrast and bit depth. In general, from an observer's perspective three types of the digital images can be perceived. These are either as black and white or greyscale or colour images. The type of each individual image seen on the computer monitor relates more or less to the already mentioned image properties.

Spatial resolution of an image (or simply image resolution) is a value determining a minimal size of an object which is possible to be distinguished in the image. It is usually quantified by means of dpi units – number of dots per inch⁶. Theoretically, the smallest distinguishable object must be constituted from 2 px, at least [3]. Logically, the higher value of dpi indicates higher image resolution.

The term dynamic range refers to the ratio between the brightness values of the lightest and darkest px which is the capturing device able to provide. The higher the dynamic range is, the greater variation of dark and bright spots and areas the image includes, and the truer image of the original is caught. In other words, the dynamic range is rather characteristic of the recording apparatus, than of the image itself. Comparing the lightest and darkest areas of the recorded image by means of a ratio leads to the expression of the image contrast [110].

Bit depth is a term derived from the word bit. In computers technology, one bit is the smallest carrier of information. It is binary entity, which means that it can equal only to two values – either 1 or 0. The number of bits storing the information about colour of an image is called bit depth or colour bit depth. This image parameter points out how finely are the individual colours and colour levels displayed. In the case of 1-bit image the information is stored only in one bit it carries information about $2^1 = 2$ colours – black and white, while the zero value is usually assigned to black and number one to white. Analogously, 4-bit images carry information about the $2^4 = 16$ colours shades; 8-bit images capture $2^8 = 256$ colours, etc. Hence, the higher bit depth enables describing wider range of colours. However, it goes hand in hand with higher memory requirements on computer. In computer graphics it is possible saving images from the simplest 1-bit black and white to highly realistic 24-bit ones (“True Colour”

⁶ “Dots per inch” equals to “pixels per inch”.

– about 16.8 million colours), 32-bit (“Super True Colour” – about 4.3 billion colours) 48-bit (“Deep Colour” – about 281.5 trillion colours), respectively [111].

In the context of bits is necessary to introduce the term byte – B. Typically, the 8 b clusters are joined together into a units corresponding to 1 B, and so is possible to cover 256 colours range in each point in the image (0-255), where the value 0 represents black and 255 represents white [112], [113].

5.2 Colour gamut, perception and interpretation of colours

The basic problem with displaying colours by the monitors and interpreting by printers is the point that the human eye perception ability is much more perfect. Certainly, the reason is linked with different principles of functionality of an eye, monitor and printer. Thus, there has been defined colour spaces and gamut in order to provide conclusive determination of the ranges of colours interpretations by both monitors and printers and by the human eye. Additionally, it is possible to compare these spaces with each other.

The human eye works on the principle of capturing the visible light which is the spectrum of wavelengths and corresponding colours and colour shades (Fig. 49):

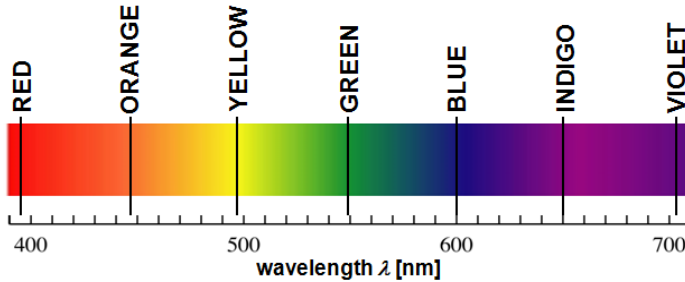


Fig. 49: Visible spectrum with the bands corresponding to the colours of rainbow.

The distribution of colours in the visible spectrum reveals that the highest sensitivity of human eye is to green colour, which is located roughly in the middle of the spectrum. Green colour is also perceived with the greatest intensity [114]. The mechanism of colour perception is related to the light sensitive rods and cones, present in human eye and through which the image is reconstructed. The rods act as a sensor of light intensity (colour hues), while the cones are responsible for colour perception. The human eye can distinguish colour range widely exceeding the displaying possibilities of monitors and colour interpretation by printers [111].

To display all these colours and hues, the chromatic diagram “CIE 1931” (Fig. 51) was proposed in 1931 by CIE⁷ on the basis of CIE triangle shown in Fig. 50:

⁷ Commission Internationale de l’Éclairage / International Commission on Illumination.

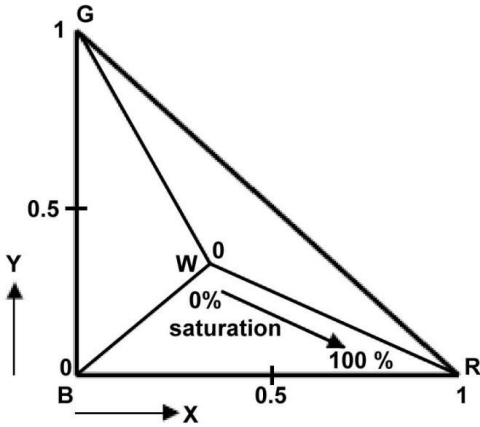


Fig. 50: Construction of the CIE triangle, redrawn from [115].

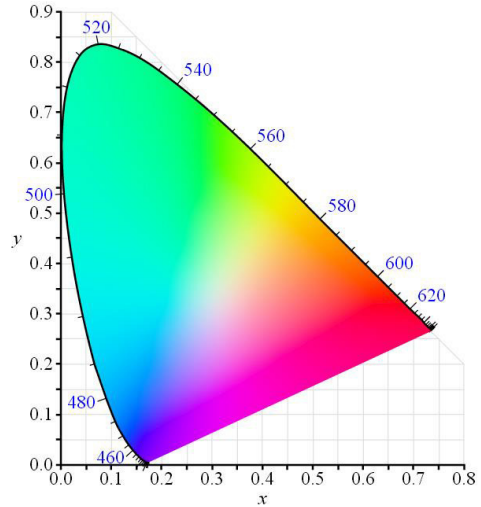


Fig. 51: Visible gamut according to CIE triangle. The values on the perimeter show wavelengths [116].

The CIE triangle is a right-angled triangle with the right angle placed at the origin of the coordinate system which is designed in order to describe the values of brightness on the Y-axis, while the X-axis has only a mathematical meaning and does not describe any colour feature. The vertices of the triangle determine the basic colour of RGB colour space: Red, Green and Blue. The intersection of the medians forms the zero point. This value is assigned to pure White colour [115].

The visible gamut is created by introducing of pure visible-light colours into this triangle perimeter, ordered in ascending manner according to their corresponding wavelengths in clockwise direction, starting at the right-angle vertex. All remaining eye-visible colour hues are organized in the inward direction of the gamut, towards to the pure white colour located roughly in the centre of the area. The resulting shape of the visible gamut is similar to a ship sail.

The essence of the construction of this diagram is the need for accurate and precise “quantification” of colour, since the human’s colour perception is subjective and thus a simple oral description of a colour is insufficient. In other words, reaching a consensus of colours seen and reproduced would always fail, without a precise definition of colours [117].

As already mentioned, the visible gamut is much wider than both gamut of printer and monitor, which are actually only small subsets of the visible gamut (Fig. 52). The reason for the existence of different printer/monitor gamut is the way how these devices interpret/display colours.

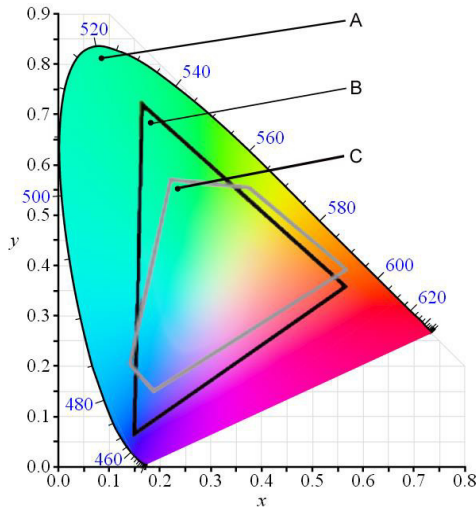


Fig. 52: Gamut comparison – region A – visible gamut, region B – RGB gamut, region C – CMYK gamut, redrawn from [119].

Monitors employ three light beams to illuminate three points (R – red, G – green and B – blue) forming a displaying pixel. Thanks to this principle of “mixing”, almost any colour can be composed. Since computer monitors work with combining of light beams, the colour mixing is additive (Fig. 53a). That means that if a hue is added to a certain colour, the resulting colour is lighter. Therefore, the displaying colour space of a monitor is called RGB gamut [118].

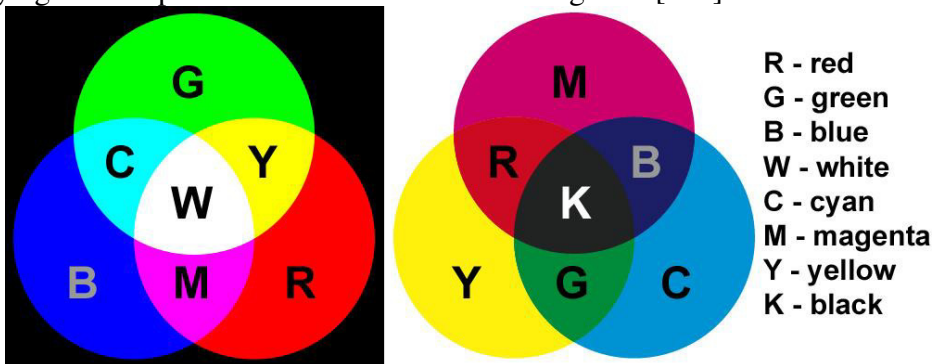


Fig. 53: Principle of colour mixing in monitors and printers [118].

The principle of printers colour interpretation is based on using pigments contained in the ink and their combinations. Unfortunately, basic ink colours are not identical with basic colours of monitor – these are achieved only upon certain composition of basic ink colours (C – cyan, M – magenta (or purple), Y – yellow and K – black), hence defining CMYK gamut. Unlike the monitors, printers work on the principle of subtractive colour mixing (Fig. 53b), meaning that with any additional colour a part of the original light is lost and the consequential colour is darker [118].

5.3 Thresholding

Thresholding (or image binarization) is the simplest method of image segmentation and it is often the very first step in the image analysis. The principle of thresholding is clear: the brightness value of each pixel is evaluated by computer and the threshold value in the histogram⁸ is searched. The histogram of the original image contains 256 brightness values - from pure black (value of 0) to completely white (value 255). As the threshold limit is considered such a brightness value, for which applies, that all lower values correspond to the background and in contrary the foreground (structure of interest) is represented by all higher values.

Thresholding converts the original coloured or grey-scaled images into a black and white image maps. That leads to suppression of useless details, like e.g. noise and to improvement of contrast of the studied structures. Despite its simplicity, this segmentation technique is very powerful; however, the disadvantage is that it must be carried out individually for each image. Often it is not possible to use the global threshold, mainly due to uneven lighting of the original pattern, or due to inhomogeneity of the image itself. Improperly selected threshold may result in partial loss of visual information about the studied structure. In practice, there is a relatively wide range of techniques based on different approaches [3], [107]-[109], [120]-[122].

5.4 Contrast modifications

According to the chapter 5.1, contrast can be described as the difference between the lightest and the darkest point in the given image. If some important details are not so clearly visible, it is necessary to enhance the image contrast artificially. These situations arise typically in the cases when the colours and brightness of the observed object and the background are similar to each other. Enhancing this difference contribute to the improvement of the image contrast and facilitate the perceptibility for the human eye, at the same time [117]. The contrast modifications are local in vast majority of situations. That means that the contrast-enhancing algorithms work with the numerical value of colour/brightness saved in the image histogram for each pixel. This modification is executed gradually for each pixel P_i of the image as follows: The currently modified pixel is assessed as the central pixel and its new value of brightness is computed by averaging the values of all P_i neighbours. Consequently, the resulting values are stored in the “modified histogram” of the image where the original pixels values (P_i) are assigned to Q_i – modified pixels. This procedure is carried out for each pixel in the image and thus the output image has its contrast modified – the finely dark pixels of the input image become darker and the original bright pixels are on the contrary lightened [3].

⁸ expression of brightness distribution in the image

5.5 Edge detection

Detection of edges between the objects and their background or in between the objects in any image is important for correct identification of features. These interfaces in images – pore boundaries, crystal surfaces or cell walls are formed by edges, which are characterized by a noticeable, almost step change of brightness in the place where the edge passes, compared to its surroundings. This phenomenon is useful for the operations dealing with edge recognition in the images [123]. For the edge detections it is mostly employed a discrete two-dimensional convolution by means of convolution masks, sometimes also called convolution kernels. From the mathematical point of view, these masks are certain numerical matrices, serving for “overlapping” the original image and consequential modification of brightness values by means of the numerical values in the matrix. This principle enables not only detection of edges and interfaces, but provided that suitable values are chosen it also possible to achieve smoothing or sharpening the image [124], [125]. The crucial condition for the coefficients of the convolution masks is that their sum must be equal to 1. Otherwise unwanted lightening of the processed image would occur [126]. Among two most used convolution masks belong Prewitt’s detector [125], [127] mathematically expressed as Eq. (22) and Sobel’s operator [128]-[129], described as Eq. (23):

$$h_p = \begin{bmatrix} 1 & 1 & 1 \\ 0 & 0 & 0 \\ -1 & -1 & -1 \end{bmatrix}, \quad h_s = \begin{bmatrix} 1 & 2 & 1 \\ 0 & 0 & 0 \\ -1 & -2 & -1 \end{bmatrix} \quad (22), (23)$$

These particular matrices detect horizontal (west-east) edges; however, both detectors are direction-independent. They are able to recognize edges in all directions, if appropriately rotated as shown by Eqs. (22.1), (22.2), (23.1) and (23.2):

$$h_p = \begin{bmatrix} 1 & 0 & -1 \\ 1 & 0 & -1 \\ 1 & 0 & -1 \end{bmatrix}, \quad h_p = \begin{bmatrix} 0 & 1 & 1 \\ -1 & 0 & 1 \\ -1 & -1 & 0 \end{bmatrix} \quad (22.1), (22.2)$$

$$h_s = \begin{bmatrix} 1 & 0 & -1 \\ 2 & 0 & -2 \\ 1 & 0 & -1 \end{bmatrix}, \quad h_s = \begin{bmatrix} 2 & 1 & 0 \\ 1 & 0 & -1 \\ 0 & -1 & -2 \end{bmatrix} \quad (23.1), (23.2)$$

The former two matrices (22.1) and (22.2) show the modifications of Prewitt’s operator for detection of vertical (north-south) and oblique-oriented (northwest-southeast) edges. Similarly, Eqs. (23.1) and (23.2) present the matrices for detections of north-south and northeast-southwest using Sobel’s operator. Beside the edge

detection, Sobel's detector also smooths mildly the original image. That makes it more universal, in comparison with Prewitt's edge-detection matrix [3], [123].

The process of convolution is a mathematical operation working with the numerical value of brightness of each pixel in the image. These values are multiplied by the coefficients of the used convolution mask adjacent to the selected pixels. The purpose of this "masking" is assigning the weighed-importance of each pixel's brightness to further processing. This principle is applied for all pixels under the convolution mask. The sum of the obtained products indicates the brightness value of a new pixel. Subsequently, the convolution mask slides over the analyzed image, and sequentially performs convolution of the entire image. The result of this procedure is determination of influence of the concerned data segment by its neighbours [130].

5.6 Binary mathematical morphology

Mathematical morphology is an approach covering a set of methods for both processing and analysis of geometrical features in the digital images. Mathematical morphology is based on set theory, stochastic and integral geometry. The most frequent and typical application range of mathematical morphology includes processing of binary images, known as binary mathematical morphology, nevertheless, some applications on greyscale images (greyscale mathematical morphology) are also possible [131], as will be discussed below.

Mathematical morphology began to develop in the second half of the 60s of 20th century, when a group of French researchers led by Georges Matheron developed and introduced mathematical techniques for analyzing spatial data from geology, later on employed as a tool of image analysis of geological and biological samples [132], [134].

Mathematical morphology in the present form is represented by a set of methods that are used in applications which require general image recognition, namely in materials research [132], as well as in industrial applications [135] or in criminology [136].

Usually, in the case of binary images, the points forming objects in the image represent a 2D plurality X , unifying the pixels with the value 1. The supplement points describing the background are united in set X^c . These pixels have their values assigned as 0 [123], [137]. The most common operations of binary mathematical morphology are listed below.

5.6.1 Erosion

Erosion is the most basic morphological operation. It can be described on an example of a binary image as a process which rewrites black pixels, neighbouring with white pixels into white ones following a predefined rule. The resulting effects on the image are slight changes in shape and size (reduction) of the features, smoothing the object boundaries or interfaces and removing point and/or linear noise of the image [3]. Mathematically said, it is the Minkowski's (vector) subtraction of a structural

element (the singleton $B=\{b\}$) from the set A – representing the original object. This mathematical operation can be written as Eq. (24):

$$A \ominus B = \{p \in \mathcal{E}^2 : p + b \in A, \text{ when } b \in B\} \quad (24)$$

The relation (24) can be interpreted in such a way, that for each point (px) of the image p , lying in 2D Euclidean space \mathcal{E}^2 is verified, if the result of all possible $p + b$ summations lies within the set A . If the condition is fulfilled, the SW assigns the value of the tested p as 1 in the resulting image (white colour), otherwise the value is set as 0 and the point is rendered by black colour [123]. When applied on image, erosion removes the outer black pixels, undesirable thin contours, tiny protrusions, noise of the image or similar non-homogeneities. The effect of erosion on the resulting feature shape is shown in Fig. 54:

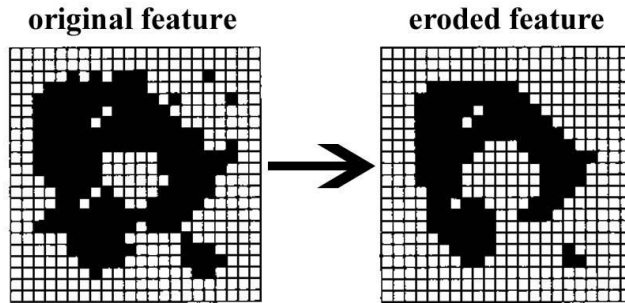


Fig. 54: Alteration of feature shape after eroding, redrawn from [3].

5.6.2 Dilation

Dilation is mathematical opposite of erosion. Nevertheless, it is important to keep in mind that the dilated object is not transferable back into its initial state by means of erosion and vice versa [138]. Similarly to the case of erosion, the white pixels surrounding the edges of the objects are changed into black pixels, according a defined rule. That results in smoothing the boundaries and “sealing” small holes or bays. According to a definition proposed in [123] dilation is in its essence the erosion of the supplement of the set A . Mathematical notation of dilation is as follows:

$$A \oplus B = \{p \in \mathcal{E}^2 : p = a + b, a \in A, \text{ and } b \in B\} \quad (25)$$

Meaning of the used symbols is similar to the previous case with Eq. (24). Dilation performed on the same object as erosion is shown in Fig. 55:

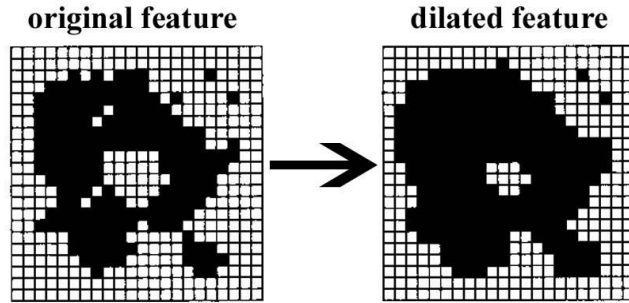


Fig. 55: Scheme of the effect of dilation, redrawn from [3].

5.6.3 Opening and closing

Since both above mentioned cases cause size alterations of the features, as it has been shown above, it is common that the dilation and erosion are used gradually, as complementary operations. This leads to a slight change in the shape of an object while keeping approximately the same size. If the image is eroded and then dilated, the approach is called opening. Conversely, when the dilation is followed by erosion, the operation is called closing [3], [137]. Opening and closing are often used several times. The purpose is to remove fine details in the image and not change the original shape of objects. Comparison of these two methods offers Fig. 56:

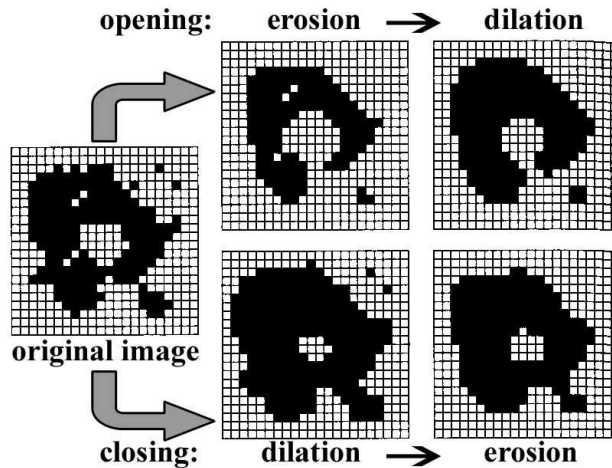


Fig. 56: Opening vs. closing, redrawn from [3].

5.6.4 Euclidean distance map

Reshaping objects induced by either dilation or erosion brings one major problem. An arbitrary modification of an object size by means of dilation or erosion causes non-isotropic changes of the modified objects. This happens due to the shape of pixels, which are squares in fact. As it is generally known, the distance from the centre of a square to its sides is shorter than the distance from the same point to the square

vertices. In other words, when repeated several times, both erosion and dilation of a circular object, never preserves the original shape – resulting shape will always be different from the circle and rather will look like a square with rounded corners, as shown in Fig. 57. This figure shows a situation when the original object – the dark grey circle – has been eroded 25 times (black shape inside the original circle) and then dilated (outer light-grey area).

Due to this phenomenon the image analysis applies also Euclidean distance map (EDM) [3], [123], [139]-[140]. It is a computational method assessing Euclidean distance in between the pixels. Beside the numerical output, the result is regularly presented as the visual EDM image. Typically, EDM calculate the Euclidean distance d_{ij} from each white, background representing pixel with the value $b_{pq} = 1$ in the i^{th} row and j^{th} column of the image consisting out of the pixel raster of p rows and q columns to the closest black foreground pixel with the value $b_{pq} = 0$. Consequently, the computational algorithm assigns the same shade of grey to the pixels with equalling white-to-closest-black distances in such a way, that with the increasing distance the brightness decreases. Thus, the white-black gradient is created, helping the observer to distinguish the same or similar distances easily. Mathematically, this can be written as distance calculation by means of Eq. (26):

$$d_{ij} = \min_{1 \leq p, q \leq N} \left(\sqrt{(p-i)^2 + (q-j)^2} \mid b_{pq} = 1 \right) \quad (26)$$

Fig. 58 shows, how the original circular object (in the picture dark-grey annulus) is changed after enlarging (the inner light-grey annulus) and shrinking (black circle) by means of the principles of EDM. It is obvious that any size alterations based on EDM are isotropic and therefore do not affect the original shape of the objects. Beside the applications in references mentioned above, the principles of EDM can be utilized also e.g. for looking for tessellation nuclei for modelling the structure of foams planar sections [13], [63].

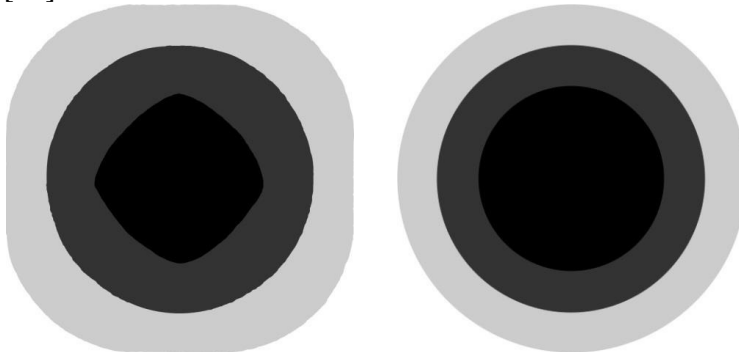


Fig. 57: The effect of dilation and erosion on the resulting shape of the initially circular object, redrawn from [3].

Fig. 58: The effect of EDM on the shape – both enlarging and shrinking preserve the shape of the original object, redrawn from [3].

5.6.5 Skeletonization

Skeletonization, sometimes also mentioned as extraction of the central axis [123] or thinning process [141] is the special case of erosion, which transforms planar objects into their skeletons (spinal curves) as it can be seen in Fig. 59:

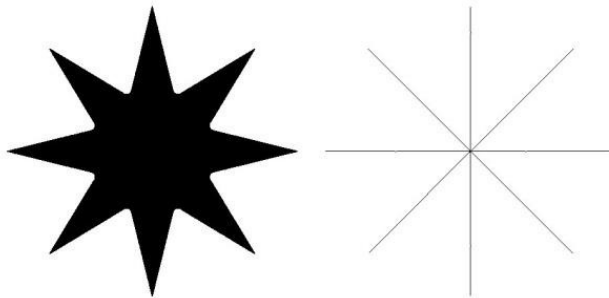


Fig. 59: *Eight-pointed star and its skeleton.*

This operation is in fact the intentional simplification of the original image used with the aim to reveal the shape, size, or orientation of the features in the image. The typical application of skeletonization is the extraction of the tessellation from the image of planar cut through a cellular structure [3], wide application range can be also found in computer graphics [142]-[144].

The principle of skeletonization can be explained on an imaginary meadow (the object), which is ignited around its whole perimeter at the same time and the fire is spreading in all directions at constant speed. The place, where two or more fires meet each other, belongs to the skeleton of the object. The scheme of this concept is illustrated in Fig. 60:

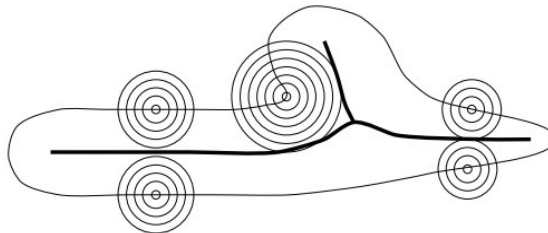


Fig. 60: *Principle of skeletonization [123].*

5.7 Greyscale mathematical morphology

The already mentioned operations of binary mathematical morphology can be also employed for the processing of images with more brightness levels. This extension can be interpreted by means of topography. This explanation is based on the concept of the greyscale image as a hypothetic model of landscape, where brightness indicates the altitude. Then each light and dark spot in the picture shows the hill and valley, respectively. Applying the morphology reveals these extremes in the images. The important operations for the greyscale mathematical morphology are *min* and *max* operations. Erosion assigns the minimum brightness value available in the immediate vicinity of the currently examined pixel to this pixel of the input image, while

dilatation has the contrary effect. The structural element is not only a singleton, but the function of two variables, assigning a weight to each pixel around the selected pixel. In the case of maxima counting is the value of the structural element added and subtracted for minima count [123].

5.7.1 Watershed segmentation

The originally geographic term watershed can be figuratively applied also to image analysis [3], [145], [146]. Segmentation method based on watershed is based on the aforementioned notion of greyscale image as a topographic map showing the hilly landscape with valleys. If the hills are sprinkled by raindrops, water flows down to the valley. In areas between two peaks (saddles), where two springs meet each other can be find a line which, after its removal, creates a boundary between the hills [143]. This principle can be typically used for separation of particles which are touching each other in the image (Fig. 61). These can be analyzed either directly as a greyscale image, or after thresholding as a black and white image. Firstly the saddles are found with EDM, then the lines of touch are removed and thus, the cells are separated.

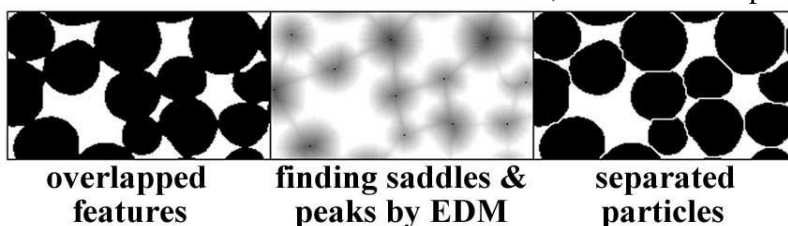


Fig. 61: Watershed segmentation [147].

EXPERIMENTAL

6 Materials

In general, foam materials can serve as a representative of the materials with – from the stereological point of view – interesting internal structure. Therefore, flexible polyurethane foams consisted out of opened pores has been chosen for the experimental work.

Taking a brief look at the chemical composition, the group of polymers known as polyurethanes (PUR) include the materials that incorporate the carbamate group (-NH-COO-) in their macromolecular chains, as well as other functional groups, such as amide or urea. However, two main PUR types are ether- and ester-based foams. The name “polyurethane” is derived from ethyl carbamate, known as urethane. The internal bubble structure of PUR is formed during the chemical reaction of monomers, provided that the reaction system contains also water, which mediates evolving the foaming agent (CO₂).

Application area of these materials follows their physical-mechanical properties – e.g. its flexibility predetermines the application in upholstery, the noise dampening properties enables the utilization of this material in soundproofing applications, etc.

As it has been already mentioned, there can be find the link between the properties and the internal structure. Hence, ten types of commercially available soft

polyurethane foams were chosen with the intention to cover as wide range of densities as possible. The list of the analyzed materials is shown in Tab. 1 below:

Tab. 1: *Overview of studied flexible PUR foams ordered according to the material density in ascending manner.*

sample		density [kg/m ³]	resistance to compression 40% [kPa]
#	material name	(ČSN 645411 & DIN 53420)	(ČSN 645411 & DIN 53577)
1	2015	20	1.5
2	2340	23	4.0
3	2545	25	4.5
4	3050	30	5.0
5	3545	35	4.5
6	4070	40	7.0
7	HR 4250	42	5.0
8	PANTERA 100	50	2.8
9	HR 5050	50	5.0
10	CMHR 6052	60	5.2

All materials; except one foam, have a 4-digit code in their names. This number encodes two physical properties of the material. While the first two digits correspond with the material density, the second pair of numbers describes the tenfold of resistance to compression. The letters have following meaning: HR – high resilience, CM – reduced flammability. Foam PANTERA ®100 contains high portion of latex. The material properties are declared by the manufacturer and have been determined in compliance with ČSN and DIN standards. All the examined materials have been provided by HG Style s.r.o. Kojetín.

7 Methods

7.1 Computed X-ray microtomography

7.1.1 Instrumentation

All the experimental data have been acquired employing X-ray micro tomograph SkyScan 1174 (further referred as CT) from Bruker. The device is shown in Fig. 62. The principles of CT, including a scheme of the machine (Fig. 46) are summarized above, in chapter 4.3 of the theoretical part.

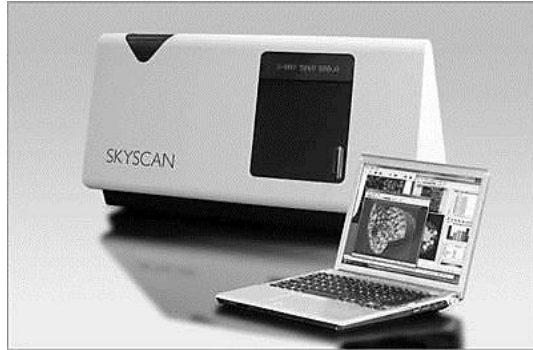


Fig. 62: SkyScan 1174 X-ray microtomograph [148].

The device operates with an X-ray source (20-50 kV), providing the power up to 40 W. The attenuated X-ray radiation, passing through the sample is detected by means of 1.3 megapixels CCD chip coupled to scintillator by lens with zoom range 1:6. This arrangement of CT allows reaching a spatial resolution of less than 10 μm corresponding to near $1 \times 10^{-6} \text{ mm}^3$ voxel size⁹. The sample stage is designed for holding the samples of 5-30 mm in diameter and up to 50 mm in length (height). Reconstruction of the structure is performed using Feldkamp algorithm [149]. Manual pre-measurement adjustment mode of CT allows customization of the parameters and obtaining the optimal contrast at the detector, according to the sample's nature.

7.1.2 Sample preparation

All examined materials were provided in the form of slabs, dimensionally exceeding the size of the sample cell of the CT machine. Cylindrical samples for the CT measurements (Fig. 63), resembling the shape and size of a cigarette filter, were prepared using a rounded leather punch. The samples were taken from a random place, but far enough from the edges in order to minimize distortion of the material when hit by the punch. The dimensions of the samples varied in the height ($\sim 30 \text{ mm}$), as the original PUR slabs were not constantly thick, nevertheless the diameter was 8.0 mm in all cases. The samples were attached directly to the rotational sample stage by double-sided tape.

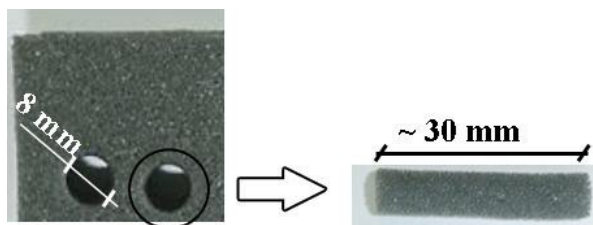


Fig. 63: Preparing the samples for CT scanning.

⁹ Voxel is a volumetric analogy to pixel.

7.1.3 Scan parameters

Although the CT accompanying SW offers fully automated mode of scanning with all parameters preset on certain values, it is not suitable to use these parameters for the measurements universally. The crucial factor specifying the need for manual adjustment is unequal absorption of X-rays of various materials and material phases.

Thus, all PUR samples were scanned at individually preset scanning conditions that are summarized in Tab. 2. The complete record (*.log file) of the scan parameters for the sample HR4250, including also the reconstruction adjustments is enclosed as the appendix A1. The values of voltage and current – determining the actual power of the X-ray tube, as well as the exposure time, were chosen on an individual basis by trial-and-error approach for each material with the intention to achieve the optimal contrast of the sample scan visualised on the computer monitor. In other words, the goal was to find such a combination of parameters to get the brightest possible background and the darkest possible sample. Since the dimensions of all samples were more or less the same, the other parameters referred in the overview were selected the same for all scans. This ensured constant image resolution and comparable image sharpness.

The other optional scan parameters which is worth considering before each scan are “flat-field correction”, “360° scanning” and “random movement”.

Flat-field correction is a tool useful for correcting the differences in brightness of the individual pixels caused by variations in sensitivity of the detector pixels. The SW takes as the reference value the brightness of the preview image background. Usage of this correction prevents from unwanted image noise; therefore it was performed before all measurements.

The function 360° scanning is suitable to use for analysis of non-homogenous and non-symmetric samples but doubles the total scanning time. In other cases, including also the examined PUR samples, it is sufficient to use only 180° scanning.

The last parameter – random movement – controls small vertical movements of the sample stage after given number of rotation step, which helps avoiding the occurrence of the ring artefacts and reduces the errors caused by dusty detector. The nature of the scanned materials and the CT conditions did not require this correction.

Tab. 2: Overview of studied flexible PUR foams ordered according to the material density in ascending manner.

Sample:	2015	2340	2545	3050	3545	4070	HR 4250	PANTERA 100	HR 5050	CMHR 6052
Voltage [kV]	24	25	24	24	24	24	24	24	24	24
Current [μ A]	642	611	661	661	642	661	648	636	661	648
Image px. size [μ m]	14.58	14.58	14.58	14.58	14.58	14.58	14.58	14.58	14.58	14.58
Exposure time [ms]	9500	9800	10000	11100	9000	11000	9000	9100	11200	9000
Rotation step [$^{\circ}$]	0.2	0.2	0.2	0.2	0.2	0.2	0.2	0.2	0.2	0.2
Frame averaging	5	5	5	5	5	5	5	5	5	5
Scan duration	12:28:21	12:51:13	13:06:44	14:31:44	11:49:25	14:23:55	11:49:26	11:57:49	14:39:01	11:48:34

7.1.4 Slices reconstruction

The output of each scanning process was a set of 16-bit *.TIFF images (Fig. 64) – grey projections (radiographs) of the samples for each rotation angle – see Tab. 2, 6th row. These images were computationally transferred into transverse cross sections (Fig. 65), which represented virtual thin slices of the structure superposed on each other. The grey contours in the image (Fig. 65) represent the structure of pore boundaries (struts), while the white areas depict the air inside the individual pores. Since the slice thickness correlates with the px size, chosen at the acquisition phase and thereby with the grey projection resolution, the resulting single-slice thickness was 14.577 μ m in all cases.

The computational slice reconstruction process itself was carried out by means of NRecon software, employing the principles of back projection. This approach is one of the simplest ways of the structural image reconstruction. Basically, it is an algorithm for converting the X-ray intensity value transmitted through each voxel into the corresponding X-ray absorption value. The essential condition for this conversion is multiple transmissions of X-rays through each voxel at various angles. In principle, this reconstruction is possible to achieve by several ways, e.g. by means of Fourier transform; however, the available CT utilizes Feldkamp algorithm, as it has been already mentioned above. Each absorption value corresponds to the specific shade of grey which is assigned to each pixel by the reconstruction SW according the results of transformation, so that forming the reconstructed image.

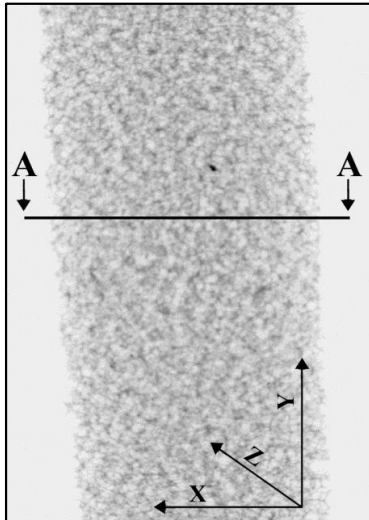


Fig. 64: XY plane grey projection of the sample 4070. The black line A-A denotes one reconstructed slice.

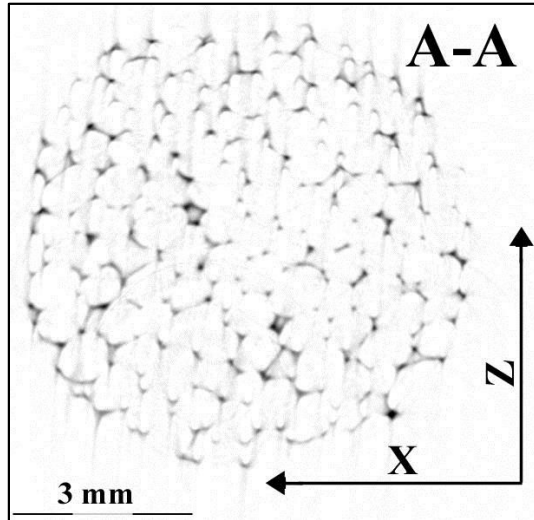


Fig. 65: Reconstructed transverse cross sectional slice of the sample 4070 corresponding with the line A-A in Fig. 64.

7.1.5 Optional reconstruction parameters

Obtaining a precisely reconstructed dataset almost regularly requires pre-adjustment of several reconstruction parameters before the reconstruction procedure itself. These parameters are “Smoothing”, “Misalignment compensation”, “Ring artefact reduction” and “Beam-hardening correction”. It is not always necessary to employ all these corrections together prior to the reconstruction, a suitable combination of only some of them is frequently sufficient. The utilization of the parameters is controlled manually by the user, thus a certain level of user’s experience is necessary.

Smoothing parameter includes several integrated smoothing kernels to be optionally used mainly for noise reduction within the reconstructed image. On the other hand an improper usage of it may cause in blurring, noticeable mainly in fine structure details.

Misalignment parameter compensates possible misalignment during acquisition. Wrong alignment compensation would cause tails, doubling or blurring in the reconstructed dataset. Equally to the previous parameter, it is advised to find the optimum in try-and-error fashion.

Ring artefacts are unwanted concentric circles appearing from time to time in the reconstructed images. The most common reasons of their origin are either presence of dust on the camera or presence of a defect pixel on the detector. The correction of the rings can be done by built-in filters, offering the user to choose the depth of compensation within 20 grades. As in the previous cases, the careless utilization of this correction may induce additional ring artefacts. However, this type of imperfection is rather typical for dense objects than for the soft, light dense foam. The appearance of ring artefacts during the reconstruction of low dense materials can be reduced or even prevented by setting a small scan step and increasing the frame

averaging number. That in other words means that the probability of ring artefact generating decreases with increasing time of scanning.

The last discussed imperfection is a phenomenon called beam-hardening. This relates to a certain polychromatic character of the X-ray source. Simply said, the source generates the X-ray photons with varying energy. While the low-energy photons are attenuated easily by the sample, the photons with higher energy are attenuated later on their way through the sample. As a consequence, bright and dark streaks appear in the reconstructed images [150]. Although these bands are typical for the high dense materials with high attenuation coefficient such as bones or metallic materials, some slight corrections are often necessary also for soft foams.

Finally, after each reconstruction all the reconstruction parameters are saved in the reconstruction protocol, which is the part of the *.log file in appendix A1.

After the reconstruction procedure of each sample a set of images (further referred as the image dataset) representing superimposed thin slices of the samples were subjected to the image analysis.

7.2 Structural analysis – CTAn software

CTAn (CT-Analyser) is an application provided by Bruker with the SkyScan CT machine. This SW is intended for measuring quantitative parameters and constructing visual models from scanned datasets obtained with the CT.

7.2.1 Region and volume of interest

CTAn processes the raw images in several steps. At the beginning it is important to define the appropriate region of interest (ROI) – see the light grey circle in (Fig. 66a), which is an area defining usually only a small, representative part of the investigated structure, containing the sample exclusively. All further operations are consequently applied only to this ROI (Fig. 66b). The main significance of ROI lies in two reasons. Primarily, the raw, full field of view (FFOV) images, obtained by the reconstruction procedure beside the meaningful structural data always include also a high content blank space (Fig. 66a). Not excluding this blank space in the image analysis logically lead to the distortion of the result. Moreover, the second benefit of ROI is considerable reduction of the image dataset size and related reduction of the computational demands. The spatial analogy of planar ROI is volume of interest (VOI), which is usually interpolated automatically from the single ROI defined by the user.

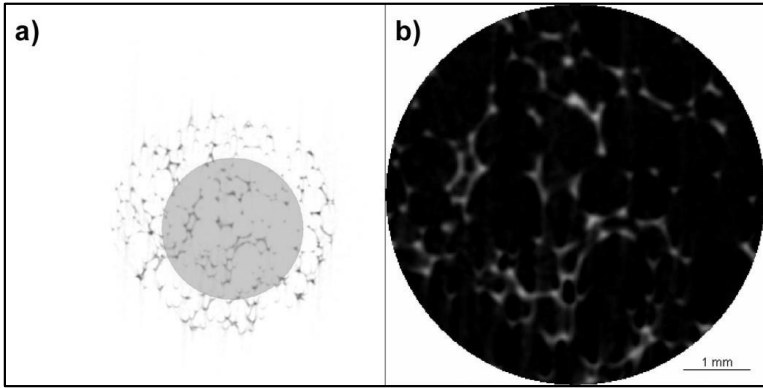


Fig. 66: a) FFOV image of a reconstructed slice (Sample HR4250) – the sample is surrounded by air; selected round-shaped ROI is highlighted by light grey circle, b) ROI saved from the FFOV image.

7.2.2 Thresholding

Thresholding is the operation following the ROI/VOI definition. The main intention of this sub-step is to prepare the binary images necessary for the further structural analyzing. In principle two variants of binarization can be applied:

- 1) Assigning the white colour to the struts and black to the pores,
- 2) assigning the white colour to the pores and black to the struts.

Both variants are possible and can be optionally performed, depending on the user's choice and the nature of the sample. Considering the image datasets contrast (Fig. 67a), all images were binarized according to the option 1, leading into the transformation of the original image datasets into the binary ones, where the pore sections were represented by continuous black area and the pore boundaries were observed as the discrete white speckles, as shown in Fig. 67b. This operation employed a general global thresholding method, which was found to be adequate for this purpose.

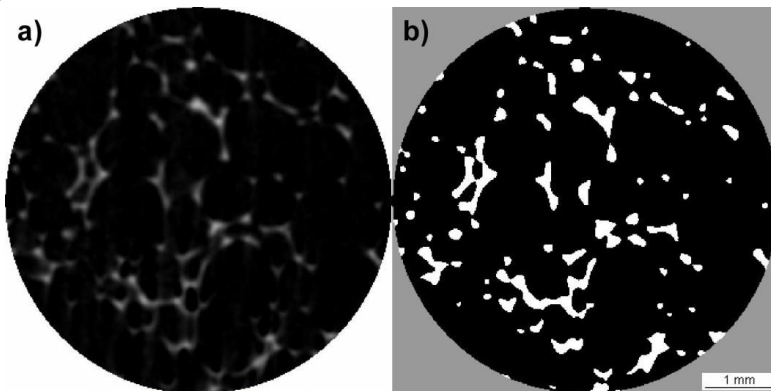


Fig. 67: a) Detail of ROI corresponding with Fig. 66b, b) binarized ROI image where white areas represent the struts.

To explain the importance of the appropriate binarization option, one crucial remark has to be made. The CTAn software interprets any white pixel in the image as a part of an object (foreground), whereas the black pixels are assigned to a vacancy (background). This logic is strictly obeyed during the consequent 3D structural analysis. Therefore, one has to bear it in mind in order to gain the correct results of the consequent structural analysis. Basically, the software enables to analyze both objects and background in the binary images by means of two types of calculations – structure thickness and structure separation, as will be explained further.

7.2.3 Structural analysis

Structural analysis was performed in Custom processing mode, which is a dataset processing interface within the CTAn software dedicated for the user-defined image operations such as smoothing, mathematical morphology (dilation, erosion) arithmetical operation on images (additions, subtractions) and last but not least it includes the 2D (ROI related) and 3D (VOI related) analysis plug-ins.

The 3D analysis plug-in incorporates calculations of twenty structural characteristics which can be opted and combined on the basis of the analysis demands. The key parameters for the 3D analysis of the soft polyurethane foams with the interconnected pore network were:

1) Total VOI volume (TV) [mm^3] and Object volume ($Obj.V$) [mm^3]

Total volume is the summation of all voxels' volumes (black and white) within the VOI, meaning the total volume subjected to the analysis. Object volume sums up only the white pixels belonging to the objects within the selected VOI. The difference between these numbers expresses the volume of vacancies.

2) Total VOI surface (TS), [mm^2] and Object surface ($Obj.S$), [mm^2]

Total surface is the surface area of the VOI in 3D, Object surface gives the surface area of all the solid objects within the VOI.

3) Surface area density (S_V), [mm^2/mm^3]

Surface area density is the ratio of solid surface to volume measured in 3D within the VOI. S_V or “specific surface” is one of the basic parameters useful for characterising the structures (see Eq. (4) and Eq. (5) in chapter “1.6 Basic stereological measurements”).

4) Structure thickness ($St.Th$), [mm]

Local thickness for a point in solid was defined by Hildebrand and Ruesegger [151] as the diameter of the largest sphere which fulfils two conditions:

- the sphere encloses the point (but the point is not necessarily the centre of the sphere);
- the sphere is entirely bounded within the solid surfaces.

The method is based on distance calculations within the objects, starting with skeletonization to identify the medial axes of all features. Then the “sphere-fitting” local thickness measurement is made for all the voxels lying along this axis. CTAn outputs a histogram of thickness with an interval of two pixels.

5) Structure separation ($St.Sp$), [mm]

This parameter is an analogy to $St.Th$ determination with the difference that it is applied for the black pixels (space) instead of white objects within the VOI.

6) Porosity (P_o) [%]

Percent porosity is one of the most meaningful structural characteristics of porous media such as the investigated polyurethane foams. Porosity is defined as the percent of voids within the VOI.

All computed parameters were outputted in the form of the analysis protocol in *.csv file, comfortably processible in a spreadsheet editor. The specimen of the protocol is enclosed as the appendix A2, the above-discussed parameters are highlighted.

7.3 Structural analysis – tessellation approach

Employing Voronoi tessellation as a tool for pore size estimation was chosen in order to process and analyze the individual images of slices through the investigated polyurethane foams, captured by CT in a different manner than offers the CTAn analysis.

This technique, previously tested as the feature-size estimation method from images of planar surfaces [13] and sections through a porous material [63], was used separately, but with the intention to verify the results obtained in this way with the results achieved by CT.

Similarly to CT method, the beginning of the analysis starts with the definition the ROI to avoid the needless blank space around the sample and the binarization of the image dataset prior to the further image analysis and following Voronoi tessellation computations. However, the further steps of this technique differ from the structural analysis via CTAn, as it will be described below. The most substantial difference between the CT and tessellation technique is the fact, that this approach does not determine the 3D distribution directly. Since it works with the individual images, which are in fact only 2D sections through the studied material, the method is capable to provide only area distribution of planar sections through the pores. The required 3D distribution must be found by means of model, which fits the experimentally acquired area distribution most satisfactory. The individual steps of this technique are illustrated below.

7.3.1 Raw image pre-processing

At the very first step there was a need to pre-process the raw images. The aim of this procedure was to transform the original 16-bit *.TIFF images containing 255 shades of grey (Fig. 68) and lot of unnecessary information such as noise and blank space into the simple binary images, carrying only the meaningful and representative structural information. All these procedures were performed employing the open-source image-editing SW ImageJ. The first operation was removing the blank space around the sample itself. This was done by simple cropping the original image (Fig. 68) – in the image indicated by the black square:

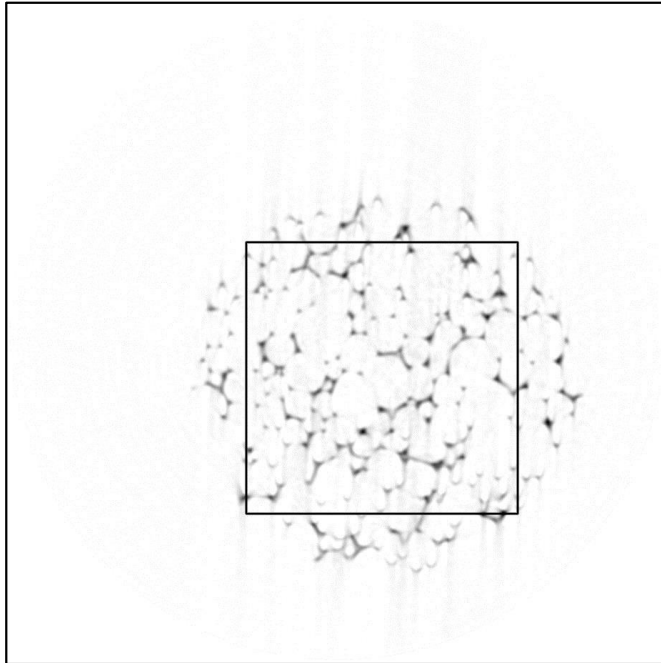


Fig. 68: FFOV – reconstructed image from CT (sample HR4250) – the sample is surrounded by blank space.

The resulting cropped image (Fig. 69), defining the ROI, was consequently subjected to enhancing the contrast of very fine image details. By means of Shadow filter plug-in a shadow effect, with light appearing to come from a certain direction was applied to the images. In Fig. 70 the northeast (light coming from the northeast direction), east and southeast shadow commands were gradually applied and the individual images were summed up into Fig. 70. This resulting image reveals that the originally pale strut contours, which are almost invisible for the observer in some areas, became darker and thus they are better prepared for the following binarization. On the other hand, one can notice that this approach slightly increases the image noise.

Final step – the image thresholding was carried out using default global thresholding adjustment of the SW. This binarization was found to be sufficient for both removing the noise, while preserving the original shape of the struts. The noise of the image was removed by means of dilation. Such a binary image (Fig. 71) was ready for further structural analysis. This pre-processing procedure was applied automatically to all images in all datasets with the great help of macros and batch tools implemented in ImageJ.

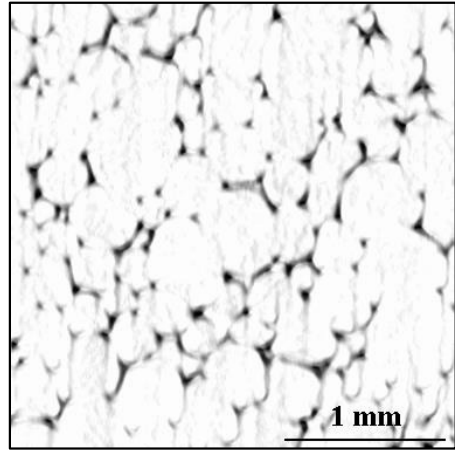
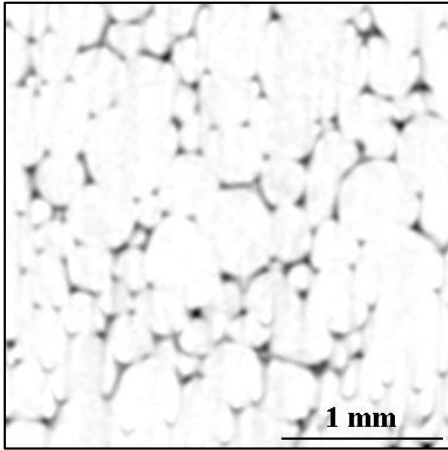


Fig. 69: Cropped reconstructed image; Fig. 70: Enhanced contrast of the image the image corresponds with the black square area in the foregoing image.

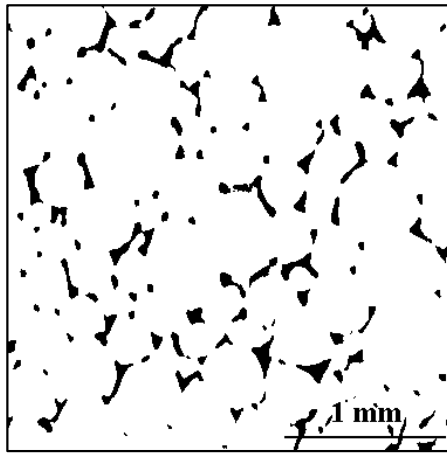


Fig. 71: Thresholded image.

7.3.2 Tessellation computation

The binarized images served as the starting point for the Voronoi tessellation computations. The goal of this technique was to reconstruct the pore sections boundaries pursuant to the dislocation of the strut sections (black areas) and therefore to reconstruct and quantify the individual pore sections.

Firstly, the EDM computation was carried out. The graphical expression of the EDM result is shown in Fig. 72. The calculation, based on the Eq. (27), assesses the distance between all white pixels to their closest black neighbour, which are highlighted by red colour (see Fig. 72). The equal distances can be distinguished by the same shade of grey, assigned to the pixels according to the rule that the longest distance (between the white and the closest black pixel) relates to the lightest shade. The areas with the greatest distance to any black pixel (in the image completely white) were found as the EDM maxima and further considered as the centres of the individual

pore cross sections. Assuming that the air bubbles, forming the inner volume of pores, grow in isotropic manner, it is possible to place the centres of inscribed circles into these EDM maxima, as it is shown in Fig. 73:

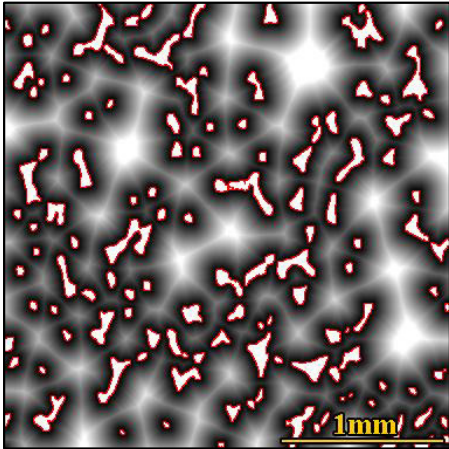


Fig. 72: EDM – the lightest area represent the centres of pores cross sections.

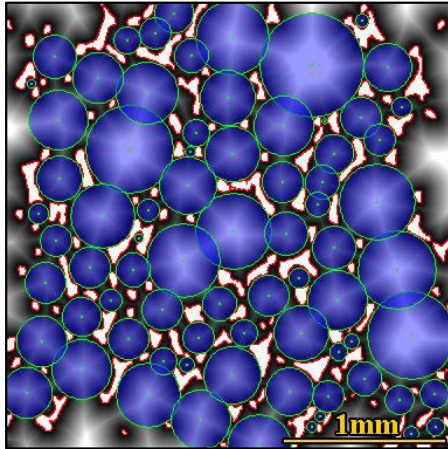


Fig. 73: EDM maxima approximated by the centres of circles inscribed to the individual pores cross sections.

These points were in the last step used as Voronoi tessellation nuclei (generators) and the tessellation-based pore cross section structure was estimated, as it is shown in Fig. 74. Note that the outer cells were erased in order to prevent from the edge phenomena. As it is apparent from Fig. 74, the resulting network of cells approximates the cells boundaries relatively well. Since the individual cells have finite dimensions, this approach enables also to estimate the pore cross sections size distribution in 2D. The computation was executed for all cross sectional images in all dataset and the acquired numerical values were put together, forming the total distributions of pore cross section areas.

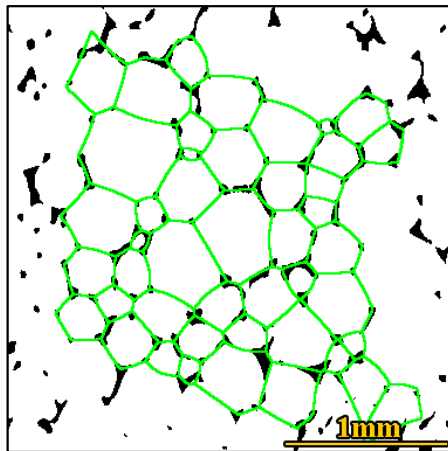


Fig. 74: Voronoi Tessellation network as the approximation of pores cross sections boundaries.

7.4 Model of 3D structure

Although the tessellation approach offers the possibility to determine the pore cross sections distribution, this planar characteristic is insufficient for the structural description of a 3D object. Thus, the pore volumes and their distribution were estimated by computer simulation.

The model, designed in Excel datasheet, assumed a set of spheres with the normal distribution of their radii, characterized by the mean radius $\bar{E}r$ and standard deviation σ_r , representing a virtual pore sizes distribution. Such a set contained the same number of spheres as was the count of cross sections in the above-mentioned total 2D distribution of pore cross sections (the total number of spheres was in the order of thousands). Provided that these virtual spheres were placed in space in such a manner, that their centres were aligned on a “zero” line, a virtual cutting plane X with the uniform distribution of distance in interval $\langle 0; \bar{E}r + 3\sigma_r \rangle$ was generated¹⁰. Always, when the sphere was intersected by the plane X, the related cross section area was computed. This led to obtaining the model distribution of pores cross sections for given $\bar{E}r$ and σ_r . Finally, these parameters of the experimental distribution were found employing the principle of searching the lowest sum of squares between the model and experimental distributions by means of Monte Carlo approach, as shown in Fig. 75:

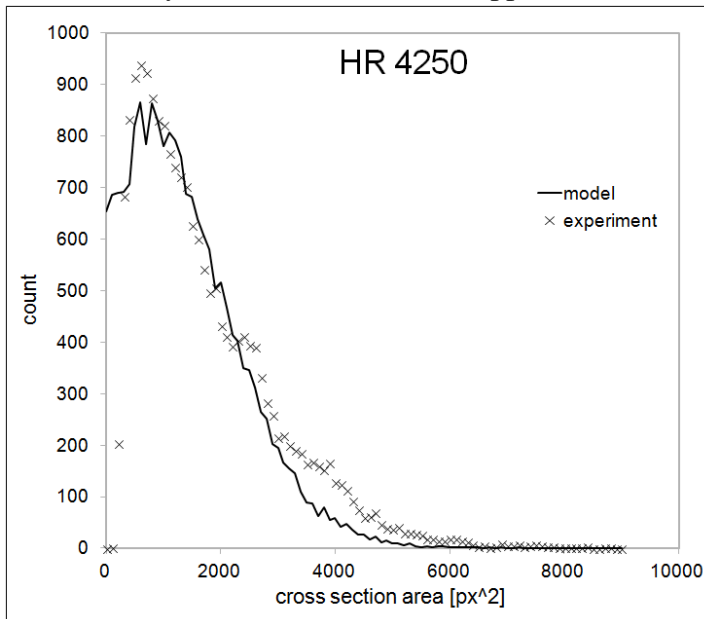


Fig. 75: Experimental data (sample HR4250) extracted from the tessellation networks fitted by the model curve – virtual distribution of pore cross section area with the parameters μ and σ found to be the closest to the real distribution – model output.

The principle of the model construction is schematically sketched in Fig. 76:

¹⁰ Note that the value $\bar{E}r + 3\sigma_r$ corresponds to the maximum sphere radius.

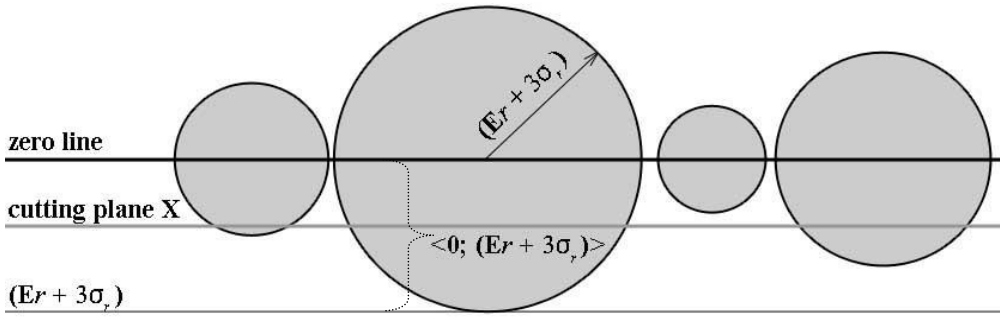


Fig. 76: Scheme of the structural model – the interval $\langle 0; Er + 3\sigma_r \rangle$ determines all possible positions of the cutting plane X.

8 Results and discussion

8.1 CT vs. Voronoi tessellation

As it has been discussed above, the set of ten samples of polyurethane foams were subjected to the determination of pore size distribution by the CT and estimation of the distribution by means of Voronoi tessellation and consequent modelling the structure.

The figures (Fig. 77, Fig. 79, Fig. 81, Fig. 83, Fig. 85, Fig. 87, Fig. 89, Fig. 91, Fig. 93 and Fig. 95) illustrate the graphical comparison between the ROI used for computation of the structural parameters in CTAn software and the ROI used for estimating the structure via Voronoi tessellations.

The tables (Tab. 3-Tab. 12) sum up the structural parameters determined by the CTAn – namely porosity – Po , [%] and structure separation – $St.Sp$ [mm], which defines the mean linear dimension of the porous structure and found model parameters – the radius of mean-size pore μ [mm]¹¹, standard deviation of radii σ [mm]¹² defining the width of the distribution and dimensionless Δ^2 – sum of least squares describing the difference between the model curve and experimental data. Finally, the four mean pore size EV [mm³]¹³ values are listed:

- 1) EV_{CT} – mean pore volume based on the $St.Sp$ value measured by CT scan and further computation of the structural characteristics.
- 2) EV_1 – mean pore volume calculated from μ value.
- 3) EV_2 – the arithmetical average of individually calculated “model” pore volumes corresponding to the found model parameters μ , σ and Δ^2 .
- 4) EV_3 – mean pore volume transferred from EA [mm²] (mean pore section area) calculated by means of Voronoi tessellation network from the individual cells. This computation is based on ASTM E112 standard [37], which proposes the equation Eq. (12) – see chapter 1.7 in Theoretical background section.

These results are put into context with the material characteristics declared by the supplier of the materials – density ρ [kg/m³] and resistance to compression Ω_c (40%) [kPa].

The comparisons between the experimental (CT) and model size distribution in terms of linear pore dimensions for the individual samples show the figures (Fig. 78, Fig. 80, Fig. 82, Fig. 84, Fig. 86, Fig. 88, Fig. 90, Fig. 92, Fig. 94 and Fig. 96).

^{11,12} μ refers to previously mentioned Er and σ refers to σ_r

¹³ Note that all discussed EV calculations except the EV_3 are based on the presumption of strictly spherical shape of the pores.

8.1.1 Sample HR4250

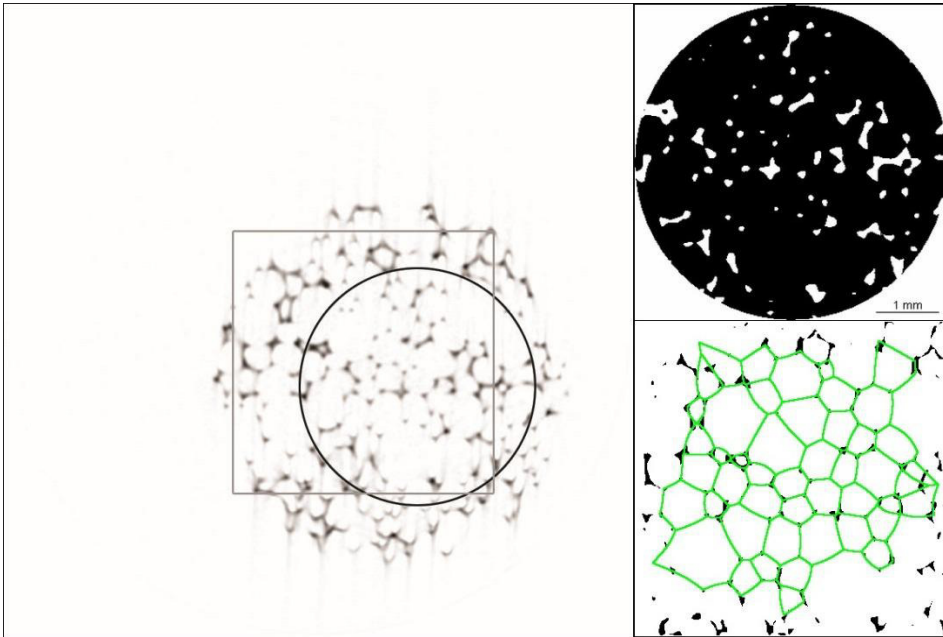


Fig. 77: Left: original FFOV of reconstructed single slice image (HR4250) with the highlighted ROIs – circular used for CT, square used for VT method; Right up: detail of the CT-ROI applied on the binarized image, magnified 1.1x, the scale bar applies for both ROI details; Right down: VT network placed over the binarized image within VT-ROI.

Tab. 3: Comparison of results from CT and VT + model parameters – Sample HR4250.

a) Material characteristics			b) Computer tomography summary		
Sample	ρ [kg/m ³]	Ω_o (40%) [kPa]	P_o [%]	$St.Sp$ [mm]	EV_{CT} [mm ³]
HR4250	42	5.0	92.117	0.773	0.242
c) Voronoi tessellation/model estimation summary					
μ [mm]	σ [mm]	Δ^2 [-]	EV_1 [mm ³]	EV_2 [mm ³]	EV_3 [mm ³]
0.344	0.096	190136	0.170	0.211	0.281

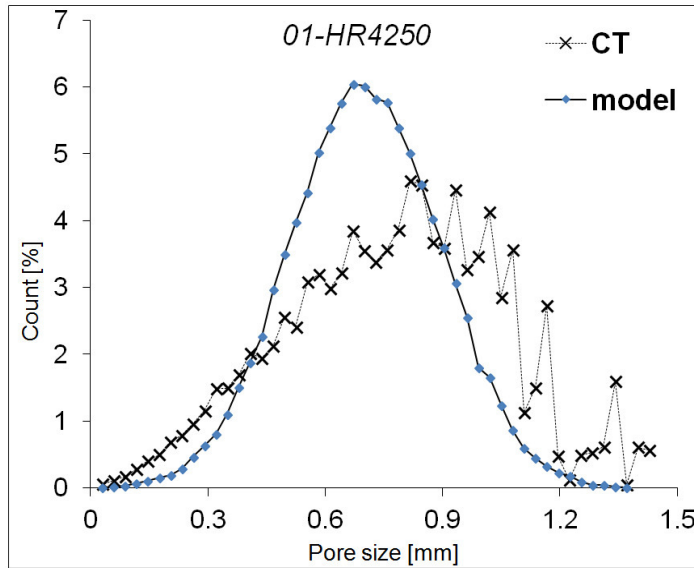


Fig. 78: Comparison of measured (CT) and estimated (model) pore size distributions – HR4250.

8.1.2 Sample CMHR6052

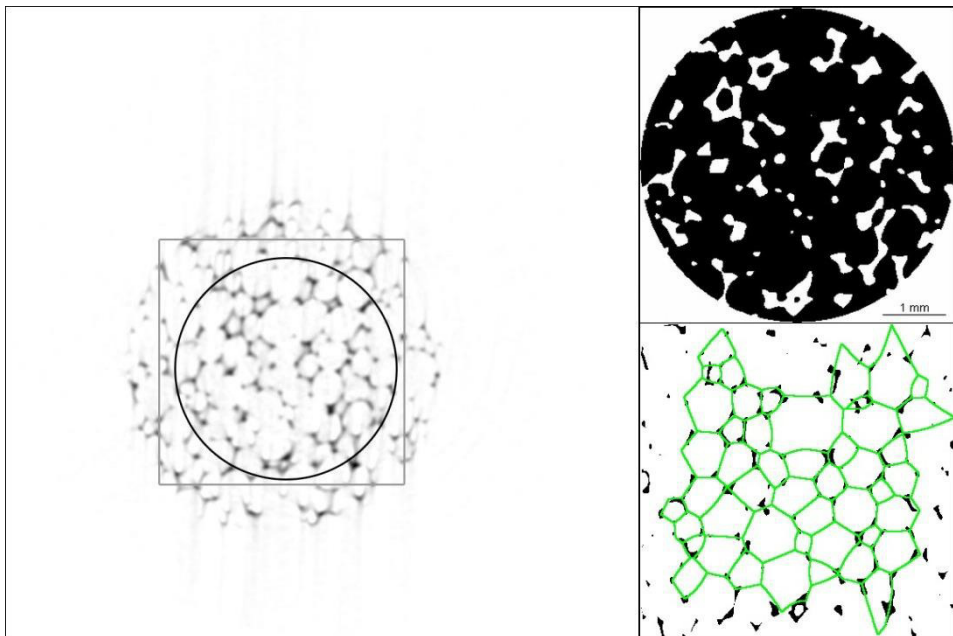


Fig. 79: Left: original FFOV of reconstructed single slice image (CMHR6052) with the highlighted ROIs – circular used for CT, square used for VT method; Right up: detail of the CT-ROI applied on the binarized image, magnified 1.1x, the scale bar applies for both ROI details; Right down: VT network placed over the binarized image within VT-ROI.

Tab. 4: Comparison of results from CT and VT + model parameters – Sample CMHR6250.

a) Material characteristics			b) Computer tomography summary		
Sample	ρ [kg/m ³]	Ω_e (40%) [kPa]	P_0 [%]	$St.Sp$ [mm]	EV_{CT} [mm ³]
CMHR6052	60	5.2	88.275	0.615	0.122
c) Voronoi tessellation/model estimation summary					
μ [mm]	σ [mm]	Δ^2 [-]	EV_1 [mm ³]	EV_2 [mm ³]	EV_3 [mm ³]
0.341	0.080	233227	0.166	0.194	0.257

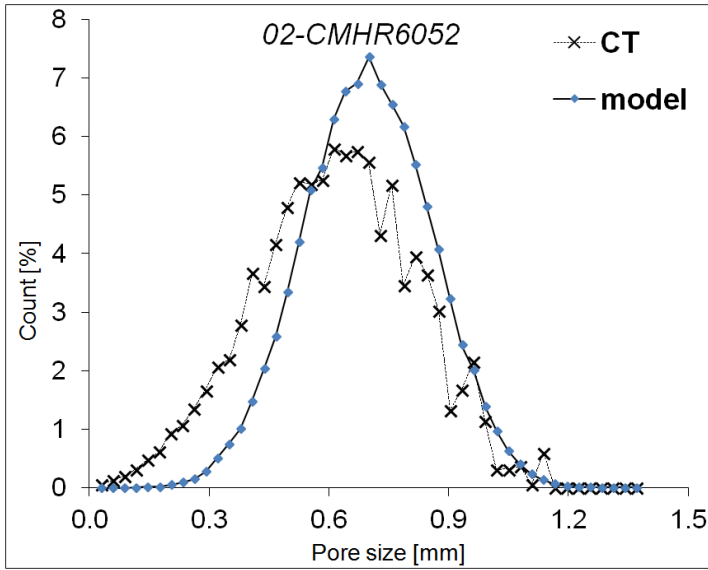


Fig. 80: Comparison of measured (CT) and estimated (model) pore size distributions – CMHR6052.

8.1.3 Sample PANTERA100

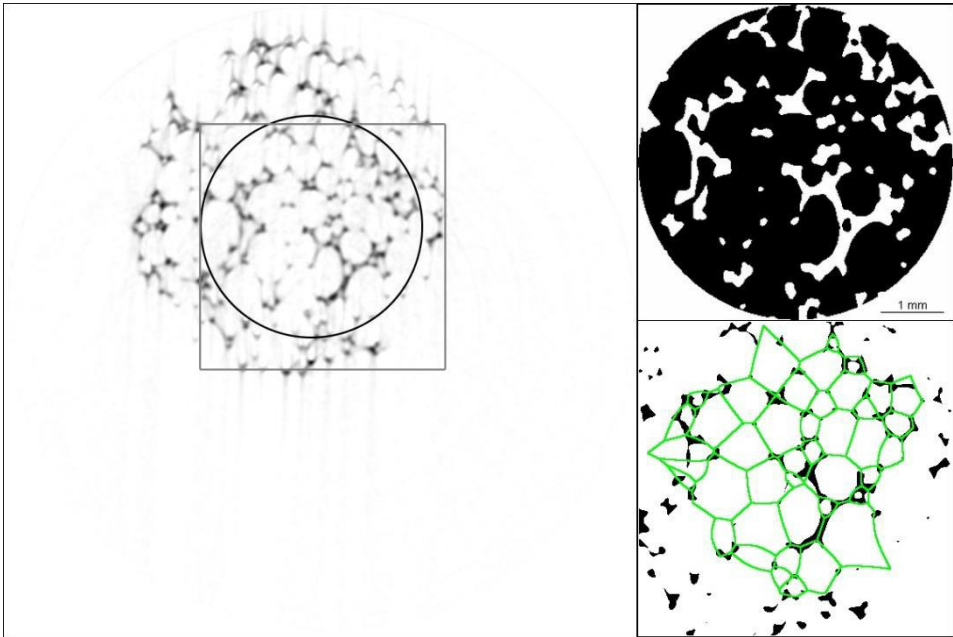


Fig. 81: Left: original FFOV of reconstructed single slice image (PANTERA100) with the highlighted ROIs – circular used for CT, square used for VT method; Right up: detail of the CT-ROI applied on the binarized image, magnified 1.1x, the scale bar applies for both ROI details; Right down: VT network placed over the binarized image within VT-ROI.

Tab. 5: Comparison of results from CT and VT + model parameters – Sample PANTERA100.

a) Material characteristics			b) Computer tomography summary		
Sample	ρ [kg/m ³]	Ω_o (40%) [kPa]	P_o [%]	$St.Sp$ [mm]	EV_{CT} [mm ³]
PANTERA100	50	2.8	82.323	0.690	0.172
c) Voronoi tessellation/model estimation summary					
μ [mm]	σ [mm]	Δ^2 [-]	EV_1 [mm ³]	EV_2 [mm ³]	EV_3 [mm ³]
0.205	0.132	361237	0.036	0.081	0.223

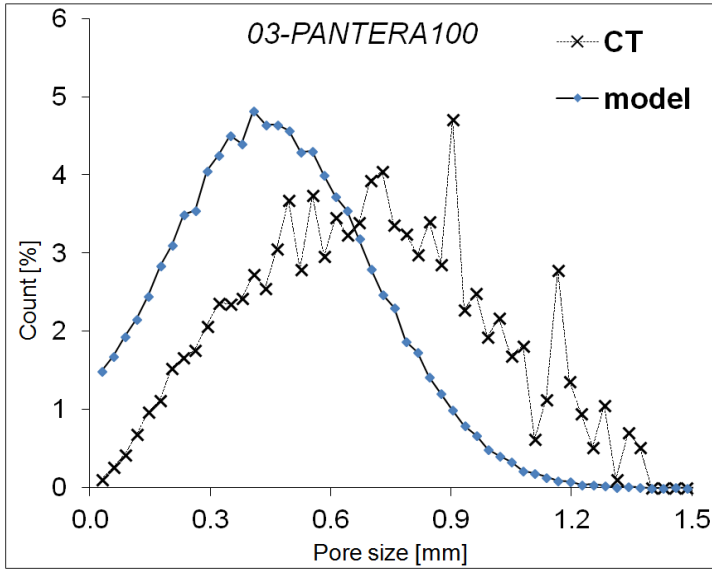


Fig. 82: Comparison of measured (CT) and estimated (model) pore size distributions – PANTERA100.

8.1.4 Sample 4070

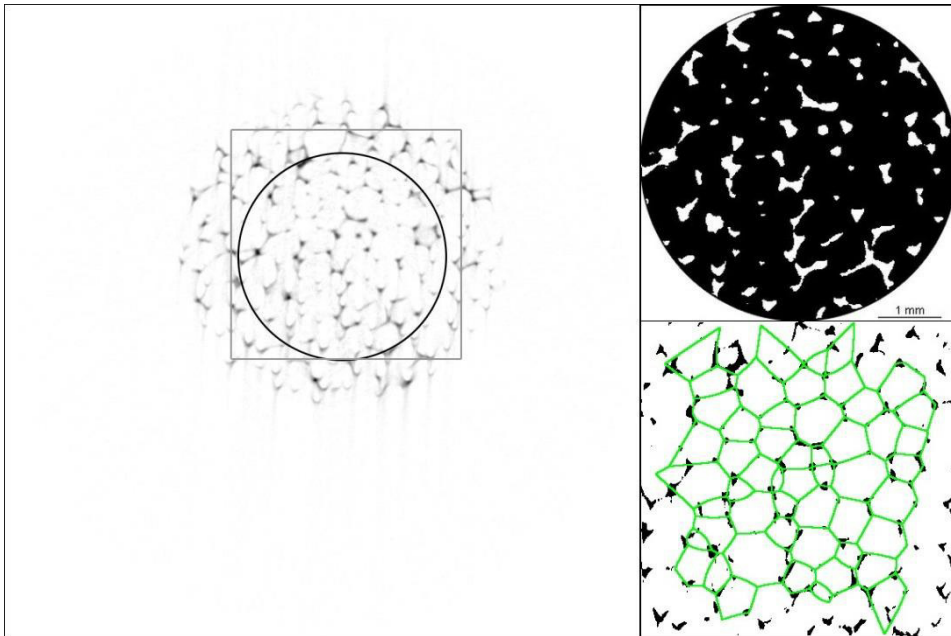


Fig. 83: Left: original FFOV of reconstructed single slice image (4070) with the highlighted ROIs – circular used for CT, square used for VT method; Right up: detail of the CT-ROI applied on the binarized image, magnified 1.1x, the scale bar applies for both ROI details; Right down: VT network placed over the binarized image within VT-ROI.

Tab. 6: Comparison of results from CT and VT + model parameters – Sample 4070.

a) Material characteristics			b) Computer tomography summary		
Sample	ρ [kg/m ³]	Ω_e (40%) [kPa]	P_o [%]	$St.Sp$ [mm]	EV_{CT} [mm ³]
4070	40	7.0	94.950	0.809	0.277
c) Voronoi tessellation/model estimation summary					
μ [mm]	σ [mm]	Δ^2 [-]	EV_1 [mm ³]	EV_2 [mm ³]	EV_3 [mm ³]
0.384	0.040	80049	0.236	0.243	0.280

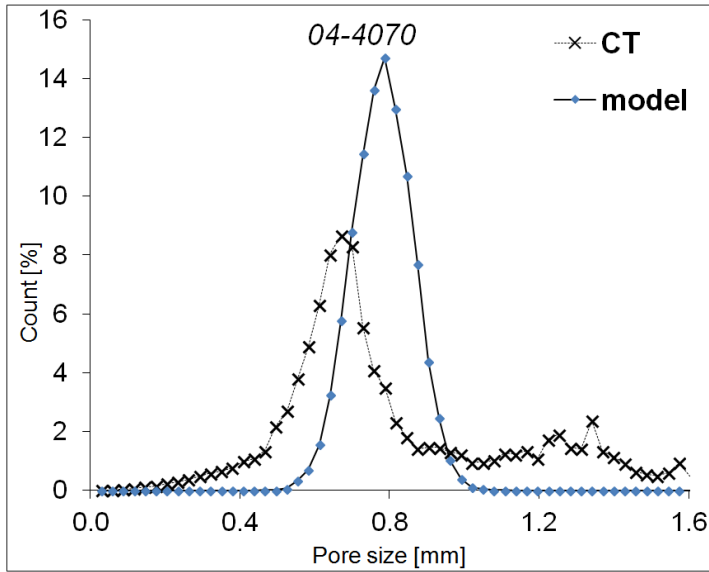


Fig. 84: Comparison of measured (CT) and estimated (model) pore size distributions – 4070.

8.1.5 Sample HR5050

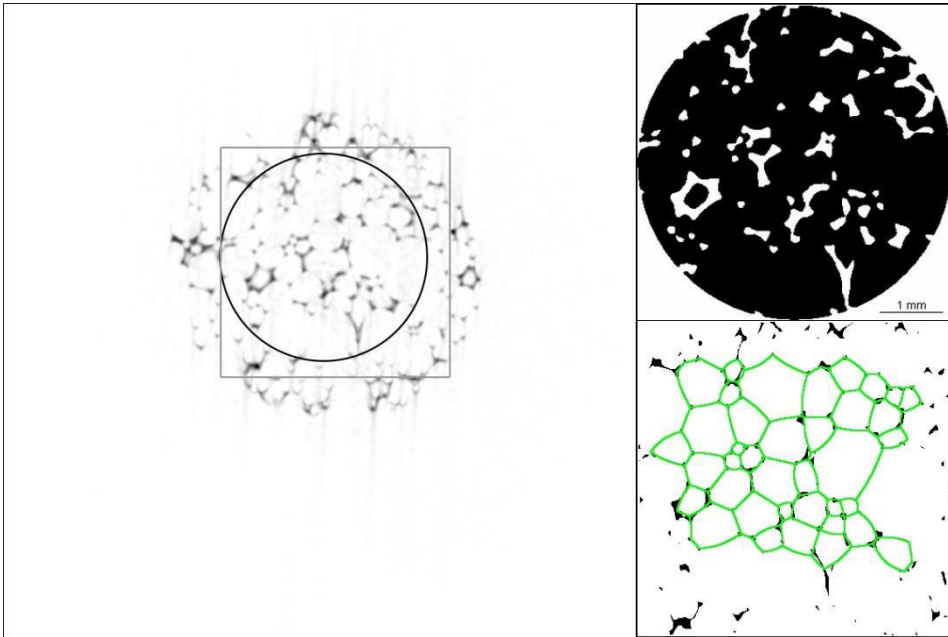


Fig. 85: Left: original FFOV of reconstructed single slice image (HR5050) with the highlighted ROIs – circular used for CT, square used for VT method; Right up: detail of the CT-ROI applied on the binarized image, magnified 1.1x, the scale bar applies for both ROI details; Right down: VT network placed over the binarized image within VT-ROI.

Tab. 7: Comparison of results from CT and VT + model parameters – Sample HR5050.

a) Material characteristics			b) Computer tomography summary		
Sample	ρ [kg/m ³]	Ω_c (40%) [kPa]	P_o [%]	$St.Sp$ [mm]	EV_{CT} [mm ³]
HR5050	50	5.0	88.980	0.762	0.232
c) Voronoi tessellation/model estimation summary					
μ [mm]	σ [mm]	Δ^2 [-]	EV_1 [mm ³]	EV_2 [mm ³]	EV_3 [mm ³]
0.328	0.124	75650	0.147	0.213	0.328

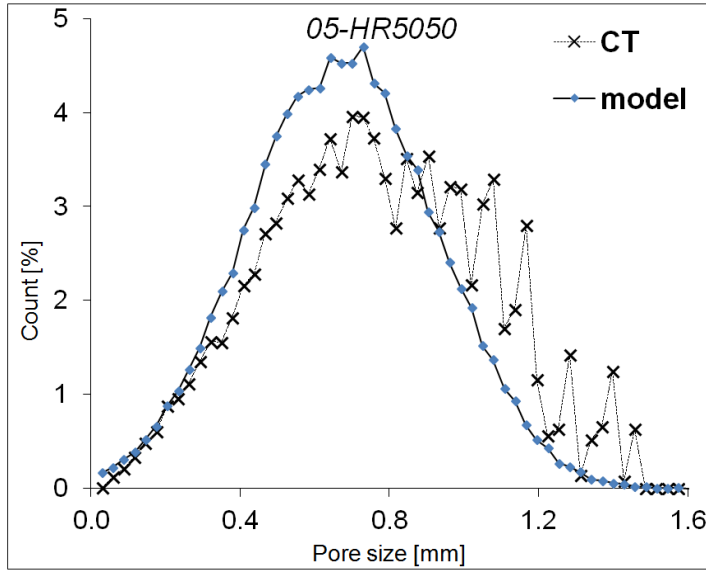


Fig. 86: Comparison of measured (CT) and estimated (model) pore size distributions – HR5050.

8.1.6 Sample 3050

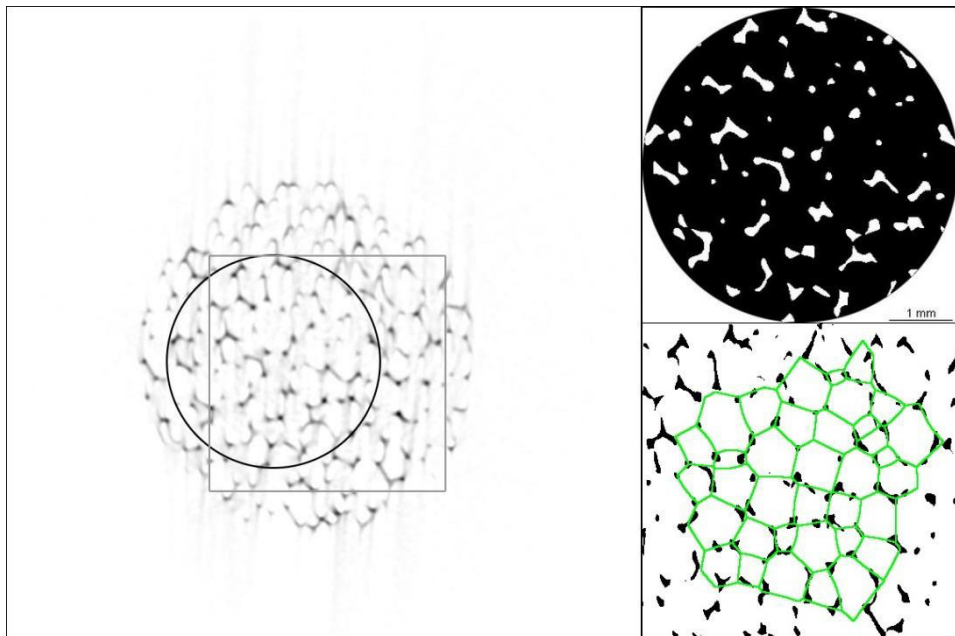


Fig. 87: Left: original FFOV of reconstructed single slice image (3050) with the highlighted ROIs – circular used for CT, square used for VT method; Right up: detail of the CT-ROI applied on the binarized image, magnified 1.1x, the scale bar applies for both ROI details; Right down: VT network placed over the binarized image within VT-ROI.

Tab. 8: Comparison of results from CT and VT + model parameters – Sample 3050.

a) Material characteristics			b) Computer tomography summary		
Sample	ρ [kg/m ³]	Ω_e (40%) [kPa]	P_o [%]	$St.Sp$ [mm]	EV_{CT} [mm ³]
3050	30	5.0	92.090	0.637	0.135
c) Voronoi tessellation/model estimation summary					
μ [mm]	σ [mm]	Δ^2 [-]	EV_1 [mm ³]	EV_2 [mm ³]	EV_3 [mm ³]
0.417	0.044	426326	0.303	0.314	0.412

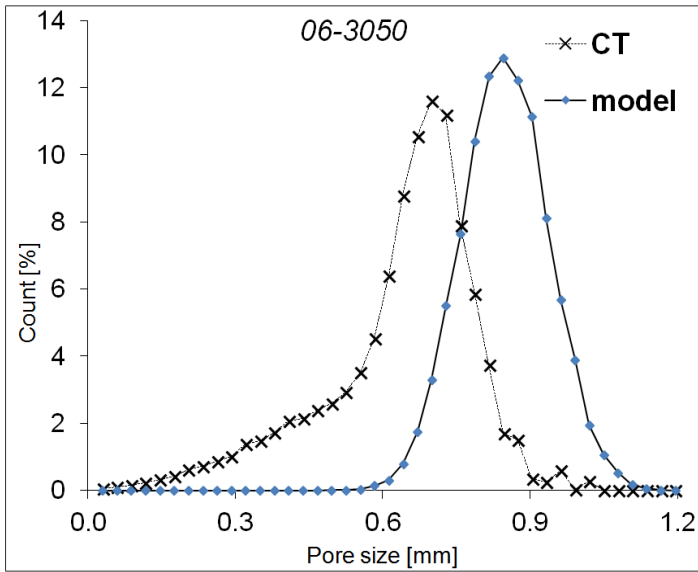


Fig. 88: Comparison of measured (CT) and estimated (model) pore size distributions – 3050.

8.1.7 Sample 2545

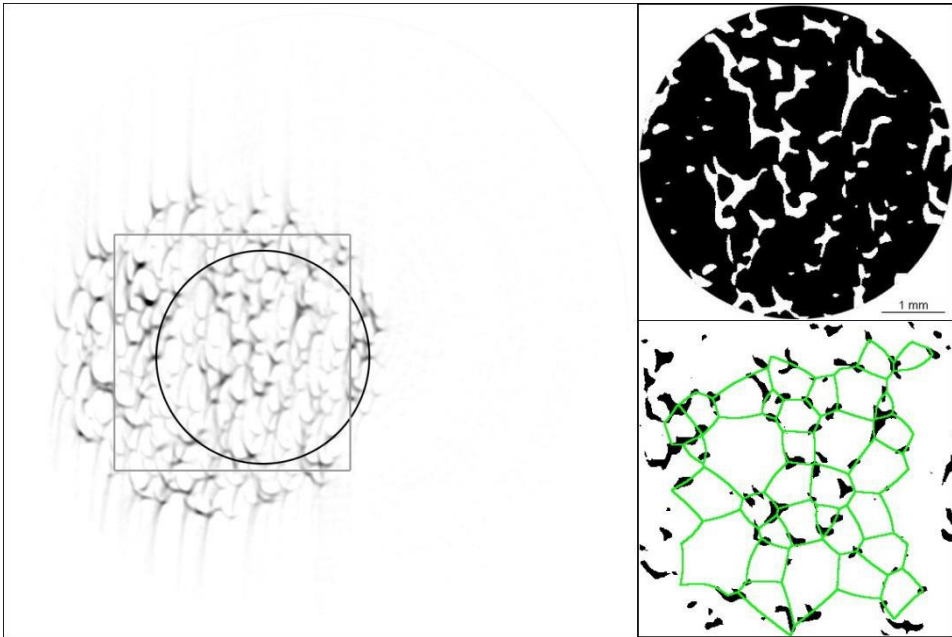


Fig. 89: Left: original FFOV of reconstructed single slice image (2545) with the highlighted ROIs – circular used for CT, square used for VT method; Right up: detail of the CT-ROI applied on the binarized image, magnified 1.1x, the scale bar applies for both ROI details; Right down: VT network placed over the binarized image within VT-ROI.

Tab. 9: Comparison of results from CT and VT + model parameters – Sample 2545.

a) Material characteristics			b) Computer tomography summary		
Sample	ρ [kg/m ³]	Ω_e (40%) [kPa]	Po [%]	$St.Sp$ [mm]	EV_{CT} [mm ³]
2545	25	4.5	85.111	0.435	0.043
c) Voronoi tessellation/model estimation summary					
μ [mm]	σ [mm]	Δ^2 [-]	EV_1 [mm ³]	EV_2 [mm ³]	EV_3 [mm ³]
0.410	0.090	142008	0.288	0.331	0.455

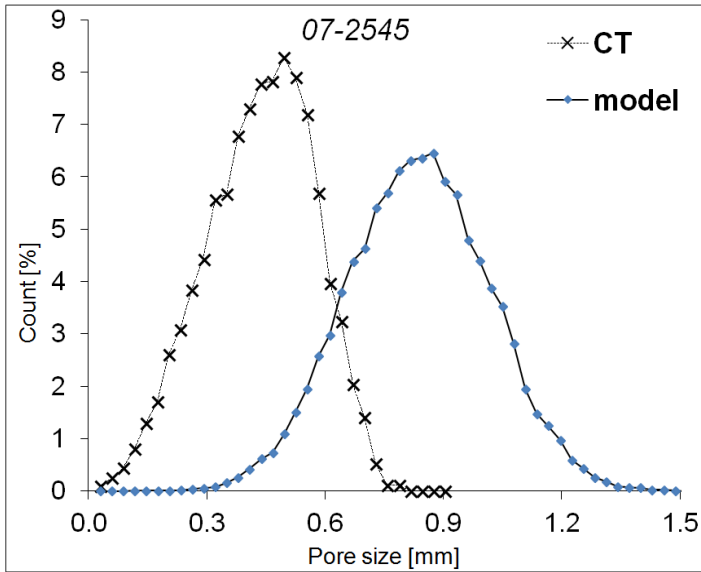


Fig. 90: Comparison of measured (CT) and estimated (model) pore size distributions – 2545.

8.1.8 Sample 2340

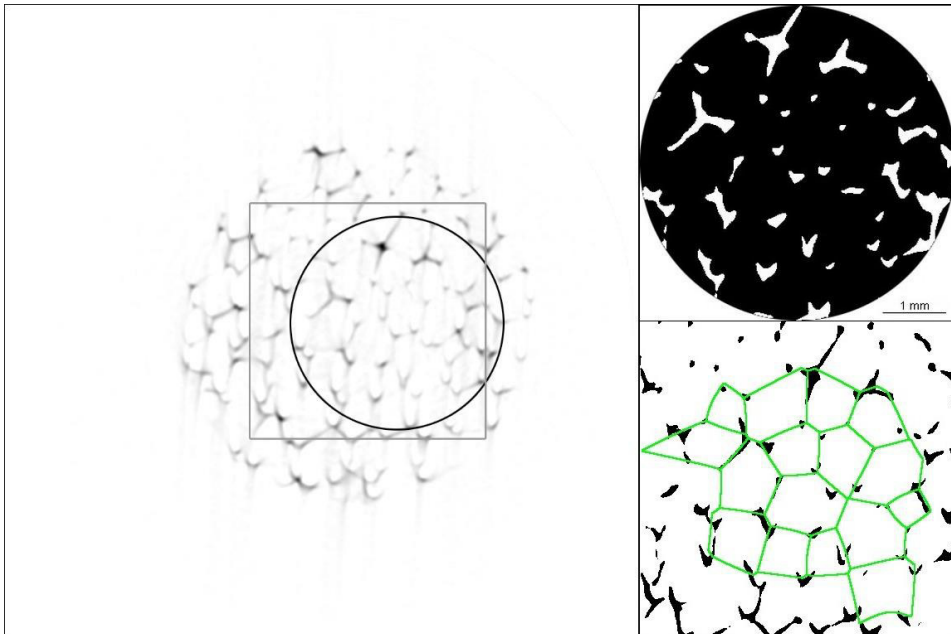


Fig. 91: Left: original FFOV of reconstructed single slice image (2340) with the highlighted ROIs – circular used for CT, square used for VT method; Right up: detail of the CT-ROI applied on the binarized image, magnified 1.1x, the scale bar applies for both ROI details; Right down: VT network placed over the binarized image within VT-ROI.

Tab. 10: Comparison of results from CT and VT + model parameters – Sample 2340.

a) Material characteristics			b) Computer tomography summary		
Sample	ρ [kg/m ³]	Ω_o (40%) [kPa]	P_o [%]	$St.Sp$ [mm]	EV_{CT} [mm ³]
2340	23	4.0	91.026	0.715	0.191
c) Voronoi tessellation/model estimation summary					
μ [mm]	σ [mm]	Δ^2 [-]	EV_1 [mm ³]	EV_2 [mm ³]	EV_3 [mm ³]
0.576	0.049	87570	0.801	0.820	0.980

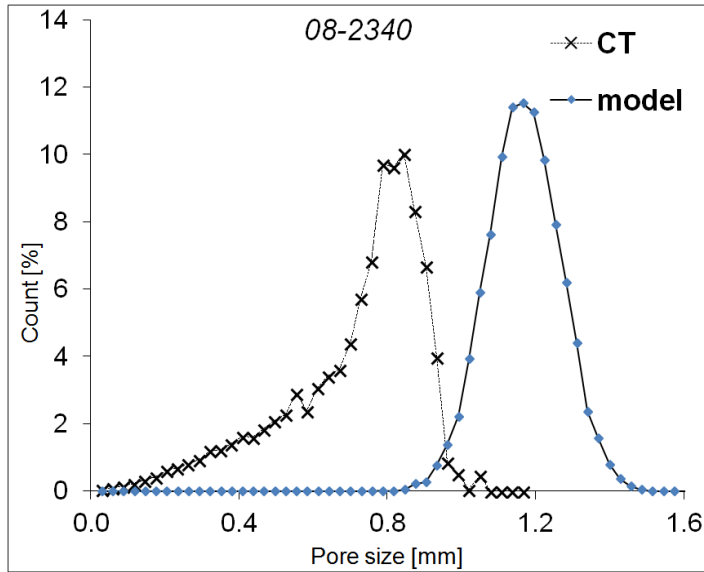


Fig. 92: Comparison of measured (CT) and estimated (model) pore size distributions – 2340.

8.1.9 Sample 2015

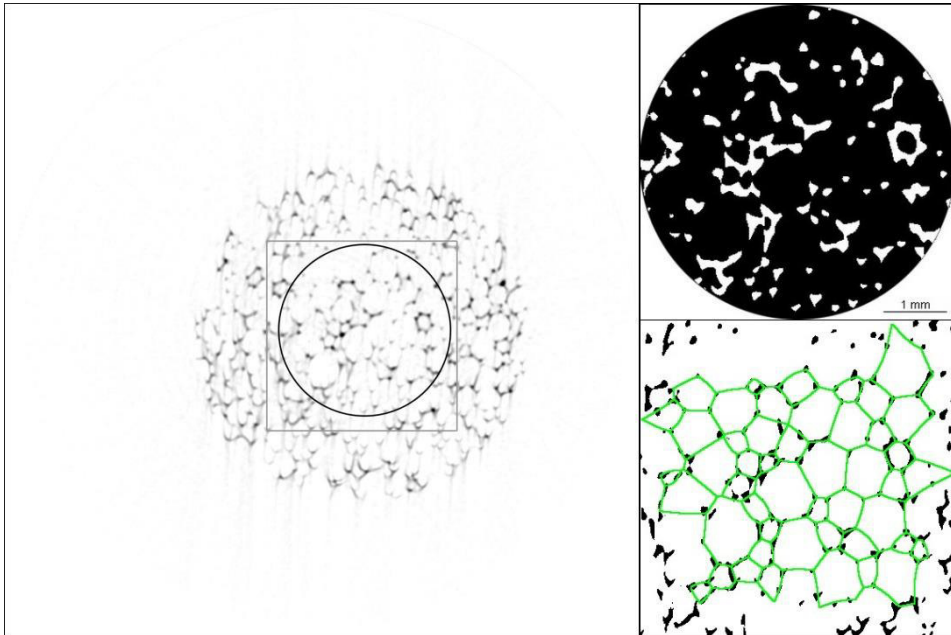


Fig. 93: Left: original FFOV of reconstructed single slice image (2015) with the highlighted ROIs – circular used for CT, square used for VT method; Right up: detail of the CT-ROI applied on the binarized image, magnified 1.1x, the scale bar applies for both ROI details; Right down: VT network placed over the binarized image within VT-ROI.

Tab. 11: Comparison of results from CT and VT + model parameters – Sample 2015.

a) Material characteristics			b) Computer tomography summary		
Sample	ρ [kg/m ³]	Ω_o (40%) [kPa]	P_o [%]	$St.Sp$ [mm]	EV_{CT} [mm ³]
2015	20	1.5	86.341	0.584	0.104
c) Voronoi tessellation/model estimation summary					
μ [mm]	σ [mm]	Δ^2 [-]	EV_1 [mm ³]	EV_2 [mm ³]	EV_3 [mm ³]
0.329	0.084	258644	0.150	0.180	0.243

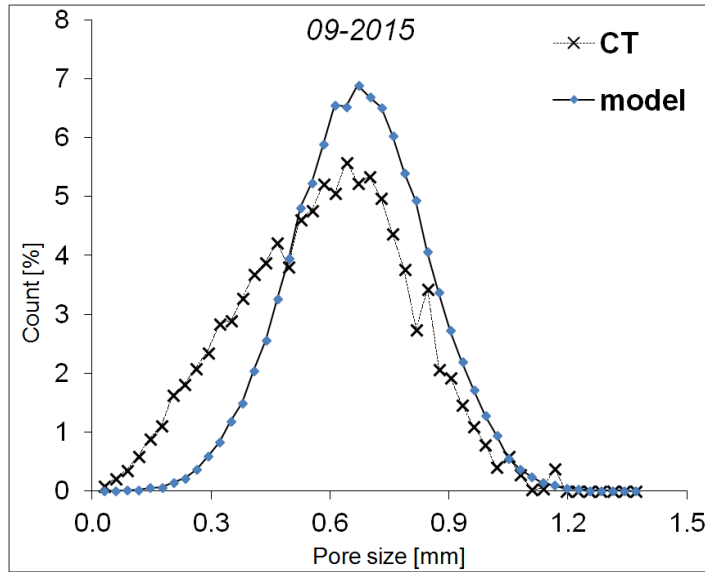


Fig. 94: Comparison of measured (CT) and estimated (model) pore size distributions – 2015.

8.1.10 Sample 3545

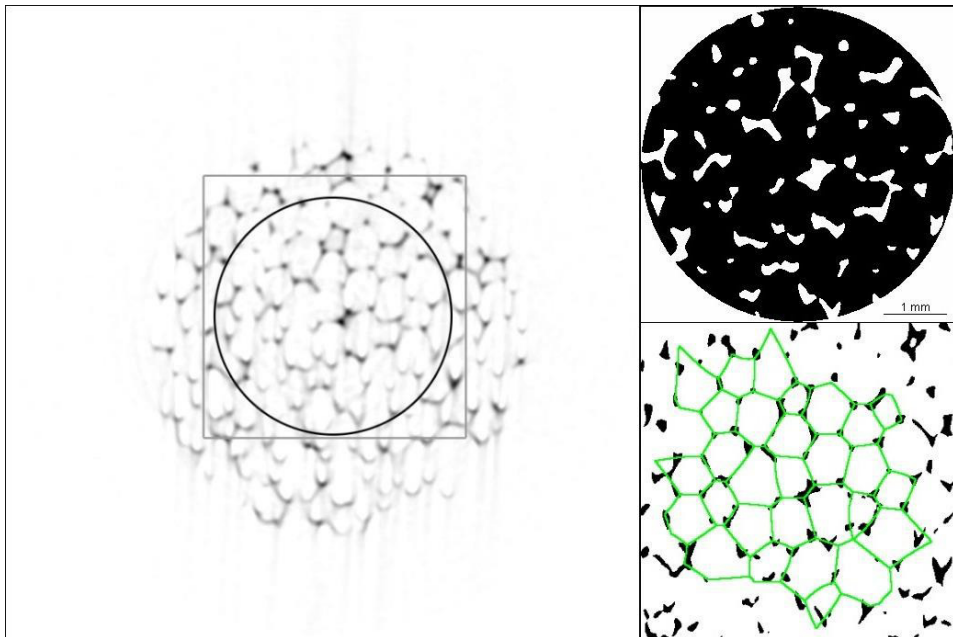


Fig. 95: Left: original FFOV of reconstructed single slice image (3545) with the highlighted ROIs – circular used for CT, square used for VT method; Right up: detail of the CT-ROI applied on the binarized image, magnified 1.1x, the scale bar applies for both ROI details; Right down: VT network placed over the binarized image within VT-ROI.

Tab. 12: Comparison of results from CT and VT + model parameters – Sample 3545.

a) Material characteristics			b) Computer tomography summary		
Sample	ρ [kg/m ³]	Ω_c (40%) [kPa]	P_o [%]	$St.Sp$ [mm]	EV_{CT} [mm ³]
3545	35	4.5	88.486	0.603	0.115
c) Voronoi tessellation/model estimation summary					
μ [mm]	σ [mm]	Δ^2 [-]	EV_1 [mm ³]	EV_2 [mm ³]	EV_3 [mm ³]
0.441	0.048	254750	0.360	0.373	0.447

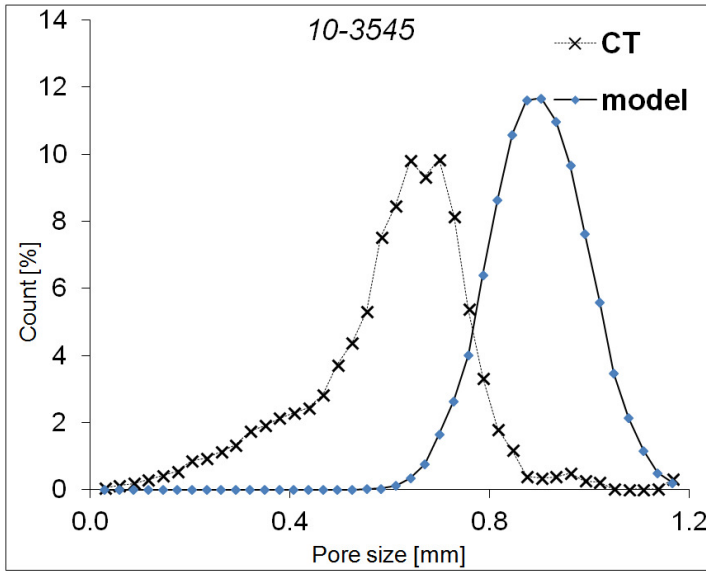


Fig. 96: Comparison of measured (CT) and estimated (model) pore size distributions – 3545.

The result from CT shows that the porosity of the observed foams ranges from 82.32 % (sample PANTERA 100) to 94.95 % (sample 4070). The CT analysis also revealed that the mean linear size of the pores, which is expressed by means of $St.Sp$ parameter is very narrowly scattered: eight values ranging within the interval 0.584-0.773 mm and moreover these values are not too remote from the extremes: minimum $St.Sp$ 0.435 mm of the sample 2545 to 0.809 mm, relating to the sample 4070. This fact proportionally corresponds also with the mean volumes EV_{CT} .

The graphical comparisons of model-based distributions with the experimentally acquired distributions show relatively good compliance of both methods. This conclusion can be stated inasmuch as the mean values of both distributions were found to be of the same order. The only exception is the sample 2545 (Fig. 90), which exhibits the largest shift of the distribution curves. This anomaly is very probably caused by the blur of the CT dataset (Fig. 89).

The values EV_1 and EV_2 slightly vary from each other, as the computational method is different, but still can be considered as similar. However, the EV_3 values based on ASTM are the greatest in all cases. The comparison of all these three mean volumes illustrates the bar chart (Fig. 97). As one can see, the greatest difference between the EV_{CT} value and the other mean volumes show the sample 2545 again, confirming the discrepancy between the CT result and model estimation caused by the distorted images from CT. Therefore, this sample was excluded from the further discussions and comments.

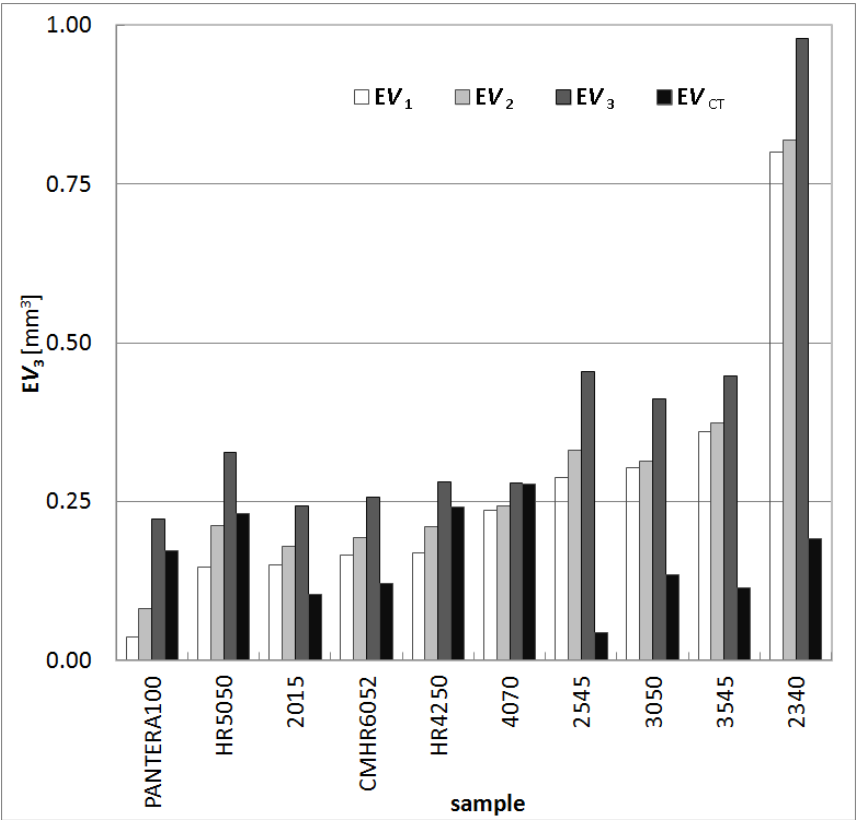


Fig. 97: Mean volumes of the individual samples ordered in ascending manner according EV_1 .

The graphical confrontation of the model-based EV_1 and EV_2 values with the ASTM E112 standard-based EV_3 is shown in the figures (Fig. 98 and Fig. 99):

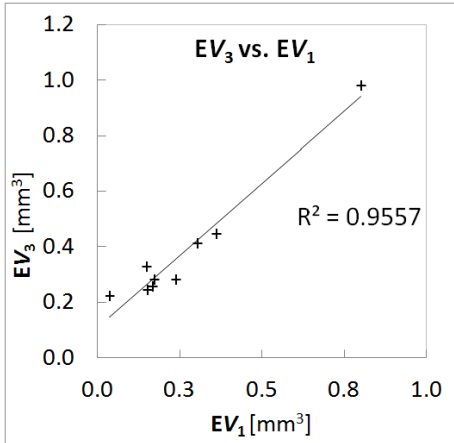


Fig. 98: Correlation between the EV_3 and EV_1 .

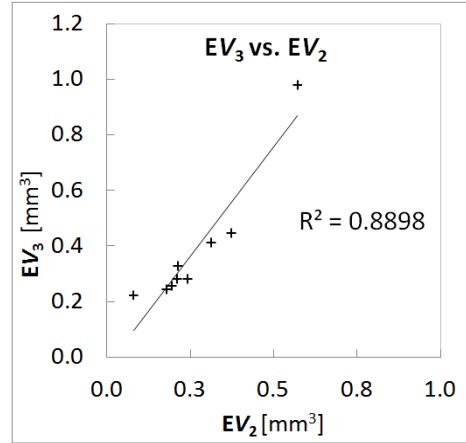


Fig. 99: Correlation between the EV_3 and EV_2 .

The graphs (Fig. 98 and Fig. 99) prove that the proposed method of estimating the mean volume based on the modelling the structure, as it has been described above, provides meaningful results, as these are comparable with the standardized method. Moreover, this novel method brings one substantial benefit because beside the mean volume estimation it is also capable to estimate the size distribution.

8.1.11 Acoustic properties of the foams

In order to put into the context the structural characteristics and the physical properties of the materials, the measurements of acoustic absorption coefficient α [-] and noise reduction coefficient (NRC) were carried out. These two values are commonly used to characterize the acoustic properties of materials.

The acoustic absorption coefficient α is defined as the incident-to-pass acoustic energy ratio and it is measured in a range of frequencies. Based on the results of α the NRC is counted as the arithmetical average of α values at 250, 500, 1000 and 2000 Hz, according to ASTM C423 specification [152].

The analysis was performed in two-microphone impedance tubes, provided by Brüel & Kjaer, type 4206. The acoustic absorption coefficient was measured through the range of frequencies between 0-4000 Hz on two cylindrical samples of the diameters 100 mm enabling the measurement in the interval 16 Hz – 1.6 kHz and 30 mm for the frequency range between 50 Hz and 4 kHz. The cylindrical samples had constant thickness of 40 mm.

As it is evident from Fig. 100, the curves are similar to each other with only small variance among them. This fact can be attributed to the previously mentioned narrow scatter of mean pore sizes.

However, it can be stated, that the samples HR 4250, 4070 and 3545, exhibit the best acoustic absorption properties from the entire set of the samples at lower frequencies (band up to 1 kHz) as these three individual curves show considerable higher acoustic absorption at this range. Moreover, the acoustic absorption behaviour of the sample HR4250 differs also between the frequencies 1 kHz and 2 kHz when α reaches the maximum of 0.97 (at 1.76 kHz) which was the highest

value measured in global. The response in the remaining part of the frequency band can be evaluated as similar to other materials, despite the decline of α to ca. 0.7 (slightly above 3 kHz).

It is also clear that the overall acoustic response of samples 4070 and 3545 differ from the behaviour of the other samples, as α reaches two maxima and two local minima along the measured frequency range in both cases. While the first minimum of α (approximately $\alpha = 0.72$ at 0.8 kHz for the sample 3545 and $\alpha = 0.68$ at 1.2 kHz for the sample 4070) exceeds the α values of all remaining samples, the second pair of minima (ca. $\alpha = 0.74$ for 3545 and $\alpha = 0.62$ for 4070, both at about 2.1 kHz) lies considerably below the α of the other samples at this frequency.

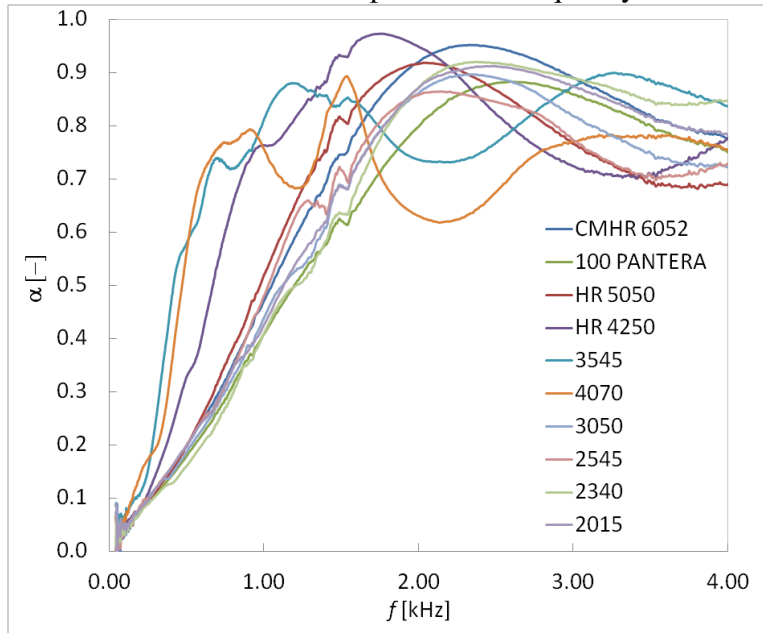


Fig. 100: The mutual dependence of acoustic absorption coefficient and frequency for all measured materials.

The results of the acoustic analysis are shown in Tab. 13, that summarizes the α coefficient values at characteristic frequencies, as well as the NRC coefficient and the overview of all α individual maxima measured for all samples.

Tab. 13: Overview of acoustic absorption coefficients at characteristic frequencies, NRC coefficient and maximum acoustic damping for all investigated materials.

sample	acoustic absorption coefficient α [-] at given frequency [Hz]							maximum acoustic damping	
	125 Hz	250 Hz	500 Hz	1000 Hz	2000 Hz	4000 Hz	NRC	frequency	α
	[-]	[-]	[-]	[-]	[-]	[-]	[-]	[Hz]	[-]
HR4250	0.06	0.11	0.33	0.76	0.95	0.78	0.54	1760	0.97
CMHR6052	0.04	0.09	0.20	0.47	0.92	0.77	0.42	2376	0.95
PANTERA100	0.05	0.09	0.18	0.41	0.80	0.75	0.37	2600	0.88
4070	0.08	0.17	0.57	0.76	0.63	0.76	0.53	1536	0.89
HR5050	0.05	0.09	0.20	0.52	0.92	0.69	0.43	2040	0.92
3050	0.05	0.10	0.19	0.44	0.86	0.72	0.40	2368	0.90
2545	0.05	0.10	0.20	0.48	0.86	0.73	0.41	2160	0.86
2340	0.04	0.09	0.16	0.41	0.87	0.85	0.38	2373	0.92
2015	0.05	0.10	0.20	0.43	0.87	0.78	0.40	2488	0.91
3545	0.08	0.15	0.58	0.81	0.74	0.84	0.57	3264	0.90

Due to the narrow scatter of mean pore size, which was mentioned above the only evident relationship between the structure and acoustic properties is the mutual dependence of maximum damping frequency and mean pore size, as shown in Fig. 101. The graph (Fig. 101) reveals a downward trend of the maximum damping frequency (the frequency that corresponds with the maximum α for the given material) with increasing mean pore size EV . These results points out to the fact, that the materials with greater EV are more suitable for lower frequencies, when used as the acoustic dampers, while the foams with smaller EV value are more advisable for damping of higher frequencies.

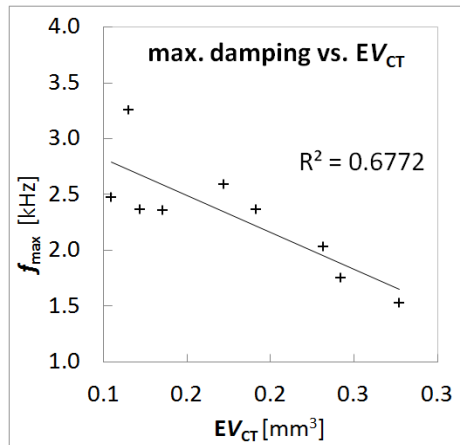


Fig. 101: Maximum damping frequency dependence on mean pore size.

8.2 Other possibilities of Voronoi tessellation approach

Direct analyzing the internal structure of the materials by means of CT is frequently a difficult issue to solve, particularly in cases, when the nature of the material disallows any special shaping (eg. due to its mechanical properties), is too

sensitive to X-ray exposition or last but not least absorbs vast of the radiation, leaving the detector underexposed. Thus, in such cases any other appropriate technique needs to be employed. Amongst the suitable solutions it is possible to place the method of approximating the structure of either planar cut or a surface by means of Voronoi tessellation. The following paragraphs show the examples when this approach can serve as an applicable alternative instead of CT.

8.2.1 Pore size estimation in pastry

In the area of food industry the researchers are interested in studying the structure of aerated food products. The typical representing of this group can be pastry [153]. In this case the complete structural analysis via CT would be unnecessarily detailed, as the evaluation criterion is only the texture (2D appearance) of the pastry and the comparison of results for various samples is often sufficient. The image processing, analysis and Voronoi tessellation approximation of a bread slice resulting into the bread texture reconstruction is shown in Fig. 102 and Fig. 103. The samples of bread for the analysis were prepared at the Department of Food Technology of Faculty of Technology at Tomas Bata University in Zlín.

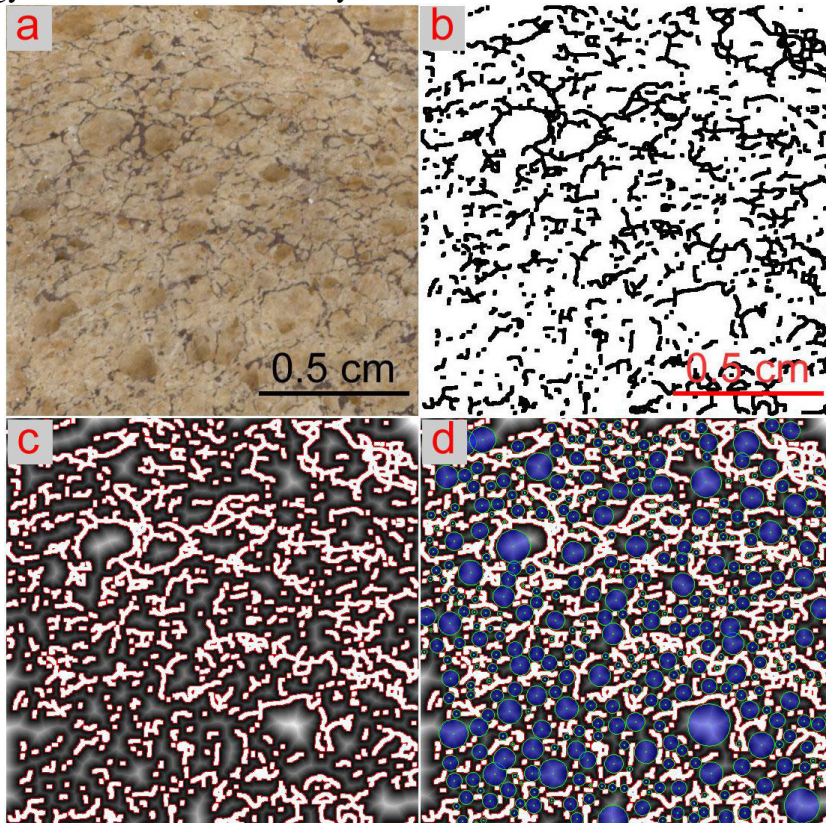


Fig. 102: a) original surface scan of the dried bread slice, b) binarized structure, c) EDM applied to the binarized image, d) inscribed circles fitting on the basis of EDM result.

The bread was scanned using conventional PC scanner HP ScanJet 2200c at resolution of 1000 dpi. The surfaces of dried bread slices were brushed by very fine sandpaper with the intention to flat them and obtain sharp images. Consequently, still prior to scanning itself, the brushed surfaces were covered with in thin layer of black stamping ink, in order to enhance boundaries contrast (Fig. 102a). The image analysis pre-processing was performed in ImageJ. The key step of the pre-processing – image binarization consisted out of several steps, including edge detection, skeletonization, despeckling to remove image noise and dilation. The resulting image (Fig. 102b) was further subjected to the image analysis (Fig. 102c and Fig. 102d), as described above and the final Voronoi tessellation of the structure was computed. The result, showing also the comparison with the original image, is illustrated in Fig. 103:

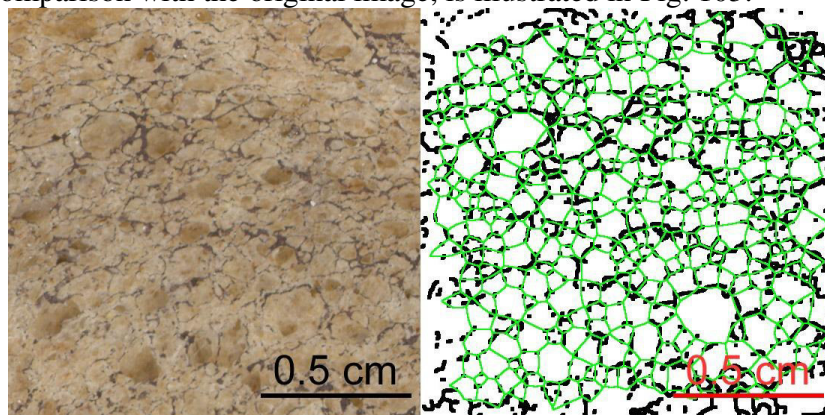


Fig. 103: Bread scan (left) vs. final Voronoi tessellation placed over the binarized image.

It can be concluded that this method provides basic planimetric data about the studied material, describing the texture of bubble structure on the cut through the material. Small disadvantage of the method is considering thin boundaries between the pores by Voronoi tessellation, leading to slight difference (overestimation) of the pores areas, as the real boundary thickness may vary from thin to relatively thick cell walls.

8.2.2 Pore size estimation in resin/metal sintered composites

From the area of materials engineering it is possible to mention the case of grain size estimation in iron-phenol formaldehyde resin soft magnetic composites [154], [155]. These materials belong to the group of materials with very limited feasibility of being scanned with the CT due to great difference between the X-ray absorption of the iron and resin. Thus, an over- or under-exposition of the materials occurs, hiding the important structural information, mainly the materials interfaces. The samples of the composites were prepared using conventional powder metallurgy at Institute of Materials Research of Slovak Academy of Sciences in Košice.

Extracting the structural information from the image was possible by image analysis of the optical micrographs (Fig. 104a), where the grey areas represent the polymer matrix, while the iron is black. The image analysis in procedure was similar to the previous example: starting with the edge detection prior to the

binarization and following despeckling and dilating the image (Fig. 104b) in ImageJ. The computation of EDM (Fig. 104c) and approximation by inscribed circles (Fig. 104d) served as the finding the generators of Voronoi tessellation computation shown in Fig. 105, right.

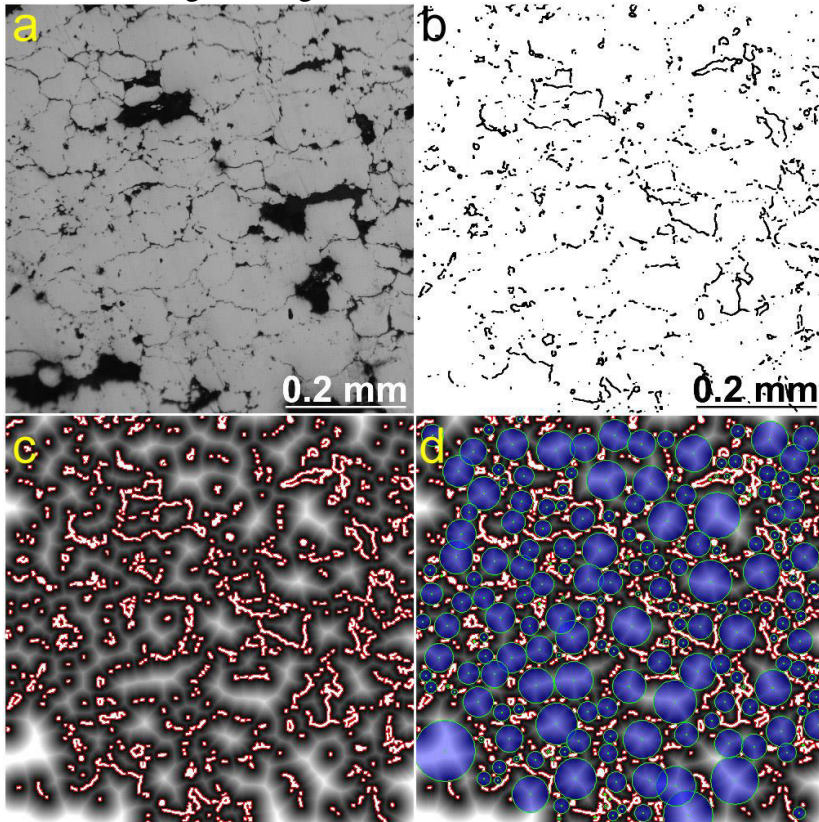


Fig. 104: a) original micrograph of the resin-metal composite, b) binarized structure, c) EDM applied to the binarized image, d) inscribed circles fitting on the basis of EDM result.

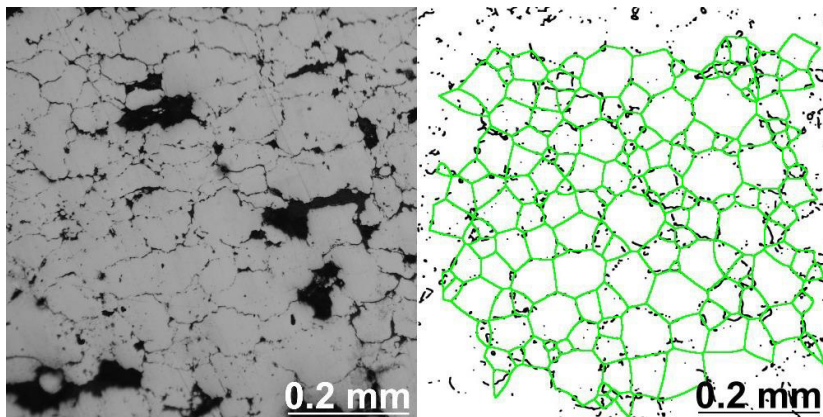


Fig. 105: Original micrograph of the resin-metal composite (left) vs. final Voronoi tessellation placed over the binarized image.

As can be seen in Fig. 105, the Voronoi tessellation approximation fits the structure well, however, due to the material's nature, it is impossible to estimate the structure parameters of the individual phases separately. That is caused by discontinuity of the iron phase which contradicts with the basic presumption of the Voronoi tessellation technique – continuity and interconnectivity of the cells. However the technique is still capable to estimate the overall (resin+metal) cells size distribution.

8.2.3 Grain size estimation in metal scratch patterns

Last but not least, it is necessary to mention the possibility of utilization of this method for estimating the structural parameters of grainy structure in metals.

As can be seen in (Fig. 106a) a common scratch pattern of an alluminum alloy prepared in a conventional manner by grinding, etching and polishing the surface reveals the grain boundaries, which are consequently observable in reflected light by optical microscope.

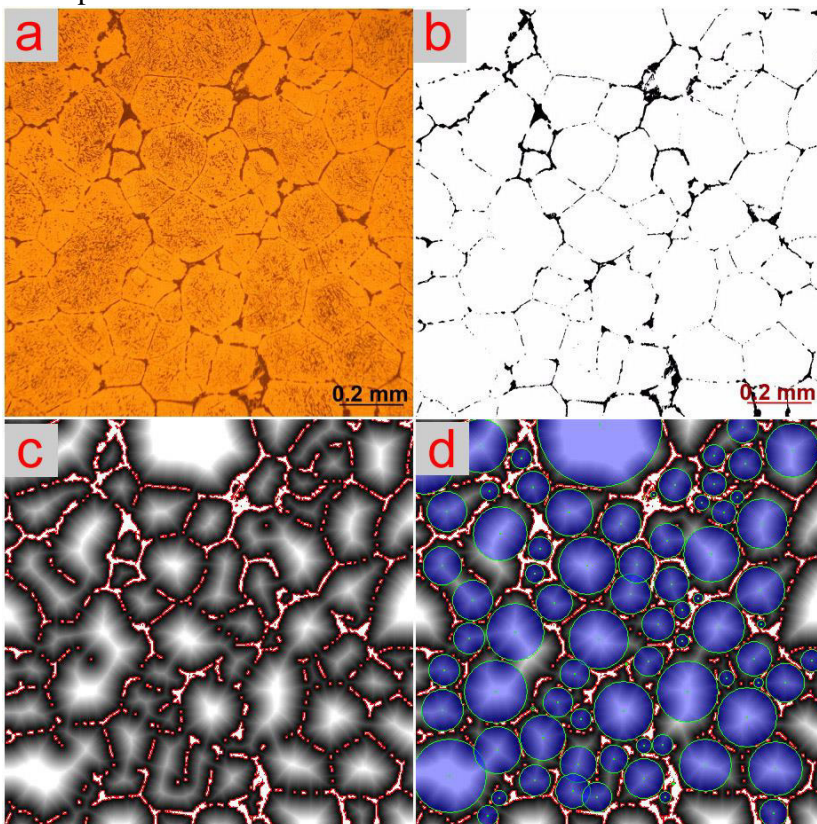


Fig. 106: a) original micrograph of the scratch pattern, b) binarized structure, c) EDM applied to the binarized image, d) inscribed circles fitting on the basis of EDM result.

The further image processing steps are principally completely the same as in the previous cases. However, as the original micrograph (Fig. 106a) exhibits a relatively high noise in the middle of some grains (e.g. see northwest quarter of Fig. 106a), the binarization requires more effort. This undesirable image noise was

probably caused by either improper etching or polishing procedure. Beside the usual sequence of the steps including edge detection, despeckling and dilating in ImageJ, some manually-assisted despeckling helping to remove the speckles bigger than 1px and clusters of pixels obviously not belonging to the boundaries was carried out (Fig. 106b). Carefully done binarization procedure provides the basis for the subsequent steps of EDM computation (Fig. 106c) and the inscribed circle fitting (Fig. 106d). The final Voronoi tessellation network (Fig. 107, right) fits the original structure boundaries quite well.

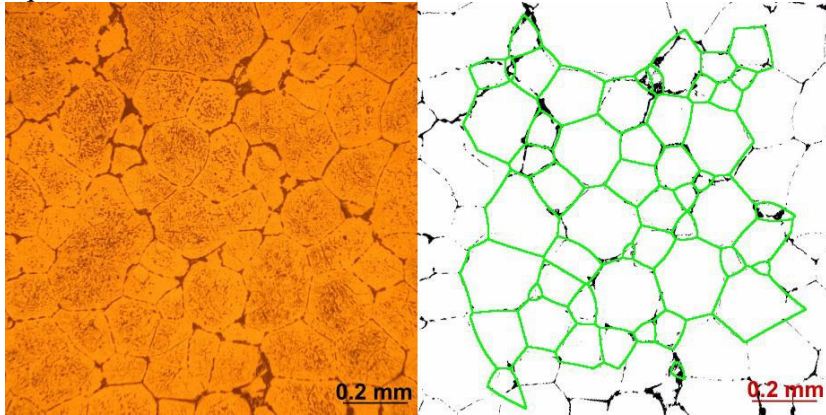


Fig. 107: Original micrograph of the alloy starch pattern (left) vs. final Voronoi tessellation placed over the binarized image.

These three examples shown the versatility of the method from the perspective of its applications. In all cases the graphical result (see the right parts of Fig. 103, Fig. 105 and Fig. 107) is accompanied by the numerical values of cross sectional areas of the individual cels. Averaging these values leads to finding mean cross sectional area EA for each material. Finally, when applied the computation according Eq. (12), the mean feature volume EV is estimated.

CONTRIBUTION TO SCIENCE

The experimental work of the doctoral studies was primarily focused on designing a novel stereological method for simple and straightforward estimation of structural parameters, especially the mean volume of a feature in generally porous or grainy materials from simple image of either planar cross section through the investigated structure or from the image of the surface. Another goal was to verify the results achieved by these estimations by means of a comparative measuring technique, which would identify the precision of the estimations. As the most convenient method for this purpose was found X-ray computed microtomography, a method, that is widely employed for the structural analysis in area of materials research and is capable to provide exact structural data of the materials.

The proposed method is based on common stereological tools – image analysis, mathematical morphology, Euclidean distance count, Voronoi tessellations and mathematical principles of normal distribution which has been found valid for the size distributions in polymeric foams. The comparison of the results with the data from X-ray computed microtomography has revealed, that despite the results of the estimations are not the same as the tomographic data, both values are of the same order. This finding puts the method on the level tomography. Mean pore volumes determined by means of estimation have shown good correlation with the mean pore volumes computed using the method proposed by ASTM E112 standard. Another important benefit which has to be highlighted is the fact, that the method surpasses the methodology of ASTM E112, since it is capable to provide not only the estimation of the mean volume but also the distribution curve. Additionally, the estimated distribution width correlates with the tomographical distribution, as it has been confirmed by mutual comparing the distributions.

Even though there are many positive points which has been found and proved, there is still some spare space for certain improvements of the current method. Firstly, the construction of the model with more than two parameters, may even better fit the X-ray computed microtomography data. Secondly, the Euclidean distance computation and following Voronoi tessellation construction performed in three-dimensional space instead of the actual two-dimensional computation would be definitely more accurate.

To conclude, the main contribution of the experimental work to science, mainly to the field of stereology, lies in the fact that it has been developed and verified the method that provides a significantly cheaper and principally simpler but reliable alternative to X-ray computed microtomography for needs of determining the mean feature volume and the size distribution. It has been also shown, that this method is relatively versatile and thus can serve for the analysis of both grainy and cellular materials, even in the cases when the X-ray microcomputed tomography cannot be used.

USED SYMBOLS AND ACRONYMS

Symbol	Dimension	Meaning(s)
0D, 1D, 2D, 3D		zero-, one-, two-, three-dimensions / dimensional
A, A	$[m^2]$ / -, -	area / point set, model sphere / cutting plane
A_A	$[m^2/m^2]$	area fraction / intercept area-to-reference-area ratio
ASTM		American Society for Testing and Materials
b		member of singleton B / pixel in EDM / bit
B, B		subset of set Q or singleton, model sphere / byte
BC		before Christ
c		cutting plane
ca.		approximately
CCD		charge coupled device
ccm	$[cm^3]$	cubic centimetres
CIE		Commission Internationale de l'Éclairage - International Commission on Illumination
CLSM		confocal laser scanning microscope / microscopy
CM		reduced flammability foam
CMOS		complementary metal oxide on silicon
CMYK		cyan-magenta-yellow-black colour space
CO_2		carbon dioxide
CT		X-ray computed microtomography
CTAn		CT-Analyser – SW for CT images processing
ČSN		Česká státní norma - Czech State Norm
d		number of dimensions / distance in EDM
DIN		Deutsches Institut für Normung – German Institute for Standardization
dpi		dots per inch or pixels per inch – image resolution
DSLR		digital single lens reflected (camera)
e		Euler's number
E		number of objects which not passes through the disector
e.g.		<i>exempli gratia</i> – for example
EA	$[m^2]$	mean profile area
EDM		Euclidean distance map
Eq.		equation
ER, E_r	$[m]$	mean sphere radius

Symbol	Dimension	Meaning(s)
et al.		<i>et alii</i> – and others
etc.		<i>et cetera</i> - and others
EV	[m ³]	mean volume of an object
FFOV		full field of view
Fig.		figure
f_{\max}	[Hz]	maximum sound absorption frequency
f_r		density of the cross section radii function
F_R		cumulative distribution function
G		ASTM grain size number
h	[m]	height (of a cycloid)
h_p, h_s		Prewitt's operator, Sobel's operator (edge detection)
HR		high resilience foam
i.a., i.e.		<i>inter alia</i> – among others, <i>id est</i> – that is
i, j		ordinal number of the row, ordinal number of the column in EDM
L	[m]	length
L_A	[m/m ²]	length of a linear object (or perimeter) per unit area
L_L	[m/m]	length fraction / intercept length-to-reference-length ratio
ln		<i>logarithmus naturalis</i> - natural logarithm
L_V	[m/m ³]	length density
min, max		minimum, maximum
N	[-]	number
NRC		Noise reduction coefficient
N Recon		reconstruction SW for raw CT images
N_A	[m ⁻²]	(feature) count per unit area
nano-		not exceeding a dimension of 10 ⁻⁹ m
N_i		number of profiles intersecting the test area (method of Jeffries)
N_L	[m ⁻¹]	number per unit length
N_r		total number of profiles (method of Jeffries)
N_V	[m ³]	number of objects per unit volume
N_w		number of profiles inside the test area (method of Jeffries)
$Obj.S, Obj.V$	[m ² , m ³]	object surface, object volume (CT)
OM		optical microscope / microscopy
p, q		total number of rows, total number of columns in EDM
P_A	[m ⁻²]	area point count

Symbol	Dimension	Meaning(s)
PC		personal computer
PDF		probability density function
P_i		original pixel contrast value
P_L	$[m^{-1}]$	points per unit length
P_o	$[\%]$	porosity (CT)
P_p	$[-]$	point fraction
PPP		Poisson point process
PUR		polyurethane
P_V	$[m^{-3}]$	numerical density
px		pixel
Q, ϕ, X		point set
Q_i		modified pixel contrast value
r	$[m]$	radius of a circle cross section
R, R	$[-], [m^3]$	region, sphere radius
RGB		red-green-blue colour space
R_{max}	$[m]$	radius of the biggest sphere
ROI	$[m^2]$	region of interest
S	$[m^2]$	cross section area
SEM		scanning electron microscope / microscopy
$St.Th, St.Sp$	$[m]$	structure thickness, structure separation (CT)
S_V	$[m^2/m^3]$	surface area density
SW		software
t	$[m]$	disector thickness
Tab.		table
TEM		transmission electron microscope / microscopy
TS, TV	$[m^2], [m^3]$	total VOI surface, total VOI volume (CT)
V	$[m^3]$	volume
VOI	$[m^3]$	volume of interest
vs.		<i>versus</i>
VT		Voronoi tessellation
V_V	$[m^3/m^3]$	volume fraction
x		general denotation for a quantity
X		cutting plane (structure model)
x, y, X, Y		coordinates
x_1, \dots, x_n		members of set Q
X^c		supplement of the set X
Z_{o_max}		maximum resolution of the optical microscope

Symbol	Dimension	Meaning(s)
Z_{SEM}, Z_{TEM}		maximum resolution of SEM, maximum resolution of TEM
α	[-]	sound absorption coefficient
α, β		material phases
$\alpha\alpha, \alpha\beta$		phase interfaces
Δ^2		sum of least squares
ε^2		2D Euclidean space
λ	[m]	wavelength
μ		mean value of a distribution
π	3.14159265	pi number
ρ	[kg/m ³]	material density
σ, σ_r	[-], [m]	standard deviation /standard deviation of radii
Ω_c (40%)	[Pa]	resistance to compression
*.csv		coma separated values file
*.log		list-of-actions file
*.TIFF		tagged image file format
\in		set membership / is an element of
\subset		is a subset of
\cap		intersected with
∞		infinity
\ominus, \oplus		Minkowski's subtraction / Minkowski's addition

LIST OF FIGURES

Fig. 1: Scope of stereometry and stereology. Scheme redrawn from [17].	10
Fig. 2: Relations between basic stereological 3D entities and corresponding 2D projections. Redrawn from [23].	12
Fig. 3: Basic types of stereological probes. Redrawn from [23].	13
Fig. 4: Events caused by interactions of probes with objects. Redrawn from [24].	13
Fig. 5: A transverse cut through the apple showing the loss of the original structure information, when cut by plane. Picture of apple from source [35], modified.	14
Fig. 6: Counting point fraction with point probes, redrawn from [19].	16
Fig. 7: Counting number of particle intersections by line probe L_T – a) two phases with the particles separated from each other, b) two phases with particles joined together, redrawn from [19].	16
Fig. 8: a) the object boundary stretched around the pixels' boundaries, b) "smoothing" the perimeter of the object, c) the connector of the centres of the outer pixels, d) "smoothing" the perimeter with preserved real area of the object, redrawn from [3].	17
Fig. 9: Linear testing grids for P_L measurements on oriented structures, redrawn from [19].	17
Fig. 10: Cycloid curve inscribed in the rectangle of height h , redrawn from [36].	18
Fig. 11: Cycloid-based grid, for vertical sections, redrawn from [39].	18
Fig. 12: Cycloid grid, redrawn from [38].	18
Fig. 13: Spatial linear object Y intersecting plane T is in 2D seen as a set of points, redrawn from [22].	19
Fig. 14: Counting the number of vertices belonging to three neighbouring objects. The points are highlighted by grey circles, redrawn from [19].	19
Fig. 15: Patterns of ASTM E112 for comparison procedure, redrawn from [37].	21
Fig. 16: Gundersen's rule of particle selection, redrawn from [44].	22
Fig. 17: Example of Gundersen's selection rule [44].	22
Fig. 18: Naturally-occurring tessellation – example I: a honeycomb [51].	23
Fig. 19: Naturally-occurring tessellation – example II: a tortoiseshell [52].	23
Fig. 20: Man-made tessellation – example I: pavement tiles [53].	24
Fig. 21: Man-made tessellation – example II: Gaudi's mosaic in Barcelona [54].	24
Fig. 22: Types of Voronoi tessellations: From left to right: Poisson-Voronoi tessellation, Bookstein tessellation, tessellation generated by cluster field, redrawn from [47].	25
Fig. 23: Poisson tessellation, redrawn from [47].	26
Fig. 24: Delaunay tessellation (dashed), induced by generators of Voronoi tessellation cells (solid lines), redrawn from [47].	26
Fig. 25: Induced tessellation (planar cut through spatial Voronoi tessellation), redrawn from [47].	27
Fig. 26: A set of spheres with the constant diameter serving as a model of monodisperse particular system.	28
Fig. 27: Model of bidisperse system containing big and small spheres with the radii ratio between them 2:3.	28
Fig. 28: Model of generally polydisperse system containing range of spheres with various sizes.	28
Fig. 29: Planar section through soft polyurethane foam as the example of real polydisperse structure.	28
Fig. 30: Generalized sketch of Wicksell's corpuscle problem, redrawn from [50].	29

Fig. 31: Random cutting planes intersecting a general polydisperse structure.	30
Fig. 32: Comparison of planar sections through the spheres A and B. Situation corresponds to Fig. 31.	30
Fig. 33: Normal (Gaussian) distribution.	32
Fig. 34: Log-normal distribution.	32
Fig. 35: Comparison of cross section radii (r) distribution with the corresponding sphere radii (R) normal distribution.	33
Fig. 36: Model of bimodal distribution.	33
Fig. 37: Comparison of cross section radii (r) distribution with the corresponding sphere radii (R) bimodal distribution.	34
Fig. 38: Area of cross sections – distribution corresponding to the size distribution in Fig. 35.	35
Fig. 39: Area of cross sections – distribution corresponding to the size distribution in Fig. 36.	35
Fig. 40: A micrograph of the spherulitic structure of polypropylene, [46].	35
Fig. 41: The principle of scanning, redrawn from [80].	36
Fig. 42: Scheme of DSLR digital camera, redrawn from [81].	36
Fig. 43: Scheme of an optical microscope, redrawn from [92].	37
Fig. 44: Schematic illustration of scanning electron microscope [93].	38
Fig. 45: A cut through transmission electron microscope [94].	39
Fig. 46: Scheme of an X-ray micro-CT, redrawn from [95].	40
Fig. 47: Stamping method. Left: Scanned image of foam structure covered with contrasting ink for enhancing the pore cross sections boundaries. Right: Binarized scan [63].	41
Fig. 48: N_V estimation by means of disector measurement [3].	42
Fig. 49: Visible spectrum with the bands corresponding to the colours of rainbow.	44
Fig. 50: Construction of the CIE triangle, redrawn from [115].	45
Fig. 51: Visible gamut according to CIE triangle. The values on the perimeter show wavelengths [116].	45
Fig. 52: Gamut comparison – region A – visible gamut, region B – RGB gamut, region C – CMYK gamut, redrawn from [119].	46
Fig. 53: Principle of colour mixing in monitors and printers [118].	46
Fig. 54: Alteration of feature shape after eroding, redrawn from [3].	50
Fig. 55: Scheme of the effect of dilation, redrawn from [3].	51
Fig. 56: Opening vs. closing, redrawn from [3].	51
Fig. 57: The effect of dilation and erosion on the resulting shape of the initially circular object, redrawn from [3].	52
Fig. 58: The effect of EDM on the shape – both enlarging and shrinking preserve the shape of the original object, redrawn from [3].	52
Fig. 59: Eight-pointed star and its skeleton.	53
Fig. 60: Principle of skeletonization [123].	53
Fig. 61: Watershed segmentation [147].	54
Fig. 62: SkyScan 1174 X-ray microtomograph [148].	56
Fig. 63: Preparing the samples for CT scanning.	56
Fig. 64: XY plane grey projection of the sample 4070. The black line A-A denotes one reconstructed slice.	59
Fig. 65: Reconstructed transverse cross sectional slice of the sample 4070 corresponding with the line A-A in Fig. 64.	59

Fig. 66: a) FFOV image of a reconstructed slice (Sample HR4250) – the sample is surrounded by air; selected round-shaped ROI is highlighted by light grey circle, b) ROI saved from the FFOV image.	61
Fig. 67: a) Detail of ROI corresponding with Fig. 66b, b) binarized ROI image where white areas represent the struts.....	61
Fig. 68: FFOV – reconstructed image from CT (sample HR4250) – the sample is surrounded by blank space.	64
Fig. 69: Cropped reconstructed image; the image corresponds with the black square area in the foregoing image.	65
Fig. 70: Enhanced contrast of the image caused by the shadow filters plug-ins.....	65
Fig. 71: Thresholded image.	65
Fig. 72: EDM – the lightest area represent the centres of pores cross sections.	66
Fig. 73: EDM maxima approximated by the centres of circles inscribed to the individual pores cross sections.....	66
Fig. 74: Voronoi Tessellation network as the approximation of pores cross sections boundaries.....	66
Fig. 75: Experimental data (sample HR4250) extracted from the tessellation networks fitted by the model curve – virtual distribution of pore cross section area with the parameters μ and σ found to be the closest to the real distribution – model output.....	67
Fig. 76: Scheme of the structural model – the interval $\langle 0; Er + 3\sigma \rangle$ determines all possible positions of the cutting plane X.	68
Fig. 77: Left: original FFOV of reconstructed single slice image (HR4250) with the highlighted ROIs – circular used for CT, square used for VT method; Right up: detail of the CT-ROI applied on the binarized image, magnified 1.1x, the scale bar applies for both ROI details; Right down: VT network placed over the binarized image within VT-ROI.	70
Fig. 78: Comparison of measured (CT) and estimated (model) pore size distributions – HR4250.....	71
Fig. 79: Left: original FFOV of reconstructed single slice image (CMHR6052) with the highlighted ROIs – circular used for CT, square used for VT method; Right up: detail of the CT-ROI applied on the binarized image, magnified 1.1x, the scale bar applies for both ROI details; Right down: VT network placed over the binarized image within VT-ROI.	71
Fig. 80: Comparison of measured (CT) and estimated (model) pore size distributions – CMHR6052.	72
Fig. 81: Left: original FFOV of reconstructed single slice image (PANTERA100) with the highlighted ROIs – circular used for CT, square used for VT method; Right up: detail of the CT-ROI applied on the binarized image, magnified 1.1x, the scale bar applies for both ROI details; Right down: VT network placed over the binarized image within VT-ROI.	73
Fig. 82: Comparison of measured (CT) and estimated (model) pore size distributions – PANTERA100.	74
Fig. 83: Left: original FFOV of reconstructed single slice image (4070) with the highlighted ROIs – circular used for CT, square used for VT method; Right up: detail of the CT-ROI applied on the binarized image, magnified 1.1x, the scale bar applies for both ROI details; Right down: VT network placed over the binarized image within VT-ROI.....	74
Fig. 84: Comparison of measured (CT) and estimated (model) pore size distributions – 4070.....	75
Fig. 85: Left: original FFOV of reconstructed single slice image (HR5050) with the highlighted ROIs – circular used for CT, square used for VT method; Right up: detail of the CT-ROI applied on the binarized image, magnified 1.1x, the scale bar applies for both ROI details; Right down: VT network placed over the binarized image within VT-ROI.	76

Fig. 86: Comparison of measured (CT) and estimated (model) pore size distributions – HR5050.77	77
Fig. 87: Left: original FFOV of reconstructed single slice image (3050) with the highlighted ROIs – circular used for CT, square used for VT method; Right up: detail of the CT-ROI applied on the binarized image, magnified 1.1x, the scale bar applies for both ROI details; Right down: VT network placed over the binarized image within VT-ROI.	77
Fig. 88: Comparison of measured (CT) and estimated (model) pore size distributions – 3050. .78	78
Fig. 89: Left: original FFOV of reconstructed single slice image (2545) with the highlighted ROIs – circular used for CT, square used for VT method; Right up: detail of the CT-ROI applied on the binarized image, magnified 1.1x, the scale bar applies for both ROI details; Right down: VT network placed over the binarized image within VT-ROI.	79
Fig. 90: Comparison of measured (CT) and estimated (model) pore size distributions – 2545. .80	80
Fig. 91: Left: original FFOV of reconstructed single slice image (2340) with the highlighted ROIs – circular used for CT, square used for VT method; Right up: detail of the CT-ROI applied on the binarized image, magnified 1.1x, the scale bar applies for both ROI details; Right down: VT network placed over the binarized image within VT-ROI.	80
Fig. 92: Comparison of measured (CT) and estimated (model) pore size distributions – 2340. .81	81
Fig. 93: Left: original FFOV of reconstructed single slice image (2015) with the highlighted ROIs – circular used for CT, square used for VT method; Right up: detail of the CT-ROI applied on the binarized image, magnified 1.1x, the scale bar applies for both ROI details; Right down: VT network placed over the binarized image within VT-ROI.	82
Fig. 94: Comparison of measured (CT) and estimated (model) pore size distributions – 2015. .83	83
Fig. 95: Left: original FFOV of reconstructed single slice image (3545) with the highlighted ROIs – circular used for CT, square used for VT method; Right up: detail of the CT-ROI applied on the binarized image, magnified 1.1x, the scale bar applies for both ROI details; Right down: VT network placed over the binarized image within VT-ROI.	83
Fig. 96: Comparison of measured (CT) and estimated (model) pore size distributions – 3545. .84	84
Fig. 97: Mean volumes of the individual samples ordered in ascending manner according EV_1 .	85
Fig. 98: Correlation between the EV_3 and EV_1	86
Fig. 99: Correlation between the EV_3 and EV_2	86
Fig. 100: The mutual dependence of acoustic absorption coefficient and frequency for all measured materials.	87
Fig. 101: Maximum damping frequency dependence on mean pore size.	88
Fig. 102: a) original surface scan of the dried bread slice, b) binarized structure, c) EDM applied to the binarized image, d) inscribed circles fitting on the basis of EDM result.	89
Fig. 103: Bread scan (left) vs. final Voronoi tessellation placed over the binarized image.	90
Fig. 104: a) original micrograph of the resin-metal composite, b) binarized structure, c) EDM applied to the binarized image, d) inscribed circles fitting on the basis of EDM result.	91
Fig. 105: Original micrograph of the resin-metal composite (left) vs. final Voronoi tessellation placed over the binarized image.	91
Fig. 106: a) original micrograph of the scratch pattern, b) binarized structure, c) EDM applied to the binarized image, d) inscribed circles fitting on the basis of EDM result.	92
Fig. 107: Original micrograph of the alloy starch pattern (left) vs. final Voronoi tessellation placed over the binarized image.	93

LIST OF TABLES

Tab. 1: Overview of studied flexible PUR foams ordered according to the material density in ascending manner.	55
Tab. 2: Overview of studied flexible PUR foams ordered according to the material density in ascending manner	58
Tab. 3: Comparison of results from CT and VT + model parameters – Sample HR4250.	70
Tab. 4: Comparison of results from CT and VT + model parameters – Sample CMHR6250.	72
Tab. 5: Comparison of results from CT and VT + model parameters – Sample PANTERA100.	73
Tab. 6: Comparison of results from CT and VT + model parameters – Sample 4070.	75
Tab. 7: Comparison of results from CT and VT + model parameters – Sample HR5050.	76
Tab. 8: Comparison of results from CT and VT + model parameters – Sample 3050.	78
Tab. 9: Comparison of results from CT and VT + model parameters – Sample 2545.	79
Tab. 10: Comparison of results from CT and VT + model parameters – Sample 2340.	81
Tab. 11: Comparison of results from CT and VT + model parameters – Sample 2015.	82
Tab. 12: Comparison of results from CT and VT + model parameters – Sample 3545.	84
Tab. 13: Overview of acoustic absorption coefficients at characteristic frequencies, NRC coefficient and maximum acoustic damping for all investigated materials.	88

REFERENCES

- [1] BUNGE, H.J. et al.: Elastic properties of polycrystals—influence of texture and stereology; *Journal of the Mechanics and Physics of Solids*; 48(1);2000; pp. 29-66.
- [2] DZIADUR, W: The effect of some elastomers on the structure and mechanical properties of polyoxymethylene; *Materials Characterization*; 46(2-3); 2001; pp. 131-135.
- [3] RUSS, J.C.: *Image analysis of food microstructure*. Boca Raton: CRC Press; 2005. 369 p. ISBN 0-8493-2241-3.
- [4] CHEN, P.-Y. et al.: Structure and mechanical properties of selected biological materials; *Journal of the Mechanical Behavior of Biomedical Materials*; 1(3); 2008; pp. 208-226.
- [5] CAO, J., LÜ Q-F: Crystalline structure, morphology and mechanical properties of β -nucleated controlled-rheology polypropylene random copolymers; *Polymer Testing*, 30(8); 2011; pp. 899-906.
- [6] FERNANDES, C.M. et al.: Microstructure-property relations in composite yttria-substituted zirconia solid electrolytes; *Solid State Ionics*; 2011; 193(1); pp. 52-59.
- [7] PEGEL, S. et al.: Spatial statistics of carbon nanotube polymer composites; *Polymer*; 50(9); 2009; pp. 2123-2132.
- [8] LIVELY, B. et al.: Quantified stereological macrodispersion analysis of polymer nanocomposites; *Composites Part A: Applied Science and Manufacturing*; 43(6); 2012; pp. 847-855.
- [9] SAXL, I., PONÍŽIL, P.: Grain size estimation: w–s diagram; *Materials Characterization*; 46(2-3); 2001; pp. 113-118.
- [10] FILIPOVIC, M. et al.: Microstructure and mechanical properties of Fe–Cr–C–Nb white cast irons; *Materials & Design*; 47; 2013 pp. 41-48.
- [11] ZHAO, L. et al.: Structural analysis of poly(butylene adipate) banded spherulites from their biodegradation behavior; *Polymer*; 48(20); 2007 pp. 6152-6161.
- [12] STORM, J., et al.: Geometrical modelling of foam structures using implicit functions; *International Journal of Solids and Structures*; 50(3-4); 2013; pp. 548-555.
- [13] MATOUŠEK, T., PONÍŽIL, P., GALETKA, M.: Pore size distribution in foams; *Key Engineering Materials*; 465; 2011; pp. 145-148.
- [14] SHEN, H. et al.: Numerical modelling of pore size and distribution in foamed titanium; *Mechanics of Materials*; 38; 2006; pp. 933-944.
- [15] WERNER, J. et al.: Production of ceramic membranes with different pore sizes for virus retention; *Journal of Water Processing Engineering*; 4; 2014; pp. 201-211.
- [16] EUCLID: *Euclid's Elements*; FITZPATRICK, R. (Ed.). Raleigh: Lulu Press, 2007, 544 p. ISBN: 978-0-9151-7984-1
- [17] MOUTON, P. R.: *Unbiased Stereology: A Concise Guide*. Baltimore: JHU Press, 2011, 200 p.; ISBN: 978-0-8018-9984-3.
- [18] GLASER, J.R., GREENE, G., HENDRICKS, S.J: *Stereology for Biological Research*. Williston: MBF Press, 2006. 94 p. ISBN: 0-9786471-0-6.

- [19] UNDERWOOD, E.E.: *Quantitative stereology I*. New York: Addison-Wesley Educational Publishers Inc., U.S., 1970, 274 p. ISBN 978-020107650-9.
- [20] MIYAMOTO, K.: Particle Number and Sizes Estimated from Sections – A History of Stereology in TAKAKI, R. (ed.) *Research of Pattern Formation*. Tokio: KTK Scientific Publishers, 1994. pp. 507-516; ISBN 4-87677-108-1.
- [21] HILLIARD, J.E., LAWSON, L.R.: *Images and Patterns in Stereology and Stochastic Geometry*. Dordrecht: Kluwer Academic Publishers, 2003. pp. 1-25; ISBN: 1-4020-1687-5.
- [22] BADDELEY, A., VEDEL JENSEN, E.B.: *Stereology for Statisticians*. Boca Raton: Chapman & Hall/CRC, 2005. 395 p. ISBN 1-58488-405-3.
- [23] WEST, M.J.: Introduction to Stereology; *Cold Spring Harbor Protocols*; 8; 2012; pp. 843-851.
- [24] HOWARD C.V., REED M.G: *Unbiased Stereology: Three Dimensional Measurement in Microscopy*. 2nd ed.; New York: Springer-Verlag, 2005. 246 p. ISBN 0-203-00639-9.
- [25] GHUGRE, N.R. et al.: Quantitative analysis and modelling of hepatic iron stores using stereology and spatial statistics; *Journal of Microscopy*; 238(3); 2010; pp. 265-274.
- [26] POURDEYHIMI, B. (ed.): *Imaging and Image Analysis Applications for Plastics*. Norwich: William Andrew Publishing, 1999. 398 p. ISBN 1-884207-81-2.
- [27] BROOKS, L. et al.: Quantified stereological macrodispersion analysis of polymer nanocomposites; *Composites Part A: Applied Science and Manufacturing*; 43(6); 2012; pp. 847-855.
- [28] DÖRRIE, H: „Buffon’s Needle Problem” in *100 Great Problems of Elementary Mathematics – Their History and Solution*; trans. ANTIN, D., New York: Dover Publications inc.; 1965; pp: 73-77; ISBN: 978-0-489-61348-2.
- [29] FENGFAN, X., DEYI, L.: On generalized Buffon needle problem for lattices; *Acta Mathematica Scientia*; 31(1); 2011; pp.303-308.
- [30] THOMSEN, J.S. et al.: Stereological measures of trabecular bone structure: comparison of 3D micro computed tomography with 2D histological sections in human proximal tibial bone biopsies; *Journal of Microscopy*; 218(2); 2005; pp. 171-179.
- [31] QUINN, T.M. et al.: Cell and matrix morphology in articular cartilage from adult human knee and ankle joints suggests depth-associated adaptations to biomechanical and anatomical roles; *Osteoarthritis and Cartilage*; 21(12); 2013; pp. 1904-1912.
- [32] EVANS, S.M., GUNDERSEN, H.J.G.: Estimation of spatial distributions using the nucleator; *Acta Stereologica*; 8; 1989; pp. 395-400.
- [33] BADDELEY, A., VEDEL JENSEN E. B.: *Stereology – sampling in three dimensions*; Online research paper of Department of Mathematics & Statistics of Western Australia and Laboratory for Computational Stochastic and MaPhySto University of Aarhus; [online]; 2002; [cited 2014-11-17]; Available at: <<http://home.imf.au.dk/stoclabb/publications/rr22.pdf>>.

- [34] TONAR, Z.: *Atlas kvantitativní histologie – příručka pro student*; Educational text of Faculty of Medicine in Pilsen Charles University in Prague; [online]; 2008; [cited 2014-11-17]; Available at: http://home.zcu.cz/~tonar/arch/tonar_atlas_text.pdf.
- [35] ŠEVČÍKOVÁ: *Fotoatlas přírody – Jablůň*; Educational webpage of the basic school in Vsetín; [online]; 2010; [cited 2014-11-18]; Available at: <http://fotoatlaspr.zs-sychrov5.sweb.cz/jablon.html>.
- [36] RUSS, J.C., DEHOFF, R.T.: *Practical Stereology*. 2nd ed.; New York: Springer; 2000; 382 p.; ISBN 0-306-46476-4.
- [37] ASTM E112-96(2004), *Standard Test Methods for Determining Average Grain Size*; ASTM International; West Conshohocken, PA; 2004; DOI: 10.1520/E0112-96R04.
- [38] PUDDEPHAT, M.: *Single object stereology (part 2)*; Dr. Mike Puddephat Online; [online]; 2010; [cited 2014-11-23]; Available at: <http://www.mikepuddephat.com/page/1600/single-object-stereology-part-2->.
- [39] KISCHELL, E.: *Grid Cycloid Arc, Grid Cycloid Arc Batch Processor*; [online]; 2003; [cited 2014-11-26]; Available at: <http://rsb.info.nih.gov/ij/plugins/grid-cycloid-arc.html>.
- [40] BADDELEY, A.J., GUNDERSEN, H.J.G.; CRUZ-ORIVE, L.M.: Estimation of surface area from vertical sections. *Journal of Microscopy*; 142(3); 1986; pp. 259-276.
- [41] CRUZ-ORIVE; L.M.; HOWARD C.V.: Estimation of individual feature surface area with the vertical spatial grid; *Journal of Microscopy*; 178(2); 1995; pp. 146-151.
- [42] JEFFRIES, Z., KLINE, A.H., ZIMMER, E.B.: Determination of grain size in metals; *Transactions of the metallurgical society of AIME*; 57; 1916, pp. 594-607.
- [43] GUNDERSEN, H.J.G.: Notes on the estimation of the numerical density of arbitrary profiles: the edge effect; *Journal of Microscopy*; 111(2); 1977; pp. 219-223.
- [44] *Counting rules: Stereology Information for the Biological Sciences*; [online]; 2012; [cited 2014-11-26]; Available at: <http://www.stereology.info/counting-rules/>.
- [45] ŠEDIVÝ, O.: *Aplikace geometrické statistiky na měření charakteristik rovinných objektů*. Prague, 2006, 98 p., Bachelor's thesis. Charles University in Prague; Faculty of Mathematics and Physics; Department of Probability and Mathematical Statistics; Supervisor: Ivan Saxl.
- [46] ČERMÁK, R., PONÍŽIL, P., SAXL, I.: *Modelling spherulite growth by planar tessellations*; [online]; 2001; [cited 2014-28-11]; Available at: <http://fyzika.ft.utb.cz/spherulites/samplek.htm>.
- [47] PONÍŽIL, P.: *Prostorové teselace – teze k rigorózní zkoušce*. Zlín, 1998, 39 p., Brno University of Technology; Faculty of Technology Zlín; Department of Physics and Materials Engineering; Supervisor: Ivan Saxl.
- [48] STEVENS, D.L., Jr., OLSEN, A. R.: Spatially-balanced sampling of natural resources; *Journal of American Statistical Association*; 99(465); 2004; pp. 262-278.

- [49] REDENBACH, C.: Microstructure models for cellular materials; *Computational Materials Science*; 44(4); 2009; pp. 1397-1407.
- [50] MATOUŠEK, T.: *Foams pore size estimation and their acoustic properties*; Zlín; 2009; 71 p.; Diploma thesis. Tomas Bata University in Zlín; Faculty of Technology Zlín; Department of Physics and Materials Engineering; Supervisor: Petr Ponížil.
- [51] KENNEMER, Q: *Rumor: Honeycomb to Require Dual-Core Processor, Hi-Def Resolution*; [online]; 2001; [cited 2014-11-28]. Available at: <<http://phandroid.com/2011/01/03/rumor-honeycomb-to-require-dual-core-processor-hi-def-resolution/>>.
- [52] SIEGEL, R.: *Turtles*; [online]; 2006; [cited 2014-11-28]; Available at: <<http://www.stanford.edu/~siegelr/animalz/turtles.html>>.
- [53] *Tessellation*. URL: <<http://en.wikipedia.org/wiki/Tessellation>>; [cited 2014-11-28];
- [54] *Pictures of Park Guell by Antoni Gaudi*. URL: <<http://www.barcelonayellow.com/bcn-photos/80-pictures-parc-guell>>; [cited 2014-11-28];
- [55] DEREUDRE, D., LAVANCIER, F.: Practical simulation and estimation for Gibbs Delaunay-Voronoi tessellations with geometric hardcore interaction; *Computational Statistics & Data Analysis*; 55(1); 2011; pp. 498-519.
- [56] CHAVEY, D.P.: A Catalog of Tilings by Regular Polygons; *Computers & Mathematics with Applications*; 17; 1989; pp. 147-165.
- [57] HORNE, C.E.: *Geometric Symmetry in Patterns and Tilings*; Abington: Woodhead Publishing; 2000; 238 p.; ISBN: 978-1-85573-492-0.
- [58] WINTER, L.: *Why Do Honey Bees Make Hexagonal Honeycomb?*; [online]; 2014; [cited 2014-11-28]; Available at: <<http://www.iflscience.com/physics/why-do-honey-bees-make-hexagonal-honeycomb>>.
- [59] WEJRZANOWSKI, T. et al.: Structure of foams modeled by Laguerre-Voronoi tessellations; *Computational Materials Science*; 67; 2013; pp. 216-221.
- [60] JEULIN, D.: Random tessellation generated by Boolean random functions; *Pattern Recognition Letters*; 47; 2014; pp. 139-146.
- [61] SAXL I., PONÍŽIL, P., SÜLLEIOVÁ K.: Grain size estimation in anisotropic materials; *Material Science Forum*; 482; 2005; pp. 239-242.
- [62] AL-MULA, A.: Investigation on the Applicability of Johnson-Mehl-Avrami Equation for the Kinetic Analysis of Crystallization in Polyalkylene Terephthalates; *Kuwait Journal Of Science and Engineering*; 38; 2011; pp.245-257.
- [63] MATOUŠEK, T. et al.: Pore size estimation; *Proceeding of 4th WSEAS International Conference on ENGINEERING MECHANICS, STRUCTURES, ENGINEERING GEOLOGY (EMEGEG '11)*, 14th-16th. July 2011, Corfu, Greece, pp. 372-377; ISBN 978-1-61804-022-0.
- [64] BEIL, M., et al.: Fitting of random tessellation models to keratin filament network; *Journal of Theoretical Biology*; 241(1); 2006; pp. 62-72.
- [65] KRAUS, M., RAJAGOPAL, A., STEINMANN, P: Investigations on the polygonal finite element method: Constrained adaptive Delaunay tessellation and conformal interpolants; *Computers & Structures*; 120; 2013, pp. 33-46.

- [66] PARDO-ALONSO, S., et al.: 3D Analysis of the progressive modification of the cellular architecture in polyurethane nanocomposite foams via X-ray microtomography; *European Polymer Journal*; 49(5); 2013; pp. 999-1006.
- [67] PARK, J.K., et al.: Preparation of PS/TiO₂ as a white pigment for electrophoretic displays; *Current Applied Physics*; 13; 2013; pp.1231-1236.
- [68] McKEEN, L.W.: *The Effect of Temperature and other Factors on Plastics and Elastomers*. 3rd ed.; Waltham, MA USA: Springer; 2014; 463 p.; ISBN 978-0-323-31016-1.
- [69] MORGAN, D.J., JERRAM D.A.: On estimating crystal shape for crystal size distribution analysis; *Journal of Volcanology and Geothermal Research*; 154(1-2); 2006; pp. 1-7.
- [70] LI, K., GAO, X.-L., SUBHASH, G.: Effects of cell shape and strut cross-sectional area variations on the elastic properties of three-dimensional open-cell foams; *Journal of the Mechanics and Physics of Solids*; 54(4); 2006; pp 783-806.
- [71] ZHANG, T.: A general constitutive relation for linear elastic foams; *International Journal of Mechanical Sciences*; 50(6); 2008; pp. 1123-1132.
- [72] CHEN, Y., DAS, R. BATTLE, M.: Effects of cell size and cell wall thickness variations on the stiffness of closed-cell foams; *International Journal of Solids and Structures*; 52; 2015; pp. 150-164.
- [73] PORTA, G.D., CAMPARDELLI, R., REVERCHON, E.: Monodisperse biopolymer nanoparticle by Continuous Supercritical Emulsion Extraction; *The Journal of Supercritical Fluids*; 76; 2013; pp. 67-73.
- [74] WICKSELL, S.D.: The corpuscle problem I; *Biometrika*; 17; 1925; pp. 84 – 99.
- [75] WICKSELL, S.D.: The corpuscle problem II; *Biometrika*; 18; 1926; pp. 152 – 172.
- [76] MELOUN, M., MILITKÝ, J.: *Kompendium statistického zpracování dat : metody a řešené úlohy*; Praha: Academia; 2006; 970 p. ISBN: 978-80-200-2071-0.
- [77] WANG, J et al.: Morphology and mechanical properties of polypropylene/poly(propylene-1-octene) in-reactor alloys prepared by Metallocene/ Ziegler-Natta hybrid catalyst; *Polymer*; 53(7); 2012; pp.1507-1516.
- [78] THÓRISDÓTTIR, Ó., KIDERLEN, M.: Wicksell's Problem in Local Stereology; *Advances in Applied Probability*; 45(4); 2013; pp. 925-294.
- [79] COX, D.R., DONNELLY, C.A.: *Principles of Applied Statistics*; Cambridge: Cambridge University Press; 2011; 202 p. ISBN: 978-1-107-01359-9.
- [80] TYSON, J.: *How Scanners Work*; [online]; 2001; [cited 2014-12-03]; Available at: <<http://computer.howstuffworks.com/scanner.htm>>.
- [81] KOCOUR, P.: *Technické zpracování digitální fotografie pro učitele* [online]; Educational text of University of West Bohemia in Pilsen; 2011; [cited 2014-12-06]. Available at: <<http://www.kvd.zcu.cz/cz/materialy/DIFOU/index2.htm>>.
- [82] BLACKWELL, H.R.: Contrast thresholds of the human eye; *Journal of the Optical Society of America*; 36(11); 1946; pp. 624-643; DOI: 10.1364/JOSA.36.000624.

- [83] CLARK, R.N.: *Experiments with Pixels Per Inch (PPI) on Printed Image Sharpness* [online]; 2003; [cited 2014-12-04]; Available at: <<http://www.clarkvision.com/articles/printer-ppi/>>.
- [84] PELZBAUER, Z.: *Morfologie a mikroskopie polymerů V: Základy fyziky pevných polymerů*; POUCHLÝ, J., LEDNICKÝ, F., RAAB, M (ed.); Prague: Department of macromolecular chemistry, The Czechoslovak academy of sciences; Edition Macro; M – 16; 1987.
- [85] LETHO, P. et al.: Influence of grain size distribution on the Hall-Petch relationship of welded structural steel; *Materials Science and Engineering: A*; 592(13); 2014; pp. 28-39.
- [86] LEWIS, A., et al.: Near-field scanning optical microscopy in cell biology; *Trends in cell biology*; 9(2); 1999; pp. 70-73.
- [87] ANTOLOVIĆ, V. et al.: A simple optical configuration for cell tracking by dark field microscopy; *Journal of Microbiological Methods*, 104; 2014; pp. 9-11.
- [88] SITU, G., et al. Phase contrast enhancement in microscopy using spiral phase filtering; *Optics Communications*; 283(7); 2010; pp. 1273-1277.
- [89] FEDOSSEEV, R. Et al.: Structured light illumination for extended resolution in fluorescence microscopy; *Optics and Lasers in Engineering*; 43(3-5); 2005; pp. 403-414.
- [90] KALUS, R.: *Trivium z optiky* [online]; Educational text of University of Ostrava, 2004, [cited 2014-12-07]; Available at: <<http://artemis.osu.cz:8080/artemis/view.php?ids=1&idr=1&idc=33>>.
- [91] NEBESÁŘOVÁ, J: *Elektronová mikroskopie pro biology* [online]; Educational text of the laboratories of elektron microscopy, Institute of parasitology; 2001; [cited 2014-12-07]; Available at: <<http://www.paru.cas.cz/lem/book/Podkap/2.1.html>>.
- [92] DAY, S.A: *A level notes: magnification* [online]; 2012; [cited 2014-12-08]; Available at: <<http://alevelnotes.com/Magnification/106>>.
- [93] *Scanning electron microscope*; URL: <<http://www.udel.edu/biology/Wags/histopage/illuspage/lec1/sem.jpg>>; [cited 2014-12-08].
- [94] Transmission electron microscope; URL: <<http://www.udel.edu/biology/Wags/histopage/illuspage/lec1/iintro9.gif>>; [cited 2014-12-08].
- [95] KAK, A.C., SLANEY, M: *Principles of Computized Tomographic Imaging*; New York: IEEE Press; 1988; 327 p.; ISBN 0-87942-198-3.
- [96] TRAN, T., CAUDILL, M.: Using computer tomography and digital image processing techniques to measure blow molded objects; *Proceedings of ANTEC 1998 Plastics: Plastics on My Mind*; Vol. 3: Special Areas.
- [97] LIM, K.S., BARIGOU, M.: X-ray micro-computed tomography of cellular food products; *Food Research International*; 37; 2004; pp. 1001-1012.
- [98] PETRASCH, J., WYSS, P., STEINFELD, A.: Tomography-based Monte Carlo determination of radiative properties of reticulate porous ceramics; *Journal of Quantitative Spectroscopy & Radiative Transfer*; 105; 2007; pp. 180-197.
- [99] KETCHAM, R.A., CARLSON, W.D.: Acquisition, optimization and interpretation of X-ray computed tomographic imagery: Applications to the geosciences; *Computers and Geosciences*; 27; 2001; pp. 381-400.

- [100] MARIE, É., ADRIEN, J., PETIT, C.: Structural characterization of solid foams; *Comptes, Rendus Physique*; 15(8-9); 2014; pp. 674-682.
- [101] GÓMEZ, S. et al.: Characterization and three-dimensional reconstruction of synthetic bone model foams; *Materials Science and Engineering: C*; 33(6); 2013; pp. 3329-3335.
- [102] MARIE, É., et al.: Characterization of the morphology of cellular ceramics by 3D image processing of X-ray tomography data; *Journal of The European Ceramic Society*; 27; 2007; pp. 1973-1981.
- [103] SCHRAMM LL, al.: The morphology of non-equilibrium foam and gelled foam lamellae in porous media; *Journal of Petroleum Science and Engineering*; 23(2); 1999; pp. 117-132.
- [104] GERMAIN, J.C., AGUILERA, J.M.; Multi-scale properties of protein-stabilized foams; *Food Structure*; 1(1); 2014; pp.55-70.
- [105] MAUKO, A., et al.: Use of confocal laser scanning microscopy (CLSM) for the characterization of porosity in marble; *Materials Characterization*; 60(7); 2009; pp. 603-609.
- [106] EXNER, H.E.: Stereology and 3D microscopy: Useful alternatives or competitors in the quantitative analysis of microstructures?; *Image Analysis & Stereology*; 23(2); 2004; pp. 73-82.
- [107] MURAI, S.: *Remote sensing note* [online]; Japan Association of Remote Sensing; 1993; 284 p.; [cit. 31.3.2013]. Available at: <<http://www.jars1974.net/pdf>>.
- [108] JOY, J., KURIAKOSE, J.: Adaptive Contrast Binarization Using Standard Deviation for Degraded Document Images; *International Journal of Computer Science Trends and Technology*; 2(4); 2014; pp. 114-118.
- [109] GILL, T.K.: Document Image Binarization Techniques – A Review; *International Journal of Computer Applications*; 98(12); 2014; pp. 1-4.
- [110] JOYCE, T.: *Bit depth vs. dynamic range in Layman's terms*; [online]; Beyond Megapixels; 2012; [cited 2014-12-13]; Available at: <<http://www.beyondmegapixels.com/2012/02/bit-depth-vs-dynamic-range-in-laymans-terms/>>.
- [111] HOBBS, T: *The wonder of light: Bits & Bytes*; [online]; 2009; [cited 2014-12-13]; Available at: <<http://www.thewonderoflight.com/articles/bits-bytes/>>.
- [112] BRAIN, M.: *How Bits and Bytes Work*; [online]; 2000; [cited 2014-12-13]; Available at: <<http://www.howstuffworks.com/bytes.htm>>.
- [113] LILLEY, S.: *How Pixels Are Converted to Bytes*; [online]; 2006; [cited 2014-12-13]; Available at: <http://www.ehow.com/how-does_4616926_pixels-converted-bytes.html>.
- [114] SPERLING, H.G., WRIGHT, A.A., MILLS, L.S.: Color vision following intense green light exposure: Data and a model; *Vision Research*; 31(10); 1991; pp. 1797-1812.
- [115] DOSEDLA, M: *Aplikace počítačové grafiky*; [online]; Masaryk University in Brno, Faculty of Education, Department of Technical Education and Information Science; 2007; [cited 2014-12-14]; Available at: <<http://www.ped.muni.cz/wtech/elearning/apg.pdf>>.

- [116] CIE; URL: <<http://web.vscht.cz/kalcicoa/POCPRE/cie.html>>; [cited 2014-12-14].
- [117] KAISER, J.: *Colorimetric Aspects of the Future Imaging Systems*. Prague: 2005; 199p.; Dissertation thesis; Czech Technical University in Prague; Faculty of Electrical Engineering; Department of Radioelectronics, supervisor: Miloš Klíma.
- [118] ROUBAL, P.: *Počítačová grafika pro úplné začátečníky*; 2nd ed.; Brno: Computer Press; 2003; 171 p.; ISBN: 80-7226-896-1.
- [119] ANG, T.: *Digitální fotografie pro pokročilé*; POSTLER, M. (trans.); Prague: Slovart 2004; 144 p.; ISBN: 80-7209-5633-3.
- [120] SEZGIN, M., SANKUR, B.: Survey over image thresholding techniques and quantitative performance evaluation; *Journal of Electronic Imaging*; 13(1); 2004; pp. 146-165.
- [121] SARMIENTO, C.P.: *Binarizacion de Imagenes*; [online]; [cited 2014-12-14]. Available at: <<http://site-informatica.blogspot.cz/2010/09/binarizacion-de-imagenes.html>>.
- [122] BUKHARI, S.S., SHAFAIT, F., BREUEL, T.M.: Adaptive Binarization of Unconstrained Hand-Held Camera-Captures Document Images; *Journal of Universal Computer Science*; 15(18); 2009; pp. 3343-3363.
- [123] HLAVÁČ, Š., SEDLÁČEK, M.: *Zpracování signálů a obrazů*; 1st ED; Prague: Vydavatelství ČVUT; 2001; 220p.; ISBN- 80-01-02114-9.
- [124] ZHANG, F., HANOCK, E.R.: Graph spectral image smoothing using the heat kernel; *Pattern Recognition*; 41(11); 2008; pp. 3328-3342.
- [125] ZHANG, H. et al.: Image quality assessment based on Prewitt magnitude; *AEU – International Journal of Electronics and Communications*; 67(9); 2013; pp. 799-803.
- [126] KLÍMA, M. et al.: *Zpracování obrazové informace*; Prague: Vydavatelství ČVUT; 1999; 177p.; ISBN-80-01-01-01436-3.
- [127] CHAUDHURI, B.B., CHANDA B.: The equivalence of best plane fit gradient with Robert's, Prewitt's and Sobel's gradient for edge detection and a 4-neighbour gradient with useful properties; *Signal processing*; 6(2); 1984; pp. 143-151.
- [128] KITTLER, J.: On the accuracy of the Sobel edge detector; *Image and Vision Computing*; 1(1); 1983; pp. 37-42.
- [129] DA, F. ZHANG, H.: Sub-pixel edge detection based on an improved moment; *Image and Vision Computing*; 28(12); 2010; pp.1645-1658.
- [130] *Implementace konvoluce a FIR filtru na vícejádrovém signálovém procesoru*. URL: <www.comtel.cz/files/download.php?id=5464>; [cited 2014-12-17].
- [131] VARDAVOULIA, M.I., GASTERATOS, A., ANDREADIS, I: Binary, gray-scale, and vector soft mathematical morphology: Extensions, algorithms, and implementations; *Advances in Imaging and Electron Physics*; 119(1) 2001; pp. 1-53.
- [132] MARTÍNEZ, F.S.J., et al.: Soil aggregate geometry: Measurements and morphology; *Geoderma*; 237-238; 2015; pp. 36-48.

- [133] KIMORI, Y., et al.: Fractal dimension analysis and mathematical morphology of structural changes in actin filaments imaged by electron microscopy; *Journal of Structural Biology*; 176(1); 2011; pp. 1-8.
- [134] MATHERON, G.: *Random Sets and Integral Geometry (Probability & Mathematical Statistics)*; New York: John Wiley & Sons; 1975; 288 p.; ISBN: 978-0-47157-621-1.
- [135] POTTMANN, H., et al.: Industrial geometry: recent advances and applications in CAD; *Computer-Aided Design*; 37(7); 2005; pp. 751-766.
- [136] YANG, M.-H., KRIEGMAN, D.J.; AHUJA, N.: Detecting Faces in Images: A Survey; *IEEE Transactions on Pattern Analysis and Machine Intelligence*; 24(1); 2002; pp. 34-58.
- [137] GLASBEY, C.A., HORGAN, G.W.: *Image Analysis for the Biological Sciences*; 1st Ed.; Edinburgh: Wiley; 1995; 230 p.; ISBN: 978-0471937265.
- [138] HEIJMANS, H.J.A.M.: The algebraic basis of mathematical morphology. Part I: Dilations and Erosions; *Computer Vision, Graphics, and Image Processing*; 49(3); 1990; p. 407.
- [139] PAN, Y., LI, K.: Constant-time algorithm for computing the Euclidean distance maps of binary images on 2D meshes with reconfigurable buses; *Information Sciences*; 120(1-4); 1999; pp. 209-221.
- [140] WONG, H.S., BUENFELD, N.R.: Euclidean Distance Mapping for computing microstructural gradients at interfaces in composite materials; *Cement and Concrete Research*; 36(6); 2006; pp. 1091-1097.
- [141] PUDNEY, C.: Distance-Ordered Homotopic Thinning: A Skeletonization Algorithm for 3D Digital Images; *Computer Vision and Image Understanding*; 72(3); 1998; pp. 404-413.
- [142] LONCARIC, S.: A Survey of Shape Analysis Techniques; *Pattern Recognition*; 31(8); 1998; pp. 983-1001.
- [143] CORNEA, N.D., SILVER, D., MIN, P.: *Curve-Skeleton Properties, Applications and Algorithms*; Proceedings of IEEE Visualization; Oct. 23rd-28th 2005; Minneapolis, MN pp. 95-102; ISBN: 0-7803-9462-3; DOI: 10.1109/VISUAL.2005.1532783.
- [144] IVANOV, D., KUZMIN, E., BURTSEV, S.: An efficient integer-based skeletonization algorithm; *Computers & Graphics*; 24(1); 2000; pp. 41-51.
- [145] ZHANG, X., et al.: A marker-based watershed method of X-ray image segmentation; *Computer Methods and Programs in Biomedicine*; 113(3); 2014; pp. 894-903.
- [146] JUNG, C.R.: Combining wavelets and watersheds for robust multiscale image segmentation; *Image and Vision Computing*; 25(1); 2007; pp. 24-33.
- [147] *Watershed*; URL: <<http://rsbweb.nih.gov/ij/docs/menus/process.html>>; [cited 2014-12-18].
- [148] *SkyScan 1174*; URL: <<http://www.sauberkeit-und-reinraum.com/wp-content/uploads/2011/11/Mikrotomographie-SkyScan-Modell-1174.jpg>>; [cited 2014-12-19].
- [149] Compact X-Ray micro-CT, SkyScan 1174v2, *Instruction Manual*, 2009.
- [150] BOAS, F.E., FLEISCHMANN, D: CT artifacts: causes and reduction techniques; *Imaging in medicine*; 4(2); 2012; pp. 229-240.

- [151] HILDEBRAND, T. RUEGSEGGER, P.: A new method for the model-independent assessment of thickness in three-dimensional images; *Journal of microscopy*; 185(1); 1997; pp. 67-75.
- [152] ASTM C423-99a (2001), *Standard Test Methods for Sound absorption and sound absorption coefficients by the reverberation room method*; ASTM International; West Conshohocken, PA; 2001; DOI: 10.1520/C0423-99A.
- [153] DVOŘÁKOVÁ, P., et al.: Baking quality of wheat-rye mixtures; *MendelNet 2011 proceedings*; 23rd Nov 2011, Brno, Mendel University in Brno; pp. 568-578; ISBN: 978-80-7375-563-8.
- [154] KOLLÁR, P., et al.; Steinmetz law in iron–phenolformaldehyde resin soft magnetic composites; *Journal of Magnetism and Magnetic Materials*; 353(1); 2014; pp. 65-70.
- [155] MATOUŠEK, T. et al.: Estimation of resin distribution in sintered powder material; *Fractography 2012 – Book of abstracts*; 21st-24th Oct., 2012, Stará Lesná, Institute of Materials Research of the Slovak Academy of Science, Košice, Slovak Republic; p. 55; ISBN 978-80-970964-2-7.

LIST OF PUBLICATIONS

Research papers:

- MATOUŠEK, T., PONÍŽIL, P., GALETKA, M.: Pore Size Distribution in Foams, *Key Engineering Materials*, 2011, 465 (Materials Structure & Micromechanics of Fracture VI, Ed. P. Šandera), pp. 145-148, ISBN: 978-3-03785-006-0.
- MATOUŠEK, T., FOJTŮ, D., PONÍŽIL P.: Pore size distribution estimation of soft polyurethane foams from planar section images; *Journal of Cellular Plastics*, *manuscript in review*.

Conference papers / proceedings

a) national

- MATOUŠEK, T., PONÍŽIL, P., GALETKA, M.: Struktura a vlastnosti polymerních pěn s otevřenými póry, *Sborník konference Plastko 2010*, p. 244, 13th-14th Apr. 2010, Zlín, Tomas Bata University in Zlín, ISBN: 978-80-7318-909-9.
- DVOŘÁKOVÁ, P., BUREŠOVÁ, I., KRÁČMAR, S., MATOUŠEK, T., PONÍŽIL, P., KUČEROVÁ, J., FAMĚRA, O.: Baking quality of wheat-rye mixtures, *Sborník konference MendelNet 2011*, pp. 568-578, 23rd Nov 2011, Brno, Mendel University in Brno, ISBN: 978-80-7375-563-8.
- MATOUŠEK, T., PONÍŽIL, P., KŘEMEN, F., DVOŘÁKOVÁ, P., BUREŠOVÁ, I.: Odhad distribuce velikosti pórů, *Sborník konference Plastko 2012*, p. 258, 11th-12th Apr. 2012, Zlín, Tomas Bata University in Zlín, ISBN: 978-80-7454-137-7.

b) international

- MATOUŠEK, T., PONÍŽIL, P., GALETKA, M.: Pore Size Distribution in Foams, *6th International Conference on Materials Structure & Micromechanics of Fracture (MSMF6)*, June 28th-30th June 2010, Brno, Brno University of Technology, Czech Republic, p. 143, Proceedings Editor P. Šandera, ISBN: 978-80-214-4112-5.
- MATOUŠEK, T., PONÍŽIL, P., KŘEMEN, F., BUREŠOVÁ, I., DVOŘÁKOVÁ, P.: Pore size estimation, *4th WSEAS International Conference on ENGINEERING MECHANICS, STRUCTURES, ENGINEERING GEOLOGY (EMESG '11)*, 14th-16th July 2011, Corfu Island, Greece, pp. 372-377, Proceedings Editor N. Mastorakis – Technical University of Sofia, Bulgaria., ISBN 978-1-61804-022-0.
- MATOUŠEK, T., GRULICH, O., PONÍŽIL, P.: Promoting the biodegradability of polymers using plasma treatment, *Potential and Applications of surface Nanotreatment of Polymers and Glass (PASNPG) - Book of Extended Abstracts*, 15th-17th Oct. 2012, Hustopeče u Brna, MUNI Press, Brno, Czech Republic, ISBN 978-80-210-5979-5.

- MATOUŠEK, T., PONÍŽIL, P., BUREŠ, R., FÁBEROVÁ, M.: Estimation of resin distribution in sintered powder material, *Fractography 2012 – Book of abstracts*, 21st-24th Oct., 2012, Stará Lesná, Institute of Materials Research of the Slovak Academy of Science, Košice, Slovak Republic, p. 55, ISBN 978-80-970964-2-7.

CURRICULUM VITAE

Name: Tomáš Matoušek
Date of birth: 14th August 1985
Place of birth: Zlín
Address: Na Honech III/4922, 760 05, Zlín
Nationality: Czech
Affiliation: Department of physics and materials engineering,
Faculty of technology, Tomas Bata University in Zlín,
Náměstí T. G. Masaryka 5555, 760 01, Zlín, Czech
Republic
E-mail: matousek@ft.utb.cz



Current occupation:

2013-now

Continental Barum, s.r.o. Product Industrialization division – Technologist of hot & cold semi-products preparation, Commercial vehicle tyres
Otrokovice

Education:

2009-now

Doctoral studies

Tomas Bata University in Zlín, Faculty of technology,
Doctoral study programme P 2808 – Chemistry and
Materials Technology, Study course 2808V009 –
Chemistry and Materials Technology

2004-2009

Bachelor's and Master's
degree

Tomas Bata University in Zlín, Faculty of technology,
Study programme Chemistry and Materials
Technology, Study course Polymers Engineering
Master thesis: Foams pore size estimation and their
acoustic properties

2000-2004

High school education

Technical high school in Otrokovice, Study programme
Computer technology in chemistry.

Internships:

Date: 2010 (2 tweeks)
Place: Buenos Aires, Argentina
Organization: University of Buenos Aires, Faculty of Exact and Natural Sciences, Institute of Plasma Physics.

Occupation: Research team member.

Date: 2010 (4 months)
Place: Santa Fé, Argentina
Organization: Celint S.A., company organized by National University of Litoral, Faculty of Chemical Engineering.

Occupation: Research team member.

Projects participations:

2013 *Project "Centre of polymer systems"*
Reg. no: CZ.1.05/2.1.00/03.0111.
Occupation: Research team member.

2009-2012 *Doctoral grant project GAČR*
Reg. no: 104/09/H080.
Occupation: Research team member.

2012 *Grant IGA/FT/2012/037*
„Study of stereological characteristics of grainy and porous materials“
Occupation: Research team member.

2011 *Grant IGA/13/FT/11/D*
“Physical and physical-chemical modifications and characterizations of polymers”
Occupation: Research team member.

2010 *Grant IGA/26/FT/10/D*
“Study of physical properties of materials”
Occupation: Research team member.

APENDICES

A1: transcription of *.log file of the sample HR4250 showing the complete information about the CT data acquisition and following image reconstruction.

01 [System]
02 Scanner=SkyScan1174v2
03 Instrument S/N=11J03086
04 Software=Version 1. 1 (build 6)
05 Home Directory=C:\SkyScan1174ver2
06 Source Type=RTW 50/800
07 Camera=SHT MR285MC
08 Camera Pixel Size (um)= 17.14
09 CameraXYRatio=1.0000
10 [Acquisition]
11 Data Directory=C:\Users\SkyScan\Documents\matousek\01-2014-10-06-HR4250
12 Filename Prefix=HR4250_
13 Number Of Files= 925
14 Number Of Rows= 1024
15 Number Of Columns= 925
16 Partial Width= 71%
17 Image crop origin X= 189
18 Image crop origin Y=0
19 Camera binning=1x1
20 Image Rotation=359.8500
21 Gantry direction=CC
22 Optical Axis (line)= 512
23 Object to Source (mm)=226.60
24 Camera to Source (mm)=266.50
25 Source Voltage (kV)= 24
26 Source Current (uA)= 648
27 Image Pixel Size (um)=14.58
28 Scaled Image Pixel Size (um)=14.577000
29 Image Format=TIFF
30 Depth (bits)=16
31 Screen LUT=0
32 Exposure (ms)=9000
33 Rotation Step (deg)=0.200
34 Use 360 Rotation=NO
35 FlatField Update=YES
36 Scanning position=2.200 mm
37 Flat Field Correction=ON
37 Frame Averaging=ON (5)
38 Sharpening (%)=40
39 Random Movement=OFF
40 Geometrical Correction=ON
41 Filter=no filter
42 Rotation Direction=CC
43 Type of Detector Motion=STEP AND SHOOT
44 Scanning Trajectory=ROUND
45 Number of connected scans=1
46 Study Date and Time=Oct 07, 2014 02:44:17
47 Scan duration=11:49:26
48 [Reconstruction]
49 Reconstruction Program=NRecon
50 Program Version=Version: 1.6.4.6
51 Program Home Directory=C:\SkyScan1174ver2
52 Reconstruction engine=NReconServer
53 Engine version=Version: 1.6.4
54 Reconstruction from batch=Yes
55 Reconstruction servers= SCAN_1174_086
56 Option for additional F4F float format=OFF
57 Reconstruction mode=Standard
58 Dataset Origin=SkyScan1174v2
59 Dataset Prefix=HR4250_
60 Dataset Directory=C:\Users\SkyScan\Documents\matousek\01-2014-10-06-HR4250
61 Output Directory=C:\Users\SkyScan\Documents\matousek\01-2014-10-06-HR4250\
62 HR4250_Rec
62 Time and Date=Oct 30, 2014 17:39:10
63 First Section=15
64 Last Section=1007
65 Reconstruction duration per slice (seconds)=0.796576
66 Total reconstruction time (993 slices) in seconds=791.000000
67 Postalignment=-1.00
68 Section to Section Step=1
69 Sections Count=993

70 Result File Type=TIF
71 Result File Header Length (bytes)=12
72 Result Image Width (pixels)=924
73 Result Image Height (pixels)=924
74 Pixel Size (um)=14.57700
75 Reconstruction Angular Range (deg)=185.00
76 Use 180+=OFF
77 Angular Step (deg)=0.2000
78 Smoothing=5
79 Smoothing kernel=2 (Gaussian)
80 Ring Artifact Correction=4
81 Draw Scales=OFF
82 Object Bigger than FOV=OFF
83 Reconstruction from ROI=OFF
84 Filter cutoff relative to Nyquist frequency=100
85 Filter type=0
86 Filter type meaning(1)=0: Hamming (Ramp in case of optical scanner); 1: Hann; 2:
Ramp; 3: Almost Ramp;
87 Filter type meaning(2)=11: Cosine; 12: Shepp-Logan; [100,200]: Generalized Hamming,
alpha=(iFilter-100)/100
88 Undersampling factor=1
89 Threshold for defect pixel mask (%)=0
90 Beam Hardening Correction (%)=3
91 CS Static Rotation (deg)=0.0
92 Minimum for CS to Image Conversion=0.0000
93 Maximum for CS to Image Conversion=0.0579
94 HU Calibration=OFF
95 BMP LUT=1
96 Cone-beam Angle Horiz.(deg)=3.408352
97 Cone-beam Angle Vert.(deg)=3.772887

A2: transcription of *.csv protocol of 3D analysis of the sample HR4250

```

01 CT Analyser Version:      1.13.11.0
02 Date and time            1.2.2015 18:20
03 Operator identity        SkyScan
04 Computer name            SCAN_1174_086
05 Computation time        0:16:29
06 Dataset                  hr4250_voi_
07 Location                  C:\Users\SkyScan\Documents\matousek\structural      analysis\
                                OldistribucePORU\01-HR4250\VOI\

```

Description	Abbreviation	Value	Unit
-------------	--------------	-------	------

10			
11	Number of layers	993	
12	Lower vertical position	2.19E-01	mm
13	Upper vertical position	1.47E+01	mm
14	Pixel size	1.46E+01	um
15	Lower grey threshold	35	
16	Upper grey threshold	255	
17			
18	Total VOI volume	TV	2.83E+02 mm^3
19	Object volume	Obj.V	2.08E+01 mm^3
20	Percent object volume	Obj.V/TV	7.36E+00 %
21	Total VOI surface	TS	2.79E+02 mm^2
22	Object surface	Obj.S	8.20E+02 mm^2
23	Intersection surface	i.S	1.75E+01 mm^2
24	Object surface / volume ratio	Obj.S/Obj.V	3.94E+01 1/mm
25	Object surface density	Obj.S/TV	2.90E+00 1/mm
26	Surface convexity index	SCv.I	1.47E+01 1/mm
27	Centroid (x)	Crd.X	2.53E+00 mm
28	Centroid (y)	Crd.Y	2.48E+00 mm
29	Centroid (z)	Crd.Z	7.39E+00 mm
30	Structure thickness	St.Th	1.06E-01 mm
31	Structure linear density	St.Li.Dn	6.94E-01 1/mm
32	Structure separation	St.Sp	7.73E-01 mm
33	Degree of anisotropy	DA	1.0814E+000 (7.5251E-002)
34	Eigenvalue 1		5.34E-02
35	Eigenvalue 2		5.55E-02
36	Eigenvalue 3		5.78E-02
37	Number of objects	Obj.N	247
38	Number of closed pores	Po.N(cl)	9
39	Volume of closed pores	Po.V(cl)	6.22E-04 mm^3
40	Surface of closed pores	Po.S(cl)	7.33E-02 mm^2
41	Closed porosity (percent)	Po(cl)	2.99E-03 %
42	Volume of open pore space	Po.V(op)	2.62E+02 mm^3
43	Open porosity (percent)	Po(op)	9.26E+01 %
44	Total volume of pore space	Po.V(tot)	2.62E+02 mm^3
45	Total porosity (percent)	Po(tot)	9.26E+01 %
46	Euler number	Eu.N	-5004
47	Connectivity	Conn	5260
48	Connectivity density	Conn.Dn	1.86E+01 1/mm^3
49			

50 Structure thickness distribution		St.Th		
51 Range	Mid-range	Volume	Percent volume in range	
52	mm	mm	mm^3	%
53	1.4577E-002 - <4.3731E-002	2.92E-02	5.08E-01	2.414
54	4.3731E-002 - <7.2885E-002	5.83E-02	3.29E+00	15.6272
55	7.2885E-002 - <1.0204E-001	8.75E-02	5.06E+00	24.0604
56	1.0204E-001 - <1.3119E-001	1.17E-01	7.57E+00	35.9731
58	1.3119E-001 - <1.6035E-001	1.46E-01	3.81E+00	18.1023
59	1.6035E-001 - <1.8950E-001	1.75E-01	6.61E-01	3.1433
60	1.8950E-001 - <2.1866E-001	2.04E-01	1.38E-01	0.6558
61	2.1866E-001 - <2.4781E-001	2.33E-01	5.03E-03	0.0239
62	Standard deviation	SD	3.35E-02	mm

63 Structure separation distribution		St.Sp		
64 Range	Mid-range	Volume	Percent volume in range	
65	mm	mm	mm^3	%

66	1.4577E-002	- <4.3731E-002	2.92E-02	1.47E-01	0.056
67	4.3731E-002	- <7.2885E-002	5.83E-02	2.95E-01	0.1125
68	7.2885E-002	- <1.0204E-001	8.75E-02	4.48E-01	0.1709
69	1.0204E-001	- <1.3119E-001	1.17E-01	7.40E-01	0.2824
70	1.3119E-001	- <1.6035E-001	1.46E-01	1.05E+00	0.4009
71	1.6035E-001	- <1.8950E-001	1.75E-01	1.30E+00	0.496
72	1.8950E-001	- <2.1866E-001	2.04E-01	1.80E+00	0.6855
73	2.1866E-001	- <2.4781E-001	2.33E-01	2.06E+00	0.7882
74	2.4781E-001	- <2.7696E-001	2.62E-01	2.50E+00	0.9548
75	2.7696E-001	- <3.0612E-001	2.92E-01	3.02E+00	1.1514
76	3.0612E-001	- <3.3527E-001	3.21E-01	3.89E+00	1.4859
77	3.3527E-001	- <3.6443E-001	3.50E-01	3.91E+00	1.4925
78	3.6443E-001	- <3.9358E-001	3.79E-01	4.44E+00	1.6938
79	3.9358E-001	- <4.2273E-001	4.08E-01	5.27E+00	2.0132
80	4.2273E-001	- <4.5189E-001	4.37E-01	5.08E+00	1.9391
81	4.5189E-001	- <4.8104E-001	4.66E-01	5.55E+00	2.1197
82	4.8104E-001	- <5.1020E-001	4.96E-01	6.68E+00	2.5511
83	5.1020E-001	- <5.3935E-001	5.25E-01	6.32E+00	2.4132
84	5.3935E-001	- <5.6850E-001	5.54E-01	8.07E+00	3.0808
85	5.6850E-001	- <5.9766E-001	5.83E-01	8.36E+00	3.192
86	5.9766E-001	- <6.2681E-001	6.12E-01	7.82E+00	2.9835
87	6.2681E-001	- <6.5597E-001	6.41E-01	8.43E+00	3.2175
88	6.5597E-001	- <6.8512E-001	6.71E-01	1.01E+01	3.8476
89	6.8512E-001	- <7.1428E-001	7.00E-01	9.30E+00	3.5482
90	7.1428E-001	- <7.4343E-001	7.29E-01	8.85E+00	3.3793
91	7.4343E-001	- <7.7258E-001	7.58E-01	9.34E+00	3.5668
92	7.7258E-001	- <8.0174E-001	7.87E-01	1.01E+01	3.857
93	8.0174E-001	- <8.3089E-001	8.16E-01	1.21E+01	4.6008
94	8.3089E-001	- <8.6005E-001	8.45E-01	1.19E+01	4.54
95	8.6005E-001	- <8.8920E-001	8.75E-01	9.63E+00	3.6742
96	8.8920E-001	- <9.1835E-001	9.04E-01	9.40E+00	3.5883
97	9.1835E-001	- <9.4751E-001	9.33E-01	1.17E+01	4.4604
98	9.4751E-001	- <9.7666E-001	9.62E-01	8.55E+00	3.2634
99	9.7666E-001	- <1.0058E+000	9.91E-01	9.06E+00	3.4594
100	1.0058E+000	- <1.0350E+000	1.02E+00	1.08E+01	4.1232
101	1.0350E+000	- <1.0641E+000	1.05E+00	7.46E+00	2.8479
102	1.0641E+000	- <1.0933E+000	1.08E+00	9.34E+00	3.5655
103	1.0933E+000	- <1.1224E+000	1.11E+00	2.96E+00	1.1301
104	1.1224E+000	- <1.1516E+000	1.14E+00	3.94E+00	1.503
105	1.1516E+000	- <1.1807E+000	1.17E+00	7.14E+00	2.7264
106	1.1807E+000	- <1.2099E+000	1.20E+00	1.24E+00	0.4734
107	1.2099E+000	- <1.2390E+000	1.22E+00	3.14E-01	0.1198
108	1.2390E+000	- <1.2682E+000	1.25E+00	1.28E+00	0.4904
109	1.2682E+000	- <1.2974E+000	1.28E+00	1.39E+00	0.529
110	1.2974E+000	- <1.3265E+000	1.31E+00	1.61E+00	0.6156
111	1.3265E+000	- <1.3557E+000	1.34E+00	4.17E+00	1.5911
112	1.3557E+000	- <1.3848E+000	1.37E+00	1.24E-01	0.0474
113	1.3848E+000	- <1.4140E+000	1.40E+00	1.60E+00	0.6091
114	1.4140E+000	- <1.4431E+000	1.43E+00	1.47E+00	0.5621
115	Standard deviation		SD	2.75E-01	mm
116					
117	<u>ANALYSIS SPECIFICATIONS</u>				
118	Total grid size:		342 x 342 x 993		pixels
119	Sphere centered at:		[170,170,511]		pixels
120	Sphere radius:	967		pixels	
121	Pixel size:	1.4577E-002 x 1.4577E-002 x 1.4577E-002 mm ³ /voxel			
122					
123	<u>VOLUME FRACTION</u>				
124	BV/TV:	7.43E-02			
125	Sphere volume:	1.17E+04	mm ³		
126	Solid volume:	2.10E+01	mm ³		
127	VOI volume:	2.83E+02	mm ³		

ORIGINAL PUBLICATIONS

Pore Size Distribution in Foams

Tomáš Matoušek^a, Petr Ponížil and Marek Galetka

Department of Physics and Materials Engineering, Faculty of Technology, Tomas Bata University
in Zlín, Nad Stráněmi 4511, 760 05, Zlín, Czech Republic

^a matousekt@seznam.cz

Keywords: Macrostructure, polymer foam, open pores, image analysis and Voronoi tessellation.

Abstract. Physical properties of polymer foams depend on their macrostructure. In this paper, we study a range of polyurethane foams from the stereological point of view. Images of plane surfaces of studied samples were created by printing them on a sheet of paper and scanning these imprints. Consequent operations included reconstruction of pore section areas in the plane of printing and computation of pore volumes. The distribution of pore section was compared with data from computer tomography (CT) in order compare both methods.

Introduction

Many recent studies in materials science have focused on investigation of materials with a structure containing a large number of individual objects. A typical example of such a material is polymer foam; a system consisting of either discrete cells (closed-cell foams) or interconnected pores (open-cell foams). These systems are widely used in broad spectrum of applications, namely in civil engineering and the automotive technology [1].

Studying the dependence of physical properties on their structure and size of cells/pores in foams is the usual topic of researchers in this field nowadays [2-4]. For analyzing of the structure, various methods can be employed, such as CT [5] or Atomic force microscopy [6]. These methods provide very accurate and fast-obtained results; however, the equipment is quite expensive.

This paper presents a new, simple method, which provides comparable results with CT. The method is based on the principle of printing plane surfaces of various soft polyurethane foams with open pores on paper and consequent reconstruction of 2D (mean pore sections areas $\bar{E}a$) and 3D (mean pore volumes $\bar{E}V$).

Theory

Our method consists of several separate steps. For better understanding the theoretical background of them is given in this section.

Euclidean distance mapping (EDM) is a tool widely employed for image analysis [7]. A numerical value within the interval from 0 to 1 is assigned for each pixel of any black and white image. The zero values are considered as white vacancies between black objects. Therefore an equation describing the Euclidean distance d_{ij} , which is a distance from a nearest foreground pixel to each background pixel b_{ij} for any pixel in p^{th} row and q^{th} column can be written as following:

$$d_{ij} = \min_{1 \leq p, q \leq N} \left(\sqrt{(p-i)^2 + (q-j)^2} \mid b_{pq} = 1 \right) \quad (1)$$

Voronoi Tessellation is a way of decomposition of a d -dimensional space \mathbf{R}^d containing discrete points p_1-p_n to a system of closed cells generated from these points. In general, Voronoi tessellation can be described by equation:

$$V(p_i) = \left\{ x \in \mathbf{R}^d, \|x - p_i\| \leq \|x - p_j\| \right\}, \text{ for } i \neq j \quad (2)$$

Materials and methods

Specimens preparation. Five different samples of soft PUR foams (A-E) with open pores were provided by the company HG-style s.r.o. These samples were analyzed by the method of printing the surfaces and consequent scanning them in order to measure pore size distribution. In addition, sample A was examined by CT in order to determine the comparability of both methods.

A surface of a small piece of each sample with an area of the base of around 1 cm^2 was covered with stamp ink. Consequently, a special press consisting of two parallel triangular steel plates was employed for printing of these specimens. It was found that the deformation of 14 % is the optimal compromise between the appropriate downforce of the foams and relatively low deformation of pores due to the downforce. Therefore this deformation was used for printing. Comparable images were obtained by CT method, thus the same further processing could be employed.

In the next step, the prints were scanned to get digital black and white (binary) maps which were necessary for further image analysis. In such images there was a common problem of „noise“ – an occurrence of small black dots in the images caused mainly due to impurities of used paper and/or a dirty scanner. This undesirable phenomenon had to be removed to avoid possible negative affection of the result of the image analysis. This operation is illustrated in the Fig. 1. After this step the “clear” binary maps (Fig. 2) was used for further processing.



Fig. 1: An illustration of a noise removing from prints – the small dots and speckles in the left part are erased.

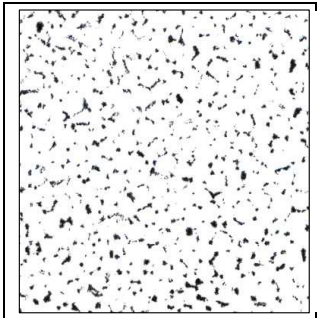


Fig. 2: A part of the binary map representing the printed image of the structure of PUR, Sample B

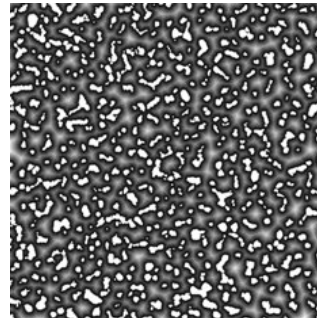


Fig. 3: The graphical result of the EDM – vacancies are represented by different tint of gray, Sample B.

Image analysis. This step was based on employing the tools of mathematical morphology [8, 9]. The EDM was applied on binary images of specimens (Fig. 3). As can be seen, the foreground boundary pixels are highlighted, while the centers of pore sections are located in areas with the lightest tint of gray (the lighter color, the bigger distance from the closest material pixel). These local maxima of EDM are centers of inscribed circles to these vacancies. On the basis of these centers the Voronoi tessellation – a final approximation of a real structure of foam can be computed.

Pore volumes. Three different methods for computation of pore volumes were used. The first method, used in the stereological standard ASTM E 112 [9] exploits a relation between Ea and Ev_1 :

$$Ev_1 = C.(Ea)^{3/2} \quad (3)$$

where the constant $C = 1.382$ [9]. The second method employs the classical formula for a computation of volume v of sphere with radius r (in our case $E_{V_2} = 4/3\pi(Er)^3$). E_{V_2} is a volume of a sphere with the mean radius Er . The computation of E_{V_3} is very similar to the E_{V_2} . From the known distribution of pore radii, the volume of each sphere was computed; then the mean value of volumes E_{V_3} was calculated.

Pore radii distribution. The pore radii distribution was estimated by the computer model. The principle of it was generating a large number of spheres with chosen diameter with Gaussian distribution. Each of these spheres was cut in random position and thus the model pore sections were obtained. Finally, the distribution of the model values was compared with experimental data.

Results

Pore size estimation. On the basis of the EDM calculation and Voronoi Tessellation Ea was measured for all materials. The values can be seen in Table 1. As can be seen there, the values Ea can be regarded as similar among the samples except sample B. The most important is the comparison between samples A and A(CT) which shows a good compliance of results obtained from both methods. While all remaining samples are comparable, sample B shows a different structure of pores. This material has distinctly larger cells, which is expressed by larger value of Ea . If one knows the areas of pore sections, a distribution curve for each sample can be simply drawn as shown in Fig. 4:

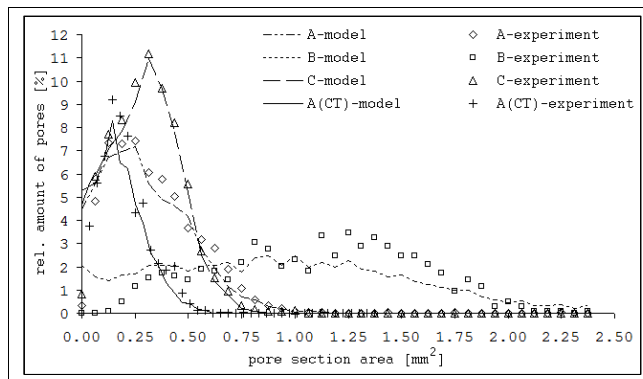


Fig. 4: Distribution curves of samples A-C compared with A(CT). Experimental data (points) fitted by model curves.

The graph confirms comparability between all samples except sample B (similar curves). In addition, it reveals that pores of area larger than 0.75 mm^2 are rare. In contrast with these samples, sample B shows a very wide distribution curve in the whole measured range.

Volumes of pores. While the distribution of pore section is very common characteristic of foams, the volume distribution or E_V describes the real 3D structure much better. There are several ways of computation of E_V . Table 1 shows 3 different E_V for each sample computed by employing different relations and Ea .

Table 1: A comparison of three different mean volumes E_V of pores and Ea for each sample.

Sample	A	A(CT)	B	C	D	E
Ea [mm^2]	0.36	0.37	1.11	0.34	0.46	0.37
E_{V_1} [mm^3]	0.30	0.31	1.63	0.27	0.43	0.31
E_{V_2} [mm^3]	0.16	0.17	0.89	0.15	0.24	0.17
E_{V_3} [mm^3]	0.21	0.22	1.15	0.23	0.21	0.13

As can be seen there, different ways of computation of this quantity provide different results. Due to this fact it is not easy to measure the distribution characteristic. In other words, E_V should be always accompanied by a description of measurement or computation of it. However, Table 1 again reveals the comparable values of E_V between samples A and A(CT).

Summary

Five soft PUR foams with open pores were examined from the stereological point of view. In order to characterize their structure, a new, simple method of printing the plane surfaces on a sheet of paper and consequent scanning of them was employed. A reconstruction of 2D net representing pore sections and following volume computation based on the standard [9] was carried out.

All of the methods used for E_V reconstruction assume the perfect isotropy. It would be also possible to assume the anisotropic cells; however it would become more complicated in such a case of the experiment. It would be necessary to make imprints of two or three perpendicular surfaces for each specimen and the model should be changed from the two-parametric into the three-parametric one (spheres should be replaced by ellipsoids). In the final, this change would bring unnecessary computational complexity of the method.

The results in the form of E_V and pore section areas distributions have been compared to data obtained by CT measurements. It has been shown that there is a good compliance between these two methods. Therefore, the new method has a big advantage. It provides results comparable with CT, employing a much cheaper device. The results show the opportunity for further experiments in this field and the potential of the technique to replace, in some cases, CT method.

Acknowledgment: This research was supported by the internal grant of TBU in Zlín No. IGA/26/FT/10/D funded from the resources of specific university research.

References

- [1] SARIER, N., ONDER, E.: Thermal characteristics of polyurethane foams incorporated with phase change materials. *Thermochim. Acta* 454. **2007**. 90-98.
- [2] LI, K., GAO, X.-L., SUBHASH, G.: Effects of cell shape and strut cross-sectional area variations on the elastic properties of three-dimensional open-cell foams. *J. Mech. Phys. Solids*, 54(4). **2006**. 783-806.
- [3] PISPOLA, G., HOROSHENKOV, K.V., KHAN, A.: Comparison of two modeling approaches for highly heterogeneous porous media. *J. Acoust. Soc. Am.* **2007**. 121(2). 961-966.
- [4] ZHANG, T.: A general constitutive relation for linear elastic foams. *Int. J. Mech. Sci.* 50(6). **2008**. 1123-1132.
- [5] SAADATFAR, M. et al.: Imaging of metallic foams using X-ray micro-CT. *Colloid Surface A: Physicochem. Eng. Aspects* 344. **2009**. 107-112.
- [6] OCHOA, N.A. et al.: Pore size distribution based on AFM imaging and retention of multidisperse polymer solutes Characterisation of polyethersulfone UF membranes with dopes containing different PVP. *J. Membrane Sci.* 187. **2001**. 227-237.
- [7] KOLOUNTZAKIS, M.N., KUTULAKOS K.N.: Fast Computation of the Euclidean Distance Maps For Binary Images. *Information Processing Letters*. 43(4). **1992**. 181-184.
- [8] SERRA, J.: *Image Analysis and Mathematical Morphology, vol. 11: Theoretical Advances*. Academic Press, London, **1988**.
- [9] ASTM E 112-96. **2004**. Standard Test Methods for Determining Average Grain Size.

Materials Structure & Micromechanics of Fracture VI

10.4028/www.scientific.net/KEM.465

Pore Size Distribution in Foams

10.4028/www.scientific.net/KEM.465.145

DOI References

[1] SARIER, N., ONDER, E.: Thermal characteristics of polyurethane foams incorporated with phase change materials. *Thermochim. Acta* 454. 2007. 90-98.

doi:10.1016/j.tca.2006.12.024

[2] LI, K., GAO, X.-L., SUBHASH, G.: Effects of cell shape and strut cross-sectional area variations on the elastic properties of three-dimensional open-cell foams. *J. Mech. Phys. Solids*, 54(4). 2006. 783- 806.

doi:10.1016/j.jmps.2005.10.007

[3] PISPOLA, G., HOROSHENKOV, K.V., KHAN, A.: Comparison of two modeling approaches for highly heterogeneous porous media. *J. Acoust. Soc. Am.* 2007. 121(2). 961-966.

doi:10.1121/1.2427114

[4] ZHANG, T.: A general constitutive relation for linear elastic foams. *Int. J. Mech. Sci.* 50(6). 2008. 1123-1132.

doi:10.1016/j.ijmecsci.2008.01.007

[5] SAADATFAR, M. et al.: Imaging of metallic foams using X-ray micro-CT. *Colloid Surface A: Physicochem. Eng. Aspects* 344. 2009. 107-112.

doi:10.1016/j.colsurfa.2009.01.008

[6] OCHOA, N.A. et al.: Pore size distribution based on AFM imaging and retention of multidisperse polymer solutes Characterisation of polyethersulfone UF membranes with dopes containing different PVP. *J. Membrane Sci.* 187. 2001. 227-237.

doi:10.1016/S0376-7388(01)00348-9

[7] KOLOUNTZAKIS, M.N., KUTULAKOS K.N.: Fast Computation of the Euclidean Distance Maps or Binary Images. *Information Processing Letters.* 43(4). 1992. 181-184.

doi:10.1016/0020-0190(92)90197-4

Submission Confirmation

stics.

t polyurethane foams from planar cross

 Print  Return to Dashboard

© Thomson Reuters | © ScholarOne, Inc., 2014. All Rights Reserved.

ScholarOne Manuscripts and ScholarOne are registered trademarks of ScholarOne, Inc.

ScholarOne Manuscripts Patents #7,257,767 and #7,263,655.

 @ScholarOneNews |  System Requirements |  Privacy Statement |  Terms of Use



Pore size distribution estimation of soft polyurethane foams from planar cross section images

Journal:	<i>Journal of Cellular Plastics</i>
Manuscript ID:	Draft
Manuscript Type:	Standard Article
Date Submitted by the Author:	n/a
Complete List of Authors:	Matousek, Tomas; Tomas Bata University in Zlin, Dpt. of Physics and Materials Engineering Fojtu, Dusan; Tomas Bata University in Zlin, Dpt. of Physics and Materials Engineering Ponizil, Petr; Tomas Bata University in Zlin, Dpt. of Physics and Materials Engineering; Tomas Bata University in Zlin, Centre of Polymer Systems
Keywords:	Pore size estimation, Pore size distribution, Stereology, Voronoi tessellation, Soft polyurethane foams, X-ray computed microtomography, Acoustic behaviour
Abstract:	A novel method of estimating the mean pore size and the size distribution of soft polyurethane foams is presented. The method is based on analyzing the binarized reconstructed X-ray computed microtomography images representing two-dimensional (2D) cuts through the three-dimensional (3D) bubble-network of 5 commercially available polyurethane foams. This technique employs standard tools of image analysis and mathematical morphology, giving the basis for Voronoi tessellation computations and the associated reconstruction of 2D network of pore cross sections. Finally, the 3D pore size distribution is found using the principles of the self-designed virtual structural model of spheres with normal distribution of their radii, fortuitously truncated by uniformly distributed cutting plane. The experimental data fitting is attained thank to Monte Carlo modelling, by searching the mean size value and the standard deviation, which determines the distribution width, at minimum possible least square. The acoustic behaviour dependence of the foams on the structural parameters is studied by means of acoustic absorption coefficient measurement.

1
2
3
4
5
6
7
8
9
10
11
12
13
14
15
16
17
18
19
20
21
22
23
24
25
26
27
28
29
30
31
32
33
34
35
36
37
38
39
40
41
42
43
44
45
46
47
48
49
50
51
52
53
54
55
56
57
58
59
60

SCHOLARONE™
Manuscripts

For Peer Review



Article

Pore size distribution estimation of soft polyurethane foams from planar cross section images

Journal of Information Science
1–11
© The Author(s) 2015
Reprints and permissions:
sagepub.co.uk/journalsPermissions.nav
DOI: 10.1177/0165551510000000
jis.sagepub.com

Tomas Matousek

Department of Physics and Materials Engineering, Faculty of Technology, Tomas Bata University in Zlin, Zlin, the Czech Republic
Centre of Polymer Systems, University Institute, Tomas Bata University in Zlin, Zlin, the Czech Republic

Dusan Fojtu

Department of Physics and Materials Engineering, Faculty of Technology, Tomas Bata University in Zlin, Zlin, the Czech Republic

Petr Ponizil

Department of Physics and Materials Engineering, Faculty of Technology, Tomas Bata University in Zlin, Zlin, the Czech Republic
Centre of Polymer Systems, University Institute, Tomas Bata University in Zlin, Zlin, the Czech Republic

Abstract

A novel method of estimating the mean pore size and the size distribution of soft polyurethane foams is presented. The method is based on analyzing the binarized reconstructed X-ray computed microtomography images representing two-dimensional (2D) cuts through the three-dimensional (3D) bubble-network of 5 commercially available polyurethane foams. This technique employs standard tools of image analysis and mathematical morphology, giving the basis for Voronoi tessellation computations and the associated reconstruction of 2D network of pore cross sections. Finally, the 3D pore size distribution is found using the principles of the self-designed virtual structural model of spheres with normal distribution of their radii, fortuitously truncated by uniformly distributed cutting plane. The experimental data fitting is attained thank to Monte Carlo modelling, by searching the mean size value and the standard deviation, which determines the distribution width, at minimum possible least square. The acoustic behaviour dependence of the foams on the structural parameters is studied by means of acoustic absorption coefficient measurement.

Keywords

Pore size estimation, pore size distribution, stereology, Voronoi tessellation, soft polyurethane foams, X-ray computed microtomography, acoustic behaviour.

1. Introduction

Polyurethane based (PU) foams belong to the family of polymeric porous materials with multiple applications possibilities in civil engineering [1], automotive industry [2], packaging [3], and other specific areas [4]. Thanks to their versatility, PU foams have attracted interest of numerous researches and studies. Extensive research has been done on formulating and proving structure-property relations [5]–[9].

The PU foams can be generally divided into rigid and flexible foams. This branching predetermines the main application areas of both types. As it has been confirmed by numerous studies, the microstructure of PU plays the crucial role regarding to the macroscopic properties. The rigid PU foams with closed-cell structure exhibit highly efficient thermo-insulating properties [10], while open-cell structure of flexible PU foams can offer excellent acoustic

Corresponding author:

Tomas Matousek, Department of Physics and Materials Engineering, Faculty of Technology, Tomas Bata University in Zlin, Zlin, the Czech Republic
Nam. T.G. Masaryka 555, 760 01, Zlin, the Czech Republic
matousek@ft.utb.cz

absorption abilities [11]. Moreover, the physical properties of PU can be either tailored chemically during the synthesis [12] or enhanced by blending with another compound afterwards [3], [7].

Generally, the most suitable and meaningful structural characteristic of a porous medium, is pore size distribution (PSD) outgoing from knowledge of pore sizes [11], [13]–[15]. The issue of investigating and characterizing the PSD in PU foams usually follows two basic approaches. The former one is direct observation and quantitative characterization of the structure. Some basic structural features, including window (face) dimensions and strut lengths and thicknesses, can be revealed by traditional techniques, namely photography or microscopic observations [11]. However, measuring all the 3D features especially the pore sizes by means of these techniques is extremely complicated due to spatial structures of pores in foams. These measurements also frequently require sample destruction. The complete determination of porous structure characteristics, without any special requirements of sample preparation offers a non-destructive technique X-ray computed microtomography (μ CT) [14], [16]. Although this technique has been originally developed as a medical imaging tool, nowadays it is being widely employed also in materials research [16]–[19].

The second group of methods is based on various modelling and simulation approaches, employing mathematical, statistical and stereological procedures. Some of the used models utilize the principle of random sphere packing in combination with spatial tessellations [16], [20], [21]; however; the other papers follow modelling based on generally polyhedral cell shapes and use self-developed algorithms for the cell sizes quantification [19], [22].

The purpose of this paper is to estimate the PSD from individual planar cross section images through the studied PU foams. It is important to remark that the proposed method have been designed with the intention to offer a comparable, cheap and simple alternative to μ CT.

2. Materials and methods

Five different types of soft polyurethane foams have been investigated in this paper. All the selected materials were provided by HG Style s.r.o, Kojetin Company, the Czech Republic. The foams were characterized from the supplier by their density (ρ) and compression resistance to 40 % deformation ($\Omega_{c(40\%)}$). The manufacturer declared that these foam parameters have been determined with compliance with Czech and German standard methods – density by ČSN EN ISO 845 (645411) and DIN 53420, respectively and compression resistance according ČSN EN ISO 845 (645411) and DIN 53577. The overview of the materials is shown in Table 1.

Table 1. Overview of the studied materials and their physical properties.

Material	ρ (kg/m ³)	$\Omega_{c(40\%)}$ (kPa)
2015	20	1.5
4070	40	2.0
HR 4250	42	5.0
HR 5050	50	5.0
CMHR 6052	60	5.2

2.1. Samples preparation

The cylindrical-shaped samples of the foams for the X-ray microtomography scanning, resembling the shape and size of a cigarette filter (ca. 30 mm in height and 8 mm in diameter) were knocked out from the slabs delivered from the manufacturer by using a leather punch. The sampling place was chosen at a random place, but far enough from the edge of the slab, so that the essential sampling conditions requiring both preserving representativeness of the structure and no mechanical distortion were fulfilled. Attachment of the samples to the rotational samples stage of the microtomograph was assured by a common double-sided tape.

2.2. X-ray computed microtomography

The images of planar cross sections for further image analysis were acquired by employing X-ray microtomograph SkyScan 1174 (Bruker) and further processing of the raw data. The individual scans were performed with the resolution 14.577 μ m/px which equals to conventionally expressed image resolution of 1742 dpi. This resolution also defined the

size of the volume element (voxel) as $14.577 \mu\text{m}^3$ and thus the thickness of the single virtual slice, represented by a single cross section image. The remaining scan parameters were preset individually for each sample (X-ray tube voltage was 24 kV, current 636–661 mA, exposure time 9000–11200 ms, rotational step 0.2° and averaging was of 5 images for each rotational step). The structural analysis procedure was carried out within a cylindrical region of interest (ROI) of diameter 4.999 mm (343 px in the image), manually defined along the vertical axis of symmetry of the sample roughly in the middle between the under most and the topmost slice.

2.3. Individual-images analysis

The key, self-designed method of this research was based on investigations and analyses done on the individual overlying cross section images through the studied foams from previous μCT scanning and reconstructions. These images were batch processed using open-source image-editing software ImageJ and the planar structural characteristics were extracted. The PSD, which is the desired spatial characteristic, was estimated with the help of Monte Carlo modelling, as it will be described further.

2.3.1. Image binarization

Binarization, the very first step of the image analysis, consisting of several steps, was executed to find and erase all unwanted image information and preserve only black strut cross sections and white pores cross sections. Similarly to the CTAn, the ROI had to be defined. The square with the side of 5.539 mm (380 px in the image) was placed randomly over the images and the images were cropped according to it. Further, the images were subjected to enhancing the contrast of very fine image details and revealing the pale contours. By means of a filter “Shadow” implemented in ImageJ a shadow effect, with light appearing to come from a certain direction the contrast was enhanced. On the other hand, this led to slight increase of image noise too. Thus, the “Despeckle” filter was used to erase these small noise speckles. Final step – the thresholding was carried out using default global thresholding adjustment of the software. The binarized images were subsequently batch-processed by means of image analysis, leading to the reconstruction of pore section boundaries based on Voronoi tessellation computations. The whole process of binarization is shown in Figure 1.



Figure 1. The scheme of binarization steps.

2.3.2. Voronoi tessellation computations

The binarized images served as the starting point for the planar Voronoi tessellation computations. The goal of this technique was to reconstruct the pore sections boundaries pursuant to the dislocation of the strut sections and therefore to reconstruct and quantify the individual pore cross sections and their areas.

Firstly, the Euclidean distance map (EDM) computations were performed on the binarized image. In principle, EDM computed the Euclidean distance (d_{ij}) from each white, background representing pixel with the pixel value (b_{pq}) = 1 in the i^{th} row and j^{th} column of the image consisting out of the N pixels in the pixel raster of p rows and q columns to the closest black foreground pixel with the value $b_{pq} = 0$. Consequently, the computational algorithm assigned the same shade of grey to the pixels with equalling white-to-closest-black distances in such a way, that with the increasing distance the brightness decreases. Thus, the white-black gradient was created, helping the observer to distinguish the same or similar distances easily. Mathematically, this can be written as distance calculation by means of equation (1):

$$d_{ij} = \min_{1 \leq p, q \leq N} (\sqrt{(p-i)^2 + (q-j)^2} \mid b_{pq} = 1) \quad (1)$$

The image analysis steps are illustrated in Figure 2. The initial binarized image (Figure 2a) was subjected to EDM computation. The mathematical result of this procedure, transferred into a graphical expression of EDM (Figure 2b) shows the colour gradient passing from the darkest tints of grey that surrounds the pore boundaries (struts) to almost white colour representing the areas around the pore section centres. In other words, the lighter colour marks the greater distance of a respective pixel to the closest pixel belonging to the pore boundary. The EDM maxima were in the next step considered as the centres of the circles inscribed within the pore cross sections (Figure 2c) and the centres of these circles were used as the generators of Voronoi tessellation cells (Figure 2d).

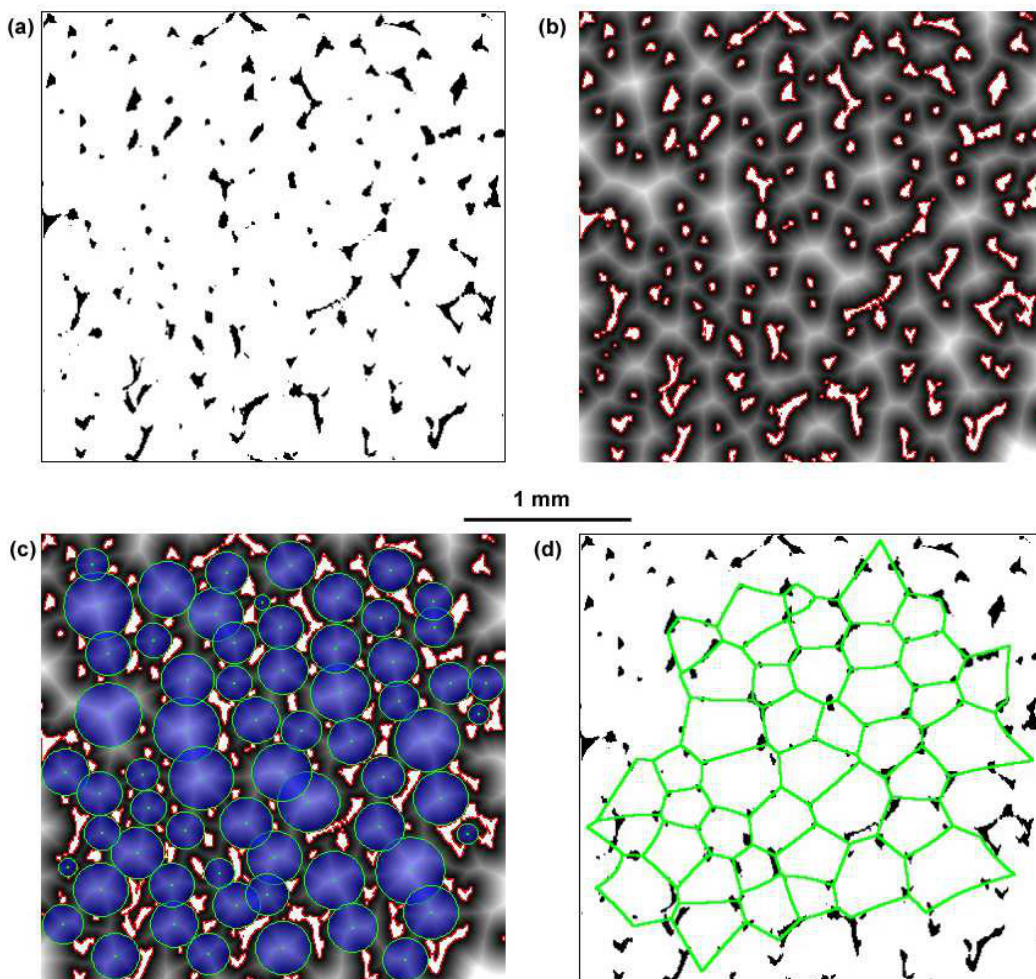


Figure 2. (a) binarized image of the transversal cross section through a polyurethane foam from μ CT scanning (sample 4070), (b) graphical expression of EDM computation, the lightest areas showing EDM maxima indicate the pore cross section centres, (c) approximation of the pore cross sections with inscribed circles, (d) resulting Voronoi tessellation approximation generated from the centres of the inscribed circles.

Construction of the cells is in principle very similar to the growth of pores in polymeric foams, therefore Voronoi tessellation can serve as a good model for pore cross section approximation. This was confirmed also in this particular case. As one can see in Figure 2d, the Voronoi tessellation network fits the cross sectional structure of the foam relatively precisely and thus it was considered as a meaningful 2D approximation of the real structure. Inasmuch as the size of each individual cell was known from the previous computations, the data could be interpreted as a representative, mathematically quantified planar pore cross section size distribution. Note that the outer cells were erased in order to prevent from possible results distortions caused by presence of edge phenomena (e.g. in cases when a pore cross section was intersected by the edge of the investigated area). As the final distribution it was considered the total 2D distribution, summing up the data from all cross section images for each sample.

A very important comment has to be mentioned regarding to 2D pore cross sections. The planar pore profiles must not be understood as the mean pore cross sections, as the random cutting plane, intersecting a system of spherically shaped pores rarely hits the equatorial line or the axis of symmetry. The bigger objects are truncated with higher probability than the smaller ones, thus the resulting distribution is size-weighted. Moreover, a cross section through a big sphere could have the same profile area as the near-equatorial cross section through a small sphere. These phenomena are well known among the stereologists as Wicksell corpuscle problem [23], [24]. Therefore, the pore cross section cannot be directly transferred to pore volumes, only estimated.

2.3.3. Modelling the 3D structure

Although the Voronoi tessellation-based approach offers the possibility to determine the pore cross section size distribution, this planar characteristic is insufficient for the desired structural description of the 3D foam structure. Therefore, the pores radii distribution was estimated by a computer simulation.

The model used for the structural description of the studied PU foams assumed a set of spheres with the normal distribution of their radii, characterized by the mean radius ($\bar{E}r$) and standard deviation (σ_r), representing a virtual pore size distribution. This set contained the same amount of spheres as the number of cross sectional profiles in the total 2D distribution (the total number of the virtual spheres was in the order of thousands). Provided that these spheres were placed in space in such a manner that their centres were aligned on a “zero” line, a virtual cutting plane (X) with the uniform probability to appear in any place within the interval $\langle 0; \bar{E}r + 3\sigma_r \rangle$ was generated. Despite the general theory of the normal distribution it was assumed that the value $\bar{E}r + 3\sigma_r$ was the maximal possible sphere radius. Always, when the sphere was intersected by the plane X, the related cross section area was computed. This led to obtaining the model distribution of pores cross section areas for the selected values of $\bar{E}r$ and σ_r . Finally, with the help of Monte Carlo modelling these parameters of the experimental total 2D distribution were found. The experimental distribution parameters were found at the lowest least squares, when comparing the experimental and model distributions. The simplified scheme of the model is sketched in Figure 3.

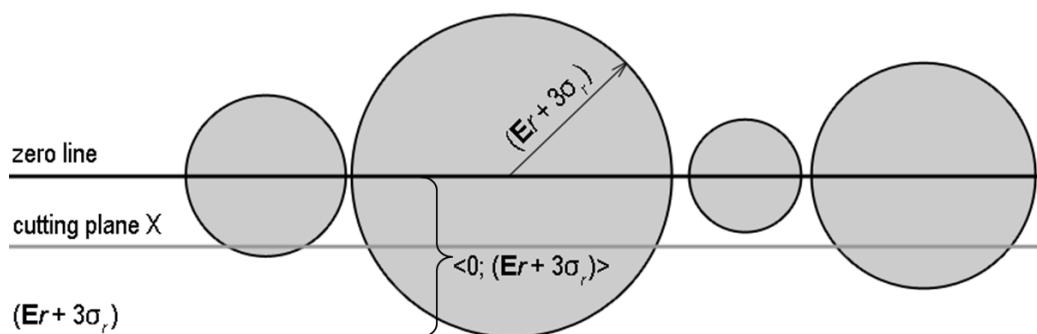


Figure 3. A simplified scheme of the structure-describing model: the virtual spheres have their centres aligned in the zero line, while a random cutting plane X is placed at any position within the interval $\langle 0; \bar{E}r + 3\sigma_r \rangle$. If the cutting plane misses a sphere, the situation is ignored, otherwise a corresponding cross section profile area is computed.

2.4. Acoustic properties of the foams

The acoustic behaviour of the foams in the form of acoustic absorption coefficient (α) measurement and the noise reduction coefficient (NRC) computation was studied. The acoustic absorption coefficient α is defined as the ratio incident-to-pass acoustic energy and is measured in a certain range of frequencies. Based on the results of α measurement; the NRC is counted as the arithmetical average of a values at 250, 500, 1000 and 2000 Hz, according to ASTM C423 specification [25].

The acoustic analysis was performed in two-microphone impedance tube (Brüel & Kjaer, type 4206). The acoustic absorption coefficient was measured through the frequency range 16–4000 Hz on two cylindrical samples for each material of the diameters 100 mm (for the band 16 Hz–1600 Hz) and 30 mm (for 50–4000 Hz); both samples were 40 mm thick.

3. Results and discussion

3.1. Estimation of mean pore sizes

Mean pore size (EV) is a single value, very roughly describing the internal structure of a porous material. Although this quantity does not help to reveal the complex character of the cellular structure, mainly pore size distribution, it is being used as the most basic quantifier of the internal porous structure in some cases. Thus, 4 mean pore size volumes were computed from the data obtained by the X-ray microtomographic analysis (μ CT) and the Voronoi tessellation-based approach. Note that all the computations presumed strictly spherical shape of the individual cells.

The μ CT scanning and further cross section image reconstruction evaluates the size of the pores by Structure separation ($St.Sp$) parameter. This value was defined as the mean of diameters of the largest spheres which fulfil two conditions: the spheres are entirely bounded within the solid surfaces, represented by the struts, and simultaneously the spheres enclose a point which is evaluated as the EDM local maximum for the respective pore cross section (but the point is not necessarily the centre of the sphere) [26]. Therefore, the value of $St.Sp$ can be easily transferred into the μ CT-determined mean pore volume (EV_{CT}). This value, computed from the μ CT scanning served as the comparative result for the remaining 3 estimated values. The mutual comparison of the mean volumes is shown in Figure 4.

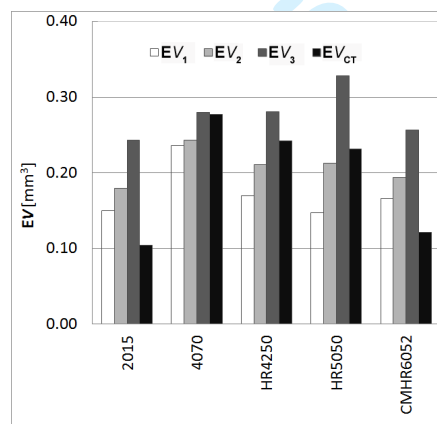


Figure 4. Comparison of mean pore volumes estimated by 3 methods with the values obtained by μ CT.

The model parameter-based mean pore volume (EV_1) was computed from the Er value, characterizing the mean cross section radius of the best experimental-data-fitting model distribution, while the third mean pore volume (EV_2) was found as the arithmetical average of generated “model” pore volumes belonging to this distribution. Finally, the ASTM E112-based mean pore volume [27] was computed by averaging the areas of the individual Voronoi tessellation cells

through the whole dataset (giving the mean cross section area (\mathbf{EA}) and consequent conversion to mean volume (\mathbf{EV}_3) according to the equation (2). The overview of the mean pore volumes values computed and estimated for the individual samples is given in Table 2

Table 2. Mean pore volumes.

Material	\mathbf{EV}_{CT} (mm ³)	\mathbf{EV}_1 (mm ³)	\mathbf{EV}_2 (mm ³)	\mathbf{EV}_3 (mm ³)
2015	0.104	0.150	0.180	0.243
4070	0.277	0.236	0.243	0.280
HR 4250	0.242	0.170	0.210	0.281
HR 5050	0.232	0.147	0.213	0.328
CMHR 6052	0.122	0.166	0.194	0.257

$$\mathbf{EV}_3 = \sqrt{\frac{6}{\pi}} (\mathbf{EA})^{3/2} \quad (2)$$

As one can see from the presented results (Table 2 and Figure 4), \mathbf{EV}_{CT} values have not exhibited any evident relationship neither between \mathbf{EV}_{CT} and ρ , nor any dependency of \mathbf{EV}_{CT} on $\Omega_{c(40\%)}$. The mutual comparison of the individual mean volumes, clearly seen in Figure 4, shows that the estimations – values \mathbf{EV}_1 , \mathbf{EV}_2 and \mathbf{EV}_3 have variable deviations from \mathbf{EV}_{CT} within the measured samples. Specifically, the comparison of the maximum value (ASTM-based \mathbf{EV}_3 , in all cases) with \mathbf{EV}_{CT} brings the scatter of their ratios ($\mathbf{EV}_{CT} / \mathbf{EV}_3$) range 0.43–0.99. On the other hand the estimations have not revealed any correlation among the \mathbf{EV}_1 , \mathbf{EV}_2 and \mathbf{EV}_3 . The reason of this fact is caused by very small differences of the values, because the deviation of the smallest estimated volume (\mathbf{EV}_1) from the greatest volume (\mathbf{EV}_3) for samples 2015, 4070, HR 4250, HR 5050 and CMHR 6052 were 0.093, 0.044, 0.111, 0.180 and 0.091 mm³, respectively.

3.2. Estimation of pore size distributions

Pore size distributions of all PU foams estimated from the individual cross section images, expressed in the terms of pore diameters, compared with μ CT distributions are shown in Figure 5. As it is evident from the results, employing Monte Carlo modelling has brought fairly satisfactory compliance of the model and experimental (μ CT), as the shape, and width of the respective distribution curves are similar to each other. That means that the model was capable to estimate and describe 2 basic distribution parameters – the mean value (note that the maxima of all model distributions are of the same order as the maximal values determined by μ CT) and the standard deviation of this value, defining the distribution width. This result confirms the expectations on comparability of results with μ CT data.

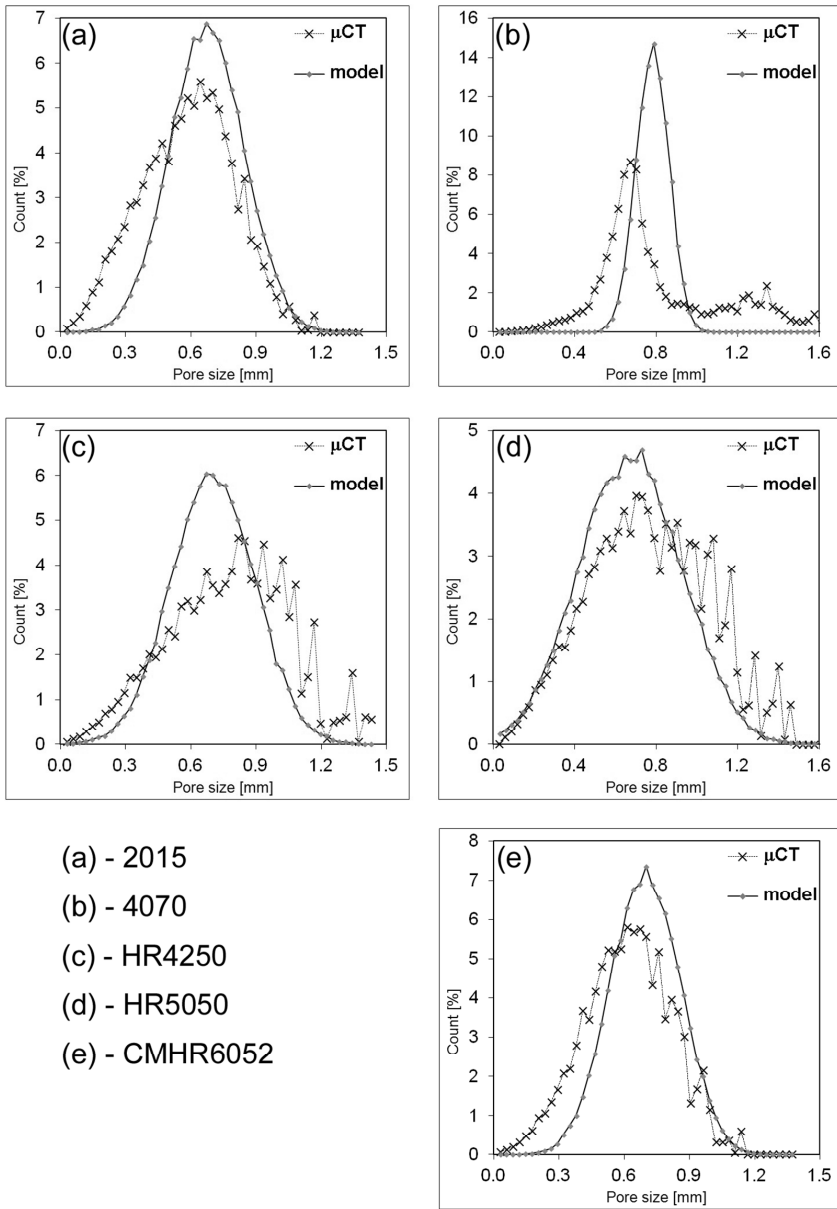


Figure 5. Pore size distributions of all studied PU foams obtained by the estimation of pore size from planar cross section images compared with the distribution curves computed on the basis of μ CT foam scans.

3.3. Acoustic properties

3.3.1. Acoustic absorption coefficient

The acoustic absorption coefficient dependence on frequency is shown in Figure 6. As it is evident from this plot, the curves are similar to each other with only small variance among them. This fact can be attributed to the previously mentioned narrow scatter of mean pore sizes.

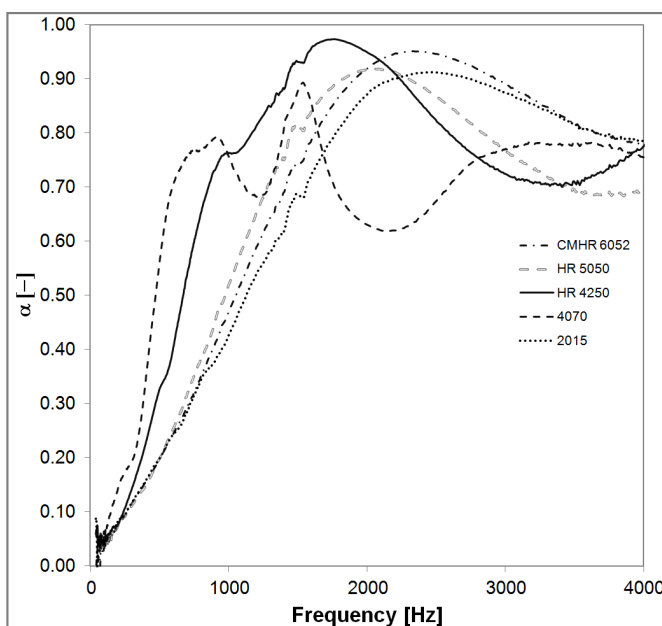


Figure 6. The acoustic absorption dependence on the measured frequency for all measured PU foams.

However, it can be stated, that the samples HR 4250 and 4070, exhibit the best acoustic absorption properties from the entire set of the samples at lower frequencies (band up to 1 kHz) as these 2 individual curves show considerable higher acoustic absorption at this range. Moreover, the acoustic absorption behaviour of the sample HR4250 differs also between the frequencies 1 kHz and 2 kHz when α reaches the maximum of 0.97 (at 1.76 kHz) which was the highest value measured in global. The acoustic response in the remaining part of the frequency band can be evaluated as similar to other materials, despite the decline of α to ca. 0.7 (slightly above 3 kHz).

It is also clear that the overall acoustic response of sample 4070 differs from the behaviour of the other samples, as α reaches two local maxima and two local minima along the measured frequency range. While the first minimum of α (approximately $\alpha = 0.72$ at 0.8 kHz) exceeds the α values of all remaining samples, the second minimum (ca. $\alpha = 0.62$ at around 2.1 kHz) lies considerably below the α of the other samples at this frequency.

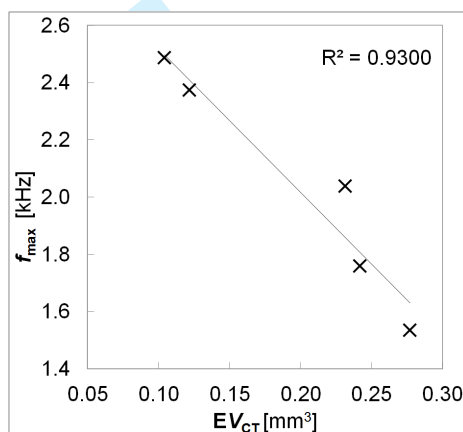
3.3.2. Maximum damping frequency, noise reduction coefficient

Maximum damping frequency (f_{\max}) is the frequency value that corresponds to the maximum α measured within the frequency interval. This characteristic predetermines the most suitable application area. Another expression of the overall acoustic properties can be characterized by means of the noise reduction coefficient (NRC), which is the arithmetical average of the α values measured at 250, 500, 1000 and 2000 Hz, according to standard ASTM C423 specification [25]. Both values are listed in Table 3.

Table 3. Noise reduction coefficient and maximum damping frequency of the foams.

Material	NRC (-)	Maximum acoustic damping	
		f_{\max} (Hz)	α (-)
2015	0.40	2488	0.91
4070	0.53	1536	0.89
HR 4250	0.54	1760	0.97
HR 5050	0.43	2040	0.92
CMHR 6052	0.42	2376	0.95

Due to the narrow scatter of mean pore sizes, which was mentioned above the only evident relationship between the structure and acoustic properties is the mutual dependence of maximum damping frequency and mean pore size EV_{CT} , as shown in Figure 7 that reveals a downward trend of the maximum damping frequency f_{\max} with increasing mean pore size EV . These results points out to the fact, that the materials with greater EV are more suitable for lower frequencies, when used as the acoustic dampers, while the foams with smaller EV value are more advisable for damping of higher frequencies.

**Figure 7.** The correlation between f_{\max} and EV_{CT} .

Conclusions

The proposed method of estimating the pore size distributions of polyurethane foams from single planar cross section images has been compared with the pore size distributions of the same materials determined by X-ray microtomographical analysis. Although a clear correlation between the mean volumes from the direct measurement and estimated values has not been revealed, the results of distribution comparisons have verified comparability of the data obtained by this novel approach with the microtomographical distributions. The further research should be focused mainly on the improving the currently presented method, namely to Voronoi tessellation computations in 3D which should overcome the intermediate step of this procedure – using Monte Carlo modelling for finding the distribution parameters and offer direct estimation of pore size distribution from the cross section images. The final remark should stress the fact that the method is applicable not only to the images obtained by μ CT scanning, but also to any image of the planar surface of the foam.

Acknowledgements

This article was written with support of Operational Program Research and Development Fund (ERDF) and national budget of Czech Republic, within the framework of project Centre of Polymer Systems (reg. number: CZ.1.05/2.1.00/03.0111).

Funding

This research received no specific grant from any funding agency in the public, commercial or not-for-profit sectors.

References

- [1] Kallaos J, Bohne RA and Hovde PJ. Long-Term Performance of Rigid Plastic Foam Building Insulation. *J Mater Civil Eng* 2014; 26: 347–378.
- [2] Gupta TK, Singh BP, Tripathi RK, et al. Superior nano-mechanical properties of reduced graphene oxide reinforced polyurethane composites. *R Soc Chem Adv* 2015; 5: 16921–16930.
- [3] Cinelli P, Anguillesi I and Lazzeri A. Green synthesis of flexible polyurethane foams from liquefied lignin. *Eur Polym J* 2013; 49: 1174–1184.
- [4] Lamba NMK, Woodhouse KA and Cooper SL. *Polyurethanes in Biomedical Applications*. Boca Raton: CRC Press, 1998, pp.150–155.
- [5] Javni I, Song K, Lin J and Petrovic ZS. Structure and properties of flexible polyurethane foams with nano- and micro-fillers. *J Cell Plast* 2011; 47: 357–372.
- [6] Vesenjak M, Borovinsek M, Fiedler T, et al. Structural characterisation of advanced pore morphology (APM) foam elements. *Mater Lett* 2013; 110: 201–203.
- [7] Zhang C, Hu Z, Gao G, et al. Damping behavior and acoustic performance of polyurethane/lead zirconate titanate ceramic composites. *Mater Design* 2013; 46: 503–510.
- [8] Yilgör I, Yilgör E and Wilkes GL: Critical parameters in designing segmented polyurethanes and their effect on morphology and properties: A comprehensive review. *Polymer* 2015; 58: A1–A36.
- [9] Sonnenschein M, Wendt BL, Schrock AK, et al. The relationship between polyurethane foam microstructure and foam aging. *Polymer* 2008; 49: 934–942.
- [10] Demharter, A. Polyurethane rigid foam, a proven thermal insulating material for applications between +130°C and –196°C. *Cryogenics* 1998; 38: 113–117.
- [11] Zhang C, Li J, Hu Z, et al.: Correlation between the acoustic and porous cell morphology of polyurethane foam: Effect of interconnected porosity. *Mater Design* 2012; 41:319–325.
- [12] Chollon G, Deletrez S and Langlais F. Chemical vapour infiltration and mechanical properties of carbon open-cell foams. *Carbon* 2014; 66: 18–30.
- [13] Matousek T., Ponizil P and Galetka M. Pore Size Distribution in Foams. *Key Eng Mat* 2011; 465: 145–148.
- [14] Pardo-Alonso S., Solórzano E, Brabant L, et al. 3D Analysis of the progressive modification of the cellular architecture in polyurethane nanocomposite foams via X-ray microtomography. *Eur Polym J* 2013; 49: 999–1006.
- [15] Lee ST and Ramesh NS. *Polymeric Foams: Mechanisms and Materials*. Boca Raton: CRC Press, 2004, pp.150–155.
- [16] BurtEAU A, N'Guyen F, Bartout JD, et al. Impact of material processing and deformation on cell morphology and mechanical behavior of polyurethane and nickel foams. *Int J Solid Struct* 2012; 49: 2714–2732.
- [17] Marie E, Buffiere JY, Salvo L, et al. On the Application of X-ray Microtomography in the Field of Materials Science. *Adv Eng Mater* 2001; 3: 539–546.
- [18] Mader K, Mokso R, Raufaste C, et al. Quantitative 3D characterization of cellular materials: Segmentation and morphology of foam. *Colloid Surface A* 2012; 415: 230–238.
- [19] Bock J and Jacobi AM. Geometric classification of open-cell metal foams using micro-computed tomography. *Mater Charact* 2013; 75: 35–43.
- [20] Redenbach C. Microstructure models for cellular materials. *Comp Mater Sci* 2009; 44: 1397–1407.
- [21] Lochman K, Oger L and Stoyan D. Statistical analysis of random sphere packing with variable radius distribution. *Solid State Sci* 2006; 8: 1397–1413.
- [22] Buffel B, Desplentere F, Bracke K, et al. Modelling open cell-foams based in the Weaire-Phelan unit cell with a minimal surface energy approach. *Int J Solids Struct* 2014; 51: 3461–3470.
- [23] Wicksell SD. The corpuscle problem I. *Biometrika* 1925; 17: 84–99.
- [24] Wicksell SD. The corpuscle problem II. *Biometrika* 1926; 18: 152–172.
- [25] ASTM C423-99a. Standard Test Methods for Sound Absorption and Sound Absorption Coefficients by the Reverberation Room Method, ASTM International: Applications note on sound absorber specimen, 2001.
- [26] Hildebrand T and Ruesegger P. A new method for the model-independent assessment of thickness in three-dimensional images. *J Microsc-Oxford* 1997; 185: 67-75.
- [27] ASTM E112. Standard Test Methods for Determining Average Grain Size, ASTM International: Analytical Chemistry for Metals, Ores, and Related Materials, 2004.